

Alma Mater Studiorum – Università di Bologna

DOTTORATO DI RICERCA IN

CHIMICA

Ciclo XXX

Settore Concorsuale di afferenza: **03/B1**

Settore Scientifico disciplinare: **CHIM/03**

**LUMINESCENT NANO-ARCHITECTURES FOR
THERANOSTIC APPLICATIONS**

Presentata da: **Francesco Palomba**

Coordinatore Dottorato

Prof. Aldo Roda

Supervisor

Prof. Luca Prodi

Co-Supervisor

Prof. Marco Montalti

Esame finale anno 2018

ABSTRACT

Theranostic is a new paradigm in nanomedicine, aiming to design unique nanostructures where diagnostic and therapeutic tools are combined. The development of new nanotechnologies has allowed fast and important step forwards in this direction, frequently focused on the optimization of materials for cancer treatment. The aim of my research work has been not only the design and preparation of nanomaterials for theranostic applications, focusing the investigation on dye doped Pluronic Silica nanoparticles (PluSNPs, a biocompatible silica core surrounded by a polymeric PEG shell), but also the development of methods or technical tools, both based on fluorescence, for an improved characterization of such materials. These complementary themes are presented in different chapters, each describing in detail the strategy, the experimental work and the conclusions yielded by the data treatment and interpretation.

A first significant part of my research has been devoted to the improvement of the principal synthetic strategies to obtain luminescent Pluronic/silica nanoparticles able to act as efficient luminescent biomarkers (chapter 2) or theranostic agents integrating drug loading and release in the same structure (chapter 4). The synthesis of PluSNPs for drug delivery purposes was carefully tuned to obtain a good entrapment and discharge of lipophilic chemotherapy drugs (Sorafenib) from the nanoparticles with a suitable kinetic for application. This drug delivery system showed very promising effects *in vitro* as tumor angiogenic controller.

A punctual characterization of such materials is not trivial due to their high complexity confined in a space in the nanometric range. To this goal I have investigated a new fluorescence based solvatochromic method, that we propose to map the polarity of neighboring nanoenvironments (Chapter 3). This method evidenced the complex architecture of the Pluronic shell of this nanoparticles which can promote both hydrophilic and hydrophobic interactions shining light on the host/guest abilities of these structures.

Aiming to *in vivo* applications the understanding of the possible nanoparticle interactions with the bioenvironment is of fundamental importance. To this goal I have both studied: i) the interaction between PluSNPs and a fluorescent labeled hyaluronic acid (one of

the chief hydrophilic components of the extracellular matrix) and ii) a novel fluorescence cross-correlation based imaging method (2D-pCF) to map dynamical processes in cellular environments. In the first case fluorescence-based investigation has been used to follow the formation of hyaluronic acid/PluSNPs interactions (chapter 5) to propose a model mechanism for the description of nanoparticle/biomolecular corona formation. It is important to underline that the nanoparticles interacting with the hyaluronic acid have proven to be internalized faster, a possible indication of their increased theranostic abilities.

As important as the formation of these complex aggregates is the study of their motion and localization in the cells. To this goal I have spent a period abroad at the Laboratory of Fluorescence Dynamics, University of California, Irvine, where the group of Professor Enrico Gratton has developed a novel fluorescence cross-correlation based imaging method (2D-pCF), 2D-pCF is useful to achieve the map of dynamical processes and the trajectories of fluorescent nanostructures in cellular environments. I applied this technique to the investigation of motion of a fluorescent protein involved on the repair mechanism upon a DNA damage (chapter 6) but, in principle, can be extended to the investigation of cellular internalization phenomena which involves fluorescent molecular and/or nanostructured materials.

To summarize, in this thesis I have presented new powerful fluorescence-based techniques for the design, synthesis and characterization – also in cellular environments – of nanostructures based on Pluronic Silica Nanoparticles. In this way, more efficient theranostic nanoparticles have been obtained, with the expectation that the techniques described here can be extended also to other materials, making a step forward in the field of nanomedicine.

List of Abbreviation

FRET	Forster Resonance Energy Transfer
2D-pCF	Two-Dimensional pair Correlation Function
Alt-EJ	Alternative End-Joining
APTES	Amino Propyl Triethoxy Silane
ATM	Ataxia–telangiectasia mutated
ATMi	Ataxia–telangiectasia mutated inhibitor
ATR	Ataxia–telangiectasia and Rad3 related
ATRi	Ataxia–telangiectasia and Rad3 related inhibitor
BSA	Bovine Serum Albumin
CA	Contrast Agent
CETS	Carboxyethylsilanetriol
CMC	Critical micellar Concentration
CT	Computed Tomography
Cy5	Cyanine 5
DDR	DNA Damage Response
DEAC	Diethylamino Coumarin
DLS	Dynamic Light Scattering
DMAP	4-Dimethylaminopyridine
DNA	Deoxyribonucleic Acid
DNA-PKA	DNA-dependent protein kinase
DNA-PKAi	DNA-dependent protein kinase inhibitor
DSB	Double Strands Breaks
EGFP	Enhanced Green Fluorescent Protein
EPR	Enhanced Permeability and Retention
ERK	extracellular signal–regulated kinases
Et2O	Diethyl Ether
F-127	Pluronic F-127
F-127 Amine	Pluronic F-127 Amine derivative
F-127 CARBO	Pluronic F-127 Carboxy derivative
FCS	Fluorescence Correlation Spectroscopy
FDA	Food and Drug Administration
H-bonds	Hydrogen Bond
HR	Homologous Recombination

Hya	Hyaluronic Acid
MRI	Magnetic Resonance Imaging
mRNA	messenger Ribonucleic Acid
NHEJ	Non-Homologous End-Joining
NIR	Near Infra-Red
NP	Nanoparticle
NR	Nile Red
OI	Optical Imaging
P	Prodan
PARP	Poly (ADP-ribose) polymerase
PARPi	Poly (ADP-ribose) polymerase inhibitor
PB	Phosphate Buffer
PBS	Phosphate Buffer Saline
PEG	Polyethylene Glycol
PET	Positron Emission Tomography
PluSNP	Pluronic F-127 Silica Nanoparticle
PPO	Polypropylene Oxide
QDs	Quantum Dots
QY	Quantum Yield
RALN	Right Axillary Lymph Node
RB	Rhodamine B
SLN	Sentinel lymph Node
SPECT	Single-photon emission computed tomography
SRF	Sorafenib Tosylate
SSA	Single Strand Annealing
TEM	Transmission Electron Microscope
TEOS	Tetra Ethyl Orthosilicate
TMOS	Tetra Methyl Ortho Silicate
VEGF	Vascular endothelial growth factor

CONTENTS

CHAPTER 1 - INTRODUCTION	1
1.1 Diagnosis, Therapy, Theranostic	1
1.2 Theranostic Nanoparticles	3
1.3 Nanomaterials for Cancer Treatment	6
1.4 AIM OF THE WORK	9
CHAPTER 2 - LUMINESCENT SILICA NANOPARTICLES	14
2.1 Introduction	14
2.2 Silica Nanoparticles in Nanomedicine	14
2.3 Synthesis of Dye Doped Silica Nanoparticles	15
2.3.1 Stöber Van Blaaderen synthesis	16
2.3.2 Reverse Microemulsion	17
2.3.4 Direct Micelle Assisted Method	18
2.4 Dye Doped PluSNPs	19
2.4.1 PluSNPs – Biological Application -	21
CHAPTER 3 – SHELL NANOPOLARITIES OF PLUSNPS	29
3.1 Spectral Fitting	33
3.2 Solvatochromic Energy Transfer	35
3.3 Conclusion	41
3.4 Experimental Methods	42
3.5 Technical Notes	43
CHAPTER 4 - DRUG DELIVERY OF PluSNP	58
4.1 Drug Delivery Nanoparticles	58
4.2 Synthesis Design of dye doped PluSNPs	61
4.3 Synthesis of SRF drug and RB dyes PluSNPs	62
4.4 SRF release and PluSNPs stability	63
4.6 Preliminary <i>in vitro</i> test	66
4.6.1 Proliferation of endothelial HUVEC cells	67
4.6.2 Morphology of HUVEC after 24h	67
4.6.3 Migration by scratch assay	68

4.6.4 Improvement for the <i>In vivo</i> Test	69
4.7 Conclusion	72

CHAPTER 5 - HYALURONIC ACID INTERACTION WITH PluSNPs -	76
5.1 Introduction	76
5.2 Probing conformational changes of Hya	78
5.3 Model of Interaction – Hya 200 KDa (SHya) and PluSNPs	83
5.4 Hya 200 KDA (SHya) media effect	87
5.5 Hyaluronic acid 1200 KDa (LHya)	89
5.6 Interaction Mechanism comparison of LHya and SHya	91
5.7 Hydrodynamic Size Distribution	95
5.8 Fluorescence Correlation Spectroscopy on Hya/PluSNPs ensemble	96
5.9 Prelaminar <i>in vitro</i> test	98
5.10 Conclusion	99
5.11 Technical Notes	100

CHAPTER 6 - APPLICATION OF A NOVEL FLUORESCENCE CROSSCORRELATION IMAGING TECHNIQUE -	109
6.1 Overview	109
6.2 pCF(δr)	110
6.3 DSB – a DNA Dangerous Damage	113
6.4 DSB Repair Mechanisms	115
6.5 HeLa – Laser Damage induce DSB	116
6.6 Ku-EGFP Motion Anisotropy Damage effect	119
6.7 Inhibition of DNA Damage Response	125
6.7.1 PARP	125
6.7.2 DNA-PK	126
6.7.3 ATM and ATR	126
6.8 Inhibition effect on the KU-EGFP motion	126
6.9 Conclusion	129
6. 10 Technical Notes	130

CONCLUSION	136
------------	-----

APPENDIX - PRYNCIPLES OF PHOTOPHYSICS -	139
A1 Electronic Excited State	139
A2 Solvatochromism	141
A3 Electronic Excitation Energy Transfer	143
A4 Electronic absorption spectra	147
A5 Emission and excitation spectra	147
A6 Excited state lifetime measurements	148
A7 Dynamic Light Scattering	148
A8 Fluorescence Correlation Spectroscopy	149

CHAPTER 1

INTRODUCTION

1.1 Diagnosis, Therapy, Theranostic

Nanotechnology is an emerging and fast-growing discipline that has extraordinary applications in health and environmental fields. In medicine, nanotechnology is expected to improve life expectancy, as well as in the last century the improvement of diagnostic and therapeutic procedures has promoted better condition and increased life quality. Nanomaterials are considered one of the most important and promising frontiers of research due to the possibility to design nanoplatforms combining more features in a single object yielding materials with extraordinarily versatile and customized properties. For example, the combination of therapeutic and diagnostic tools in a single object - referred as theranostic - is a very intriguing multimodal strategy in nanomedicine which could overcome unsolved problems. Theranostic nanomedicine is emerging as a promising therapeutic paradigm. It takes advantage of the high capacity of nanoplatforms to ferry cargos and loads together with imaging functions. The resulting nano-systems, capable of diagnosis, drug delivery and monitoring the therapeutic response, are expected to play a significant role in the dawning era of personalized medicine in particular in cancer treatment.¹⁻⁴ In the last decades, numerous drugs for cancer treatment have been discovered⁵, nevertheless, they generally present severe limitations compromising the therapy efficiency. Chemotherapy drugs, commonly, provoke hazardous side effects due to their intrinsic cytotoxicity. moreover, tumor cells can develop drug resistance. The main limit of the traditional medicine toward cancer treatment is a not satisfactory selectivity of the drug for these tissues, in fact, traditional drugs are spread out in the whole body with no specific distribution, showing a systemic toxicity. Side effects as hair loss, diarrhea, anemia and muscular pain can frequently appear during

chemotherapy becoming additional very relevant issues for the patients in the fight against cancer⁶. Moreover, tumor cells can develop drug resistance, eliminating any beneficial effect the therapy

A possible solution to increase the therapy efficacy and to limit side effects can be found thanks to nanotechnology, since nanosystems can be designed to be accumulated selectively inside the tumor tissue. Solid tumors, in fact, have different characteristics with respect to healthy tissue. An important difference is angiogenesis which consists of an increase of the vascularization level and the extensive production of muscular mediators, both yielding an abnormal vascular architecture and the alteration of lymphatics system. All this can be conveniently exploited in nanomaterials presenting intrinsic features enabling them to work as nanocarriers to selectively deliver tailored quantity of drugs in specific tissues. On the other hand, the same goal can be also reached by designing customized objects with *ad hoc* functions to target only the desired tissues. The spontaneous entrapment and accumulation of nano-sized species in the tumor is due to a phenomenon called Enhanced Permeability and Retention (EPR)⁷ caused by its abnormal vascular architecture (see *infra*). In particular, the EPR effect permits the accumulation of macromolecules, and in general of nanoscaled objects, in the interstitial of tumor tissues with concentration higher than the blood plasma^{8,9}.

As mentioned above, the versatility of nanostructured carriers can allow to integrate in the same nanoparticle also diagnostic features. These materials, in fact, have also been widely studied in the last decades as diagnostic agents for *in vitro* and *in vivo* applications. Indeed, biocompatible nanomaterials are considered as great candidates for the preparation of a new generation of contrast agents (CAs) since they allow to increase the signal output in many diagnostic techniques. Nanoparticle-based contrast agents present all the characteristics to become efficient tools for medical diagnostics and imaging in many modalities with possible valuable

repercussions on many medical areas including surgery. Nanostructures can be designed to allow also multimodal imaging, which could result much more efficient than the single analysis possible with conventional molecular-scale CAs. Moreover, they provide new abilities for *in vivo* detection and enhanced targeting efficiencies through longer circulation times, designed clearance pathways, and multiple binding capacities. Properly protected, they can be safely used for the fabrication of various functional systems with targeting properties, reduced toxicity, and proper excretion from the body. Nanosized CAs are expected to become standard practice in the field of imaging in a close future, for both bioimaging and medical imaging. In this context, one of the techniques which today can offer the widest plethora of applications ranging from the study of biological processes at molecular level to the surgery practice is optical imaging (OI)¹⁰. Luminescent nanomaterials for optical techniques are, as a matter of fact, the frontier for the development of emerging technologies with great potential for the improvement of disease prevention, diagnosis, and treatment. For all these reasons, fluorescence, nanomaterials, drug delivery, theranostic are focus topics with a key role within this thesis.

1.2 Theranostic Nanoparticles

The term “theranostic” has been coined to define ongoing efforts to combine diagnostic and therapeutic capabilities into a single agent for clinical applications, to develop more specific and even personalized therapies for various diseases. The rationale arises from the fact that diseases, such as cancer, are immensely heterogeneous, and all existing treatments are effective for limited patient subpopulations and only at precise stages of the disease development. The hope is that a close marriage of diagnosis, including genome interpretation, and therapy could provide more specific therapeutic protocols for each individual and, therefore, more likely to offer improved prognoses. The emergence of nanotechnology offers an opportunity to draw diagnosis and therapy

closer. Imaging nanoparticles and, parallel, nanomaterials for therapeutic application have been lively investigated in the last years, and the know-how in the field is now exploited in many laboratories worldwide to design theranostic nanoparticles, that is to say nanoplatforms which can allow a close monitoring of the region of interest not only before or after, but also during treatment¹¹.

Liposomes, gold, silver, iron (magnetic) and silica nanoparticles are only few examples of the many substrates investigated nowadays for theranostic purposes. Nanomaterials as diagnostic tools are, instead, already in clinical trials in many modern imaging techniques such as: magnetic resonance imaging (MRI), computed X-ray tomography (CT), positron emission tomography (PET), single-photon emission computed tomography (SPECT), ultrasound imaging (US) and optical imaging (OI)^{12–15}.

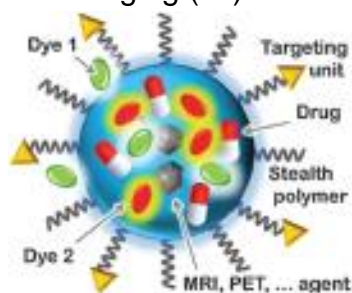


Figure 1. Schematic representation of a multifunctional system for nanomedicine¹⁶.

OI techniques can find applications in many fields from the surgical practice to the molecular investigation of different phenomena. Scientists take advantage of OI as tools for *in vitro* and *in vivo* investigations, in particular for soft tissue, for biological or hard technological materials, and they mainly exploit fluorescence-based techniques since the input energies, used to gain a highly resolved signal in space and time (from the nanoscale up to an entire organ, from femtoseconds up to hours), in most cases are not destructive and safe.

However, *in vivo* fluorescence optical imaging shows some limitations for deep tissues investigation since the penetration depth of light is quite low (only around two centimeters) and suitable only for soft tissues. This can be, therefore, an election technique for superficial skin diseases; in fact, it is already in the clinical trial stage for melanoma diagnosis. CAs for fluorescence imaging can be very useful tools also in surgery practice where they can guide the surgeon in the selective removal of the diseased tissue. Moreover, depth limitation can be partially overcome, and imaging extended to harder tissues as articulations, with photoacoustic imaging, again based on light excitation. In this case, a pulsed near infrared laser is used to irradiate a contrast agent which is able to produce ultrasound waves that are then detected by a medical ultrasound scanner¹⁷. We can say therefore that *in vivo* applications of optical imaging are still in their infancy, while they provide the best spatiotemporal resolution (nanoscale and femtoseconds) for *in vitro* applications due to the present technological level of microscopes, lasers, optical fibers and detectors. For these reasons in this field nano-sized objects can allow to increase the signal and to obtain functional information which can be hardly provided by other techniques¹⁰.

Besides the diagnostic features, theranostic nanomaterials have to be able to promote also efficiently targeted therapies.

In the framework of medicine, nanomaterials are extensively studied for cancer treatment applications thanks to the possibility given by EPR of their spontaneous accumulation in damaged tissues. Indeed, different therapies are presently in study such as photodynamic and photothermal therapies or local chemotherapy by drug delivery.^{11,18,19} Photodynamic and photothermal therapies exploit the nanomaterials to convert, respectively, the light stimuli into the production of reactive species (singlet oxygen, nitrogen oxide...) or into an increase of local temperature, both able to kill the surrounding cells. For the limitations described above, these therapies are proposed for the treatment of quite 'superficial' illness

(for example dermal diseases) or localized ones. Drug delivery of chemotherapeutic is, on the contrary, a method able to reach and treat diseased tissue simultaneously in the whole body. As already mentioned, in this case if targeting is not efficient healthy cells can also be damaged, with serious collateral effects.²⁰ Drug delivery consists into ferry a pharmaceutical cargo selectively to targeted sites drastically reducing critical side effects and tuning retention times. This difficult task can be fulfilled by a properly designed nanocarrier able to accumulate in the tumor, to locally release the drug in a controlled way that therefore can be lethal for the diseased tissues but not hazardous for the patient life quality. This main point is related to the drug volume to target ratio: in traditional administration the drug dose efficacy has to be computed taking into account its distribution in the entire body, while for a drug delivery system the dose has to be calculated for the volume of the diseased tissues. Nanoparticles suitable for drug delivery must be able to²¹:

- 1) hit selectively diseased sites: which can be obtained by passive (EPR) or active targeting (peptide, antibody...).
- 2) carry on and control the release of a discrete number of pharmaceutical agents: this can be achieved by designing *ad hoc* the nanomaterial yielding a structure able to establish controlled labile physical or chemical interactions with the drugs molecules.

1.3 Nanomaterials for Cancer treatment

Theranostic nanomaterials can be used *in vitro* for the diagnosis and the optimization of the treatment and *in vivo* for cure/monitor protocols. To develop more efficient theranostic agents it is necessary to induce selective targeting ability toward the desired cells or tissues. In the field of cancer treatment the EPR effect, studied and proposed by Maeda as an efficient way to hit solid angiogenic tissues (that is to say not only tumors but also inflammatory tissues²²) is principally associated with fenestrations in vasculature. This effect offers one of the most attractive way to

gain a selective accumulation of a nanostructure in a tumor tissue. This is an intrinsic property and it is made possible by the abnormal vasculature of the angiogenic tissues together with the longer circulation time of nanoparticles in comparison with single molecules. The selective accumulation of nanostructures is usually localized in the interstitial space²³.

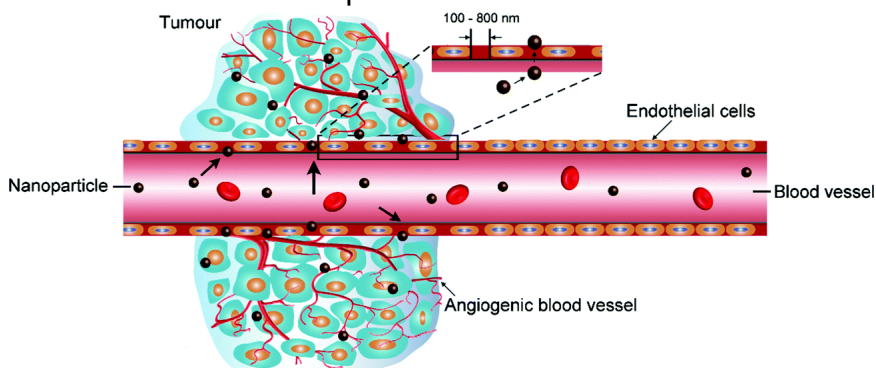


Figure 2. Schematic representation of the entrapment of nanoparticles inside a tumor tissue by Enhanced and Permeability Retention (EPR)²³.

The size of nanoparticles is a key factor for their efficient entrapment by EPR effect. This is due to the fact that objects of different sizes present very different circulating times, and this means that with a proper design of the size and shape of the nanoobject one can tune the amount of entrapped material. Objects smaller than 6 nm are excreted too rapidly via urine to accumulate in tumor tissues since they can pass the nephron membranes in the kidneys (this excretion pathway is the best one for optimum body clearance but too fast for an efficient delivery). Objects bigger than 100-150 nm circulate for a much longer time inside the body, this is constructive for tissue accumulation, but it can result in undesired high toxicity by bioaccumulation. Therefore, the nanostructure size is a very important parameter in the design of targeting materials, but it is not the only one since the nanostructure toxicity depends prevalently upon the composition, functionalization and properties of its surface.

After the localization in the tumor tissue, a theranostic nanoparticle must be internalized by cancer cells to carry out its therapeutic action. The parameters which affect cellular uptake depend upon the uptake mechanism and must be taken into account in the design of efficient theranostic nanomaterials^{24,25}. Several different cellular uptake mechanisms are possible, but in general the internalization is influenced by:

- size and shape
- surface charge
- surface hydrophilicity (hydrophobicity)

In general, these three parameters influence the nanoparticles/cell interaction and, consequently, the cytotoxicity, biocompatibility and bio-distribution of the material.

As already mentioned, the size of nanoparticles rules their uptake but also their shape can influence not only the membrane trafficking but also their intracellular localization²⁵. The other two parameters can be discussed together since they can prevent nanoparticle aggregation and influence the interaction with the cellular membrane. One of the most established way to prevent nanoparticle aggregation is by protecting the nanoparticle surface with polyethylene glycol (PEG). This polymer allows to increase the water solubility, the biocompatibility, it can work as anti-fouling agent and, therefore, protects the nanoparticle by undesired interactions with the species present in the biological media including proteins and other bio-macromolecules. In these media, in fact, nanoparticles are generally surrounded by a biomolecular corona which is a complex self-organized architecture of protein and biological molecules that interact with the surface of the nanoparticle. This corona can greatly interfere with the nanoparticles/cell interaction and their localization inside a cell, and it can be considered as the surface which mediates nano-objects trafficking. For these reasons, when designing a nanoparticle for an efficient internalization its interaction with the surrounding biological components must be carefully considered. Moreover, one could also take advantage by the formation of the biomolecular corona and, controlling its composition, it could be possible to target nanoparticles to specific

cells. According to this strategy, NPs are thought to be surface-designed to interact with biopolymers, influencing the corona and initiating targeted receptor-mediated cellular binding and internalization²⁶⁻²⁸.

1.4 AIM OF THE WORK

The aim of this work is the development of fluorescent tools for the improvement of nanomaterials designed for theranostic applications, focusing on platforms based on dye doped Pluronic Silica nanoparticles (PluSNPs). For this goal, it is necessary to:

- to investigate the host/guest abilities of these core/shell nanoparticles mapping the polarity of their different nanocompartments; this knowhow is crucial for increasing the drug loading ability and to suitably tune its release;
- to synthesize PluSNPs specifically designed for drug delivery purposes, taking Sorafenib – a lipophilic chemotherapeutic drug – as model;
- to check the effects of the drug-nanoparticle system *in vitro* as tumour angiogenic controller;
- to study and optimize the interaction of PluSNPs with macro/bio-molecules, taking hyaluronic acid (Hya) – one of the chief hydrophilic components of the matrix – as model compound;
- to study and control the effects of their interaction with HyA on the cell internalization of PluSNPs;
- to study a novel fluorescence cross-correlation based imaging method (2D-pCF), developed at the Laboratory of Fluorescence Dynamics, University of California, Irvine, to map the dynamical processes and the trajectories of fluorescent nanostructures in cellular environments;
- to apply this technique, that, in principle, can be very interesting for the investigation of cellular internalization phenomena which involves fluorescent molecular and/or nanostructured materials,

to the investigation of the motion of a fluorescent protein involved in the repair mechanism of a DNA damage.

To summarize, the fundamental theme of my research work is the development of luminescent core/shell silica nanoparticles as theranostic nanomaterials. For a proper design it is fundamental a precise characterization and a deep understanding of their performance in a biological environment. To these goals I have tested and optimized fluorescence-based techniques as powerful and, in some cases, new tools suitable for this investigation.

REFERENCES

- 1 P. N. Prasad, *Introduction to Nanomedicine and Nanobioengineering*, 2012.
- 2 J. Kim, Y. Piao and T. Hyeon, *Chem. Soc. Rev.*, 2009, **38**, 372–390.
- 3 A. Baeza, E. Guisasola, E. Ruiz-Hernández and M. Vallet-Regí, *Chem. Mater.*, 2012, **24**, 517–524.
- 4 Z. Chen, Z. Li, Y. Lin, M. Yin, J. Ren and X. Qu, *Chem. - A Eur. J.*, 2013, **19**, 1778–1783.
- 5 A. Luetke, P. A. Meyers, I. Lewis and H. Juergens, *Cancer Treat. Rev.*, 2014, **40**, 523–532.
- 6 A. M. Griffin, P. N. Butow, A. S. Coates, A. M. Childs, P. M. Ellis, S. M. Dunn and M. H. Tattersall, *Ann. Oncol.*, 1996, **7**, 189–95.
- 7 H. Maeda, J. Wu, T. Sawa, Y. Matsumura and K. Hori, *J. Control. Release*, 2000, **65**, 271–284.
- 8 Y. Matsumura and H. Maeda, *Cancer Res.*, 1986, **46**, 6387–6392.
- 9 H. Maeda, *Adv. Enzyme Regul.*, 2001, **41**, 189–207.
- 10 N. Institutes and H. U. October, 2010, 1–2.
- 11 J. Xie, S. Lee and X. Chen, *Adv. Drug Deliv. Rev.*, 2010, **62**, 1064–1079.

- 12 J. Gallo, N. J. Long and E. O. Aboagye, *Chem. Soc. Rev.*, 2013, **42**, 7816.
- 13 N. Lee, S. H. Choi and T. Hyeon, *Adv. Mater.*, 2013, **25**, 2641–2660.
- 14 N. Mitchell, T. L. Kalber, M. S. Cooper, K. Sunassee, S. L. Chalker, K. P. Shaw, K. L. Ordidge, A. Badar, S. M. Janes, P. J. Blower, M. F. Lythgoe, H. C. Hailes and A. B. Tabor, *Biomaterials*, 2013, **34**, 1179–1192.
- 15 F. Kiessling, S. Fokong, J. Bzyl, W. Lederle, M. Palmowski and T. Lammers, *Adv. Drug Deliv. Rev.*, 2014, **72**, 15–27.
- 16 M. Montalti, L. Prodi, E. Rampazzo and N. Zaccheroni, *Chem. Soc. Rev.*, 2014, **43**, 4243–4268.
- 17 S. Biffi, L. Petrizza, C. Garrovo, E. Rampazzo, L. Andolfi, P. Giustetto, I. Nikolov, G. Kurdi, M. B. Danailov, G. Zauli, P. Secchiero and L. Prodi, *Int. J. Nanomedicine*, 2016, **11**, 4865–4874.
- 18 D. W. Felsher, *Nat. Rev. Cancer*, 2003, **3**, 375–380.
- 19 Q. Chen, L. Xu, C. Liang, C. Wang, R. Peng and Z. Liu, *Nat. Commun.*, 2016, **7**, 1–13.
- 20 E. Piktel, K. Niemirowicz, M. Wątek, T. Wollny, P. Deptuła and R. Bucki, *J. Nanobiotechnology*, 2016, **14**, 39.
- 21 A. C. Anselmo and S. Mitragotri, *Bioeng. Transl. Med.*, 2016, **1**, 10–29.
- 22 H. Maeda, *Enhanced Permeability and Retention (EPR) Effect: Basis for Drug Targeting to Tumor*, Springer, Boston, MA.
- 23 Y. Dai, C. Xu, X. Sun and X. Chen, *Chem. Soc. Rev.*, 2017, **46**, 3830–3852.
- 24 M. Ferrari, *Nat. Rev. Cancer*, 2005, **5**, 161–171.
- 25 M. Ferrari, *Nat. Nanotechnol.*, 2008, **3**, 131–132.
- 26 M. Hadjidemetriou, Z. Al-Ahmady, M. Mazza, R. F. Collins, K. Dawson and K. Kostarelos, *ACS Nano*, 2015, **9**, 8142–8156.
- 27 M. Hadjidemetriou, Z. Al-Ahmady and K. Kostarelos,

- Nanoscale*, 2016, **8**, 6948–6957.
- 28 M. Hadjide metriou and K. Kostarelos, *Nat. Nanotechnol.*, 2017, **12**, 288–290.

CHAPTER 2

LUMINESCENT SILICA NANOPARTICLES

2.1 Introduction

Luminescence is a very sensitive technique that allows a detection down to the single molecule and offers submicron visualization and sub millisecond temporal resolution. The development of new systems that use luminescence-related techniques^{1,2} to collect molecular level information about biologically relevant processes needs to overcome many of the typical limitations of conventional luminophores - mainly organic dyes - such as poor photo-stability and water solubility, low quantum yield and aggregation under physiological conditions³. In this context, nanotechnology led to the design of platforms taking advantage of many classes of nanoparticles - organic, inorganic and metallic - which are currently used as fluorescent emitters, each presenting its own pros and cons. Probably the main distinction within luminescent nano-system is between dye doped nanomaterials and intrinsically luminescent ones: according to this broad classification luminescent dye-doped latex nanoparticles and quantum dots (QDs) are the most studied examples in the literature^{4,5,6}. Another very promising and versatile example of dye-doped luminescent systems are, however, silica nanoparticles, and in the next paragraph we will describe their principal features and bioanalytical applications.

2.2 Silica Nanoparticles in Nanomedicine

One of the most interesting and promising chemical matrix useful to develop theranostic nanostructures is silica, because its synthetic methods allow the fabrication of complex nanoarchitectures where size and the surface properties can be modulated to control possible interactions with biomolecules, a promising efficient cell internalization and specific tissues accumulation^{7,8}. Silica nanoparticles are composed by an amorphous lattice of silicon oxide, usually synthesized by sol gel processes that involve a silica

precursor (tetra-alkoxysilane derivatives). Their synthesis can be manipulated to obtain structures with different sizes (5 nm – 1 µm), porosity and shapes (disk, rod, spherical particles, hollow spheres...). Several different morphologies of silica nanoparticles are under investigation in clinical and preclinical tests, aimed for the evaluation of the cytotoxicity and the biocompatibility by oral or subcutaneous administration. For example, a special kind of silica nanoparticles developed by the group of Professor U. Wiesner, called Cornell Dots, are today used in first stage clinical trials for lymph node mapping in cancer patients. These particles comprise a targeting moiety, an antifouling polymer layer (PEG, polyethylene glycol), and an internal silica core labelled with a near-infrared (NIR) fluorescent dye. The diagnostic feature of Cornell Dots is provided by a fluorescent label - frequently an alkoxysilane Cy5 derivative - which is chemically entrapped inside the silica core.^{9,10}

2.3 Synthesis of Dye Doped Silica Nanoparticles

The synthesis of silica nanoparticles in solution can be obtained using sol-gel processes¹¹ under various conditions that lead to different materials by tuning parameters such as the catalytic conditions and nanoparticle nucleation and growth confinement. All these synthetic strategies, however, usually share tetraethoxysilane (TEOS) as their silica precursor and characteristics such as simplicity, low cost, versatility and control over nanoparticle dimensions. The reaction kinetics of silica precursor depends on the lengths of the alkoxy moieties of the silica precursor (smaller means faster) and the acid or alkaline catalysis which can influence the hydrolysis and condensation processes that lead the formation of the silicon oxide matrix. The main synthetic approaches are the Stöber-Van Blaaderen method and those involving hydrolysis and condensation confinement, known as reverse microemulsion (water-in-oil)¹² and direct micelle assisted methods (Fig. X)^{13,14}. Each synthetic approach has advantages and limitations that are transferred to the resulting nanostructures, designed to suit

particular applications. As a general indication, the use of trialkoxysilane derivatized dyes¹⁵ ensures condensation of the fluorophores within the silica matrix, preventing the leaching of dye from the particles. The number of molecular dyes that can be used for NPs doping is quite high but can be limited by the synthetic strategy. Limitations are mainly related to solubility in the reaction milieu and to the synthetic accessibility of the trialkoxysilane derivatives. Another important point is the electrostatic interaction between the dye and the silica matrix which generally favors the inclusion of positively charged dye and hampers negatively charged species. In the case of diagnostic applications, the combination of several factors such as the brightness of the system, spatial control over nanoparticle functionalization and the colloidal stability of the nanoparticle suspension determines the suitability of the synthetic method.

Table 1. Main fluorescent Silica nanoparticles synthetic methods: versatility (★ = poor; ★ ★ ★ = very good).

SNPs synthetic method	Dimensional range	Colloidal stability	Dyes Incorporation	Surface modification	Accessibility to hybrid systems	Overall efficiency
Stöber	★★★	★★★	★★	★	★★	★
Reverse microemulsion	★★	★★	★	★★★	★★★	★★
Direct micelles	★	★★★	★★★	★★★	★★	★★★

2.3.1 Stöber Van Blaaderen synthesis



Figure 3. Schematic representation of the Stöber-Van Blaaderen method

This method is far from dated, thanks to an accessible dimensional range spanning from 10 to several hundreds of nanometers (with one-pot procedures), very simple synthetic mixtures (TEOS, water and ammonia), mild conditions and the possibility to obtain very monodisperse NPs. In this strategy, TEOS hydrolysis and NP formation are promoted by ammonia and water using ethanol as the TEOS co-solvent. The dimension of NPs can be controlled by varying the concentrations and ratios of the components. Covalent doping of the NPs is achieved by using alkoxy-silane derivatized dyes, with some limitations due to their solubility in ethanol–water mixtures. The luminescence properties of these systems depend on the mutual position of the condensed fluorophores within the nanoparticle. The Cornell Dots synthesis is an evolution of the Stöber methods where a dye rich core works as seed for the heterogeneous nucleation of the silica.

2.3.2 REVERSE MICROEMULSION

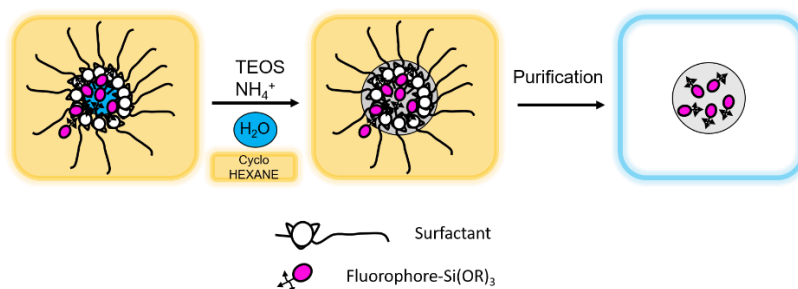


Figure 4. Schematic representation of the reverse microemulsion method

An appropriate mixture of a surfactant and a hydrocarbon induces the formation of a dispersion of reverse micelles, capable of housing a finite amount of water forming a macroscopically isotropic reverse microemulsion (water-in-oil). The water cores of a reverse microemulsion can be exploited as nano-containers to confine a Stöber synthetic process. Several protocols of this kind have been

proposed to give quite simple access to nanoparticle preparation and surface modification in the dimensional range of circa 15–200 nm¹⁴, where the dimension depends largely upon the surfactant type and the surfactant-to-water molar ratio¹⁶. This synthetic approach is usually appropriate for positively charged water soluble dyes^{15,17,18}, since they can be easily incorporated into the reverse microemulsion water cores and retained within the nanoparticle silica matrix by electrostatic interactions. This prerequisite constitutes a very strong limitation to the synthesis of fluorescent nanoparticles doped with water insoluble fluorophores or negatively charged ones.

2.3.4 DIRECT MICELLE ASSISTED METHOD

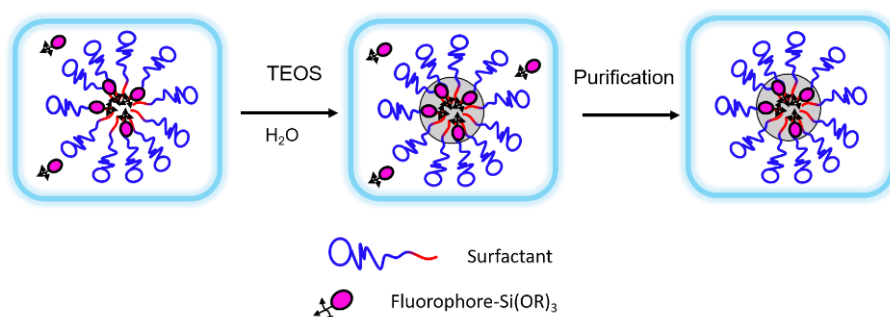


Figure 5. Schematic representation of micellar assisted method

In this synthetic approach, surfactant aggregates or co-aggregates in water are used as self-organized templates to confine the growth of the silica nanoparticles¹⁹. This is possible because of the lipophilic nature of silica precursors such as TEOS or other organo-alkoxysilane; a large range of organic dyes can be used as doping molecules using this approach. The general strategy involves a water solution of a low molecular weight surfactant (sometimes together with a co-surfactant) and a condensation process driven by ammonia that leads to monodisperse nanoparticles with a diameter from 5 to about 90 nm^{20,21}, a range that is particularly suitable for *in vivo* and *in vitro* applications. After the formation of the

nanoparticles, the colloidal suspension usually undergoes purification, usually performed by dialysis, ultrafiltration or centrifugation to remove surfactants, silica oligomers and non-trapped dyes. The nanoparticles investigated in this work are made by this synthetic approach, using a high molecular weight surfactant, conferring to the nanoparticles peculiar structure and characteristics that are reported in the next paragraph.

2.4 DYE DOPED PLURONIC SILICA NANOPARTICLES

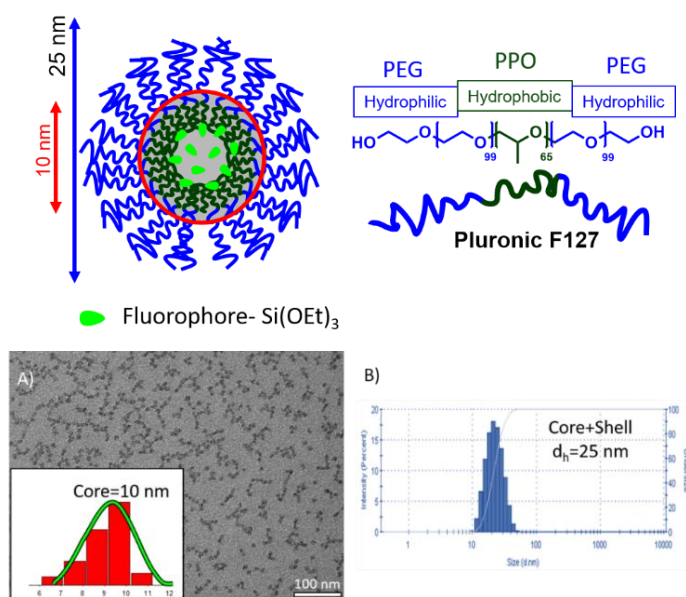


Figure 6. Dye doped Pluronic Silica Nanoparticles (PluSNPs), a schematic overview. A) TEM image and core size distribution. B) DLS Hydrodynamic size distribution

Prodi et al. in the last decade propose a very interesting dye doped silica core - PEGylated shell nanostructure (PluSNP) matching most of the requirements useful for theranostic applications: as biocompatibility, good body-clearance and size suitable for an EPR based drug delivery system. PluSNPs with remarkable

luminescence properties can be synthesized by chemical functionalization of their silica core with alkoxy silane derivatized fluorescent molecules. In the final material the silica core protects the embedded dyes from quenching and photobleaching agent extending their photo-stability and emission efficiency, gaining super bright nanoparticles. For these reasons, PluSNPs are already investigated as promising fluorescent probe *in vivo* as well as *in vitro* because they can be administrated safely by subcutaneous or intravenous injection or they can be incubated in a cell culture showing any side effects and negligible cytotoxicity. Moreover, the biocompatibility is due to the core/shell structure of the nanoparticle, because PluSNP is composed by a Pluronic F-127 shell, a PEG-PPO-PEG (hydrophilic PEG=polyethylene glycol, hydrophobic PPO= polypropylene oxide) biocompatible block co-polymer. The shell is partially entrapped in the porous silica core of 10 nm (measured by TEM, Transmission Electron Microscopy). PluSNPs show a monodisperse hydrodynamic size of 25 nm which increase slightly in protein containing media, showing that the Pluronic shell is effective in preventing protein adhesion and nanoparticles aggregation in demanding environment like blood plasma or serum or in any cellular culture media. These interesting nanostructures are synthesized via a micellar assisted route where Pluronic F-127 works as a surfactant and the Pluronic aggregate become a special kind of template where the hydrolysis and condensation of a silica precursor (TEOS or TMOS) can occur. This complex nanoarchitecture is originated by the entrapment of the Pluronic F127 filaments, providing the nanoparticle with a complex shell where hydrophilic and hydrophobic moieties co-habit. The shell compartment can be efficiently used to host many lipophilic molecules, such as fluorescent dyes or metal ion fluorescent biosensor, showing that this nanostructure is interesting and promising as intracellular carrier for drug delivery purposes²²⁻²⁴.

2.4.1 DYE DOPED PluSNPs - BIOLOGICAL APPLICATIONS -

The colloidal behavior in biological environment and the cell interactions of PluSNPs can be controlled by managing some nanoparticles charge properties (affecting their Z-Potential). Two main strategies are possible, acting on:

- the core charge, using the silica precursor combined with charged silane derivatives bearing ammonium or carboxylate moieties;
- the shell, upon transformation of the Pluronic F-127 hydroxyl groups into carboxylic acid or amine moieties.

In this paragraph are briefly described some example of biological application of PluSNPs as fluorescence label where the surface properties influence their biological activity.²⁰

In 2013 Prodi et al. showed a very interesting application of dye doped PluSNPs for the NIR imaging of sentinel lymph nodes. This investigation was carried out tuning the surface charge of the PluSNPs by two different strategy: i) the modification of the negative charge within the core by using CETS (Carboxy Ethyl Trihydroxy Silanol) or ii) by the insertion of carboxylate groups on the nanoparticle shell using carboxy derivatized Pluronic F-127. Different amounts of negative charge groups were tested, evaluating the trends of hydrodynamic size and the ζ -potential of different nanoparticles samples. The nanoparticles were doped with a Cyanine 7 NIR emitting dye, modified with a triethoxy silane group to have covalent link of the dye within the silica core. Fluorescence *in vivo* imaging investigation on mouse showed how different surface charge modification strategy influenced deeply the kinetics of accumulation and visualization of right axillary lymph node (RALN). The cause of such differences was attributed to a synergy between ζ -potential and size in physiological conditions. This hypothesis, was verified toward aggregation experiments between the NPs and bovine serum albumin, (BSA) in physiological conditions.

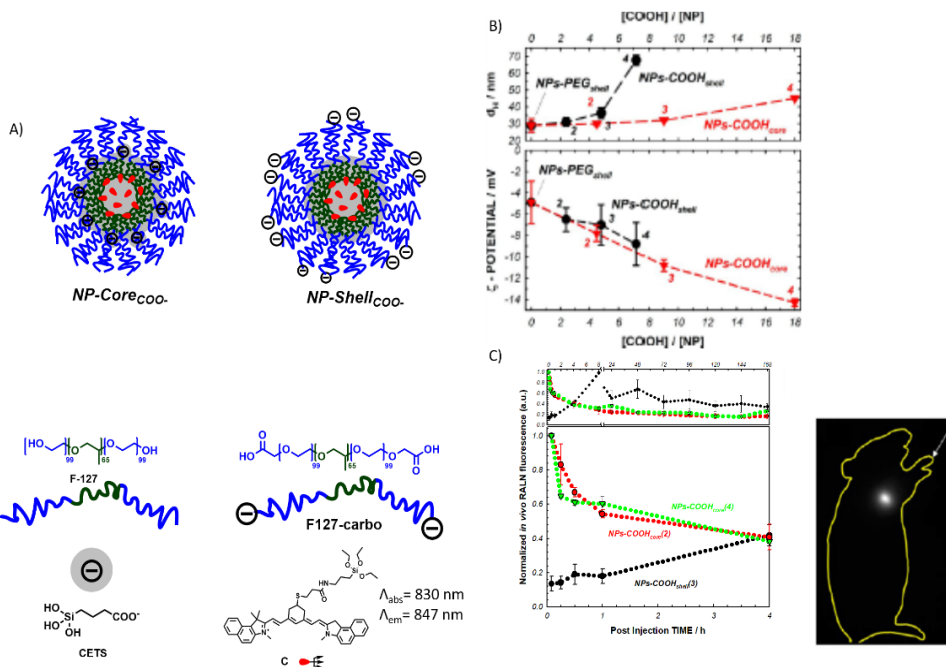


Figure 7. A) Schematic Representation of Cyanine 7 doped PluSNPs presenting negative charges within the core (introduced by CETS) and on the shell (using dicarboxylic modified Pluronic F-127 CARBO surfactant). B) Hydrodynamic size and ζ -potential of different samples containing increasing amount of CETS or F-127 CARBO. C) In vivo fluorescence intensity of RALN at different post-injection time. Mice were subcutaneously injected in the right anterior paw. Fluorescence imaging of RALN was performed at different times after injection with a 739 nm excitation light.

PluSNPs with negative charges on the shell showed a more pronounced aggregation behavior in the presence of BSA, with strong effects on their hydrodynamic diameter. On the other side, nanoparticles presenting a modified silica core were less prone to aggregation in the presence of BSA, with a hydrodynamic size always less than 60 nm, also in rich protein environments. PluSNPs with negatively charged core were then considered as the sample with the best overall performance in RALN mapping, probably

because of the more negative ζ -potential and less steep aggregation profile in the presence of BSA. These results clearly indicated that for SLN mapping the NP architecture in which the COOH groups (necessary to confer a negative ζ -potential) are buried in the PEG shell was more efficient than the one in which the same groups were outstretched from the surface of the NP.

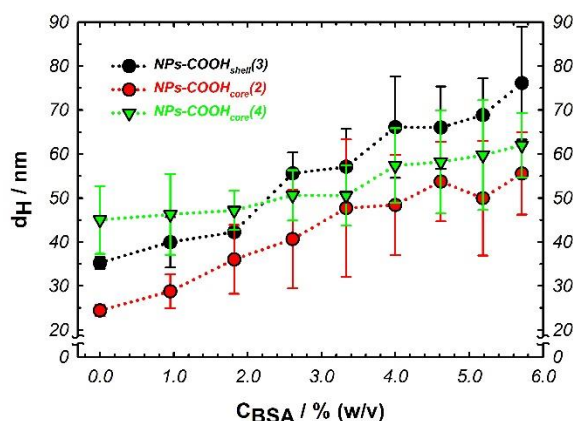


Figure 8. Hydrodynamic diameters (DLS) of NPs-COOH shell, NPs-COOH (2) and (4) core, and NPs-COOH core in the presence of increasing amounts of BSA. (NPs-COOH core (2) and (4) have two different amounts of COOH per nanoparticles respectively 4.5 and 18.)

The evolution of the effect of the rich protein environments on migration of a nanoparticle to a target tissue is a clear example on how the biomolecular corona can influence the colloidal behavior of this kind of nanoparticles in different tissues or via different systems (lymphatic, vascular...)

In another example, the influence of the PluSNPs surface chemistry was studied to evaluate effects on the endocytosis and to evaluate the interaction with lipid bilayer.

Surface charge of a nanostructures is responsible, in general, of nanoparticle/cells interaction. For PluSNPs positive surface charge can enhance the uptake by endocytosis due to the anionic charge

of cellular membranes. Moreover, the internalization of PluSNPs by JVM-2 B leukemic line in suspension, and of Hu7 cells in adhesion was promoted preferentially by caveolae-mediated pathway. Endocytosis mainly proceeded firstly by the interaction of nanoparticle with the cell membrane which can stimulate the formation and internalization of a vesicle²⁴.

The development of tools or techniques giving access to information at nanoscale level regarding interactions between nanoparticles and complex interfaces as the cellular membrane are highly desirable, since they can help to rationalize the design of fluorescent nanoparticles for imaging and theragnostic applications. A practical example was provided using an energy transfer approach (which occur between a donor and an acceptor only when they are very close, range about 10 nm, see Appendix) between PluSNPs with different charge and a dye labeled lipid bilayer. This tool permitted to describe the interaction *in vitro*, looking the energy transfer in cellular environment.

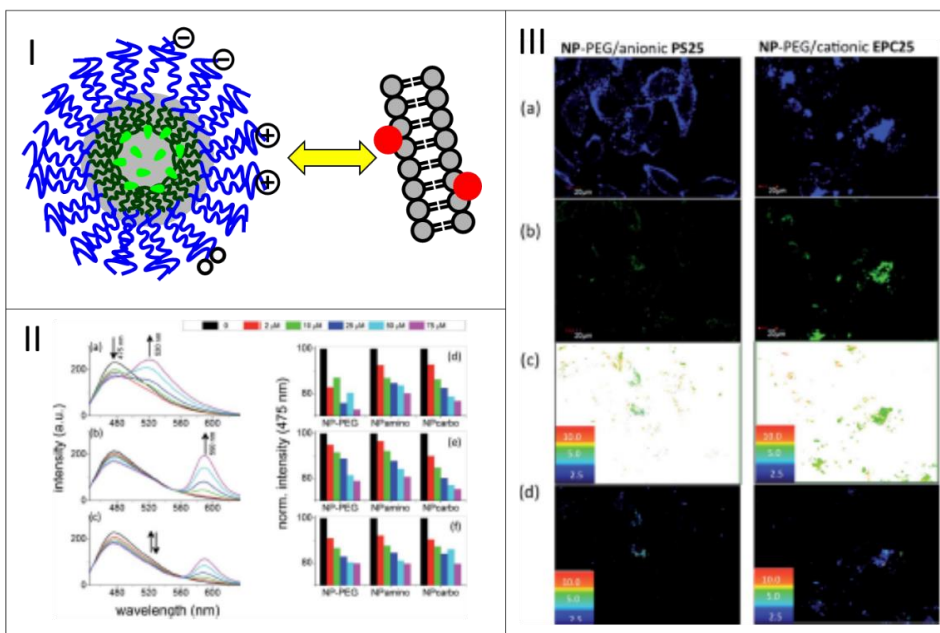


Figure 9. I) Schematic representation of PluSNPs with different charge and the dye labeled lipid bilayer. II) Emission spectra of different surface charge PluSNPs and different kind of lipid bilayer and their relative Energy Transfer efficiencies. III) investigation intracellular energy transfer of PluSNPs and lipid bilayer.

By changing the surface properties of the nanoparticles it was possible to drive their interaction with biological compartments, to increase for example the accumulation in lymph node or to enhance the cellular uptake by endocytosis^{22–24}. These investigations showed how the nanoparticles in the biological media can form a bioinorganic interface which can control many aspects of the PluSNP bioavailability. The PluSNPs surface composition seem to be very important to develop tools able to understand and model the interaction between nanoparticle and biomacromolecules. A solution to prove the interaction of PluSNPs with biomacromolecules can be provided by fluorescence, a technique able to demonstrate nanoparticle-macromolecule interactions for examples exploiting the colocalization of two fluorophores (Energy Transfer).

Fluorescence is also able to map nano-polarities (solvatochromism) and to observe the motion of nanoobjects in solution as well as in complex systems as the cellular media (Fluorescence Correlation Spectroscopy, FCS).

REFERENCES

- 1 W. Arap, R. Pasqualini, M. Montalti, L. Petrizza, L. Prodi, E. Rampazzo, N. Zaccheroni and S. Marchiò, *Curr. Med. Chem.*, 2013, **20**, 2195–211.
- 2 S. W. Bae, W. Tan and J.-I. Hong, *Chem. Commun.*, 2012, **48**, 2270.
- 3 M. S. Bradbury, E. Phillips, P. H. Montero, S. M. Cheal, H. Stambuk, J. C. Durack, C. T. Sofocleous, R. J. C. Meester, U. Wiesner and S. Patel, *Integr. Biol.*, 2013, **5**, 74–86.
- 4 S. Prilloff, M. I. Noblejas, V. Chedhomme and B. A. Sabel, *Eur. J. Neurosci.*, 2007, **25**, 3339–3346.
- 5 M. Miragoli, P. Novak, P. Ruenraroengsak, A. I. Shevchuk, Y. E. Korchev, M. J. Lab, T. D. Tetley and J. Gorelik, *Nanomedicine (Lond.)*, 2013, **8**, 725–37.
- 6 P. Wu and X.-P. Yan, *Chem. Soc. Rev.*, 2013, **42**, 5489.
- 7 M. Ma, H. Chen, Y. Chen, K. Zhang, X. Wang, X. Cui and J. Shi, *J. Mater. Chem.*, 2012, **22**, 5615.
- 8 P. M. Montalti, .
- 9 D. Bobo, K. J. Robinson, J. Islam, K. J. Thurecht and S. R. Corrie, *Pharm. Res.*, 2016, **33**, 2373–2387.
- 10 J. Choi, A. A. Burns, R. M. Williams, Z. Zhou, A. Flesken-Nikitin, W. R. Zipfel, U. Wiesner and A. Y. Nikitin, *J. Biomed. Opt.*, 2007, **12**, 64007.
- 11 J. H. Ryu, H. Koo, I. C. Sun, S. H. Yuk, K. Choi, K. Kim and I. C. Kwon, *Adv. Drug Deliv. Rev.*, 2012, **64**, 1447–1458.
- 12 M. a Dobrovolskaia, P. Aggarwal, J. B. Hall and S. E. Mcneil, *Mol. Pharm.*, 2009, **5**, 487–495.

- 13 A. Burns, P. Sengupta, T. Zedayko, B. Baird and U. Wiesner, *Small*, 2006, **2**, 723–726.
- 14 L. Wang and W. Tan, *Nano Lett.*, 2006, **6**, 84–88.
- 15 J. Yan, M. C. Estévez, J. E. Smith, K. Wang, X. He, L. Wang and W. Tan, *Nano Today*, 2007, **2**, 44–50.
- 16 M. Mahmoudi, H. Hofmann, B. Rothen-Rutishauser and A. Petri-Fink, *Chem. Rev.*, 2012, **112**, 2323–2338.
- 17 X. He, H. Nie, K. Wang, W. Tan, X. Wu and P. Zhang, 2008, **80**, 9597–9603.
- 18 A. a Burns, J. Vider, H. Ow, E. Herz, O. Penate-medina, M. Baumgart, S. M. Larson, U. Wiesner and M. Bradbury, *Nano Lett.*, 2009, **9**, 442–448.
- 19 D. Genovese, S. Bonacchi, R. Juris, M. Montalti, L. Prodi, E. Rampazzo and N. Zaccheroni, *Angew. Chemie - Int. Ed.*, 2013, **52**, 5965–5968.
- 20 E. Rampazzo, E. Brasola, S. Marcuz, F. Mancin, P. Tecilla and U. Tonellato, *J. Mater. Chem.*, 2005, **15**, 2687.
- 21 T. Suteewong, H. Sai, R. Cohen, S. Wang, M. Bradbury, B. Baird, S. M. Gruner and U. Wiesner, *J. Am. Chem. Soc.*, 2010, **133**, 172–175.
- 22 M. Helle, E. Rampazzo, M. Monchanin, F. Marchal, F. Guillemin, S. Bonacchi, F. Salis, L. Prodi and L. Bezdetsnaya, *ACS Nano*, 2013, **7**, 8645–8657.
- 23 S. Biffi, L. Petrizza, E. Rampazzo, R. Voltan, M. Sgarzi, C. Garrovo, L. Prodi, L. Andolfi, C. Agnoletto, G. Zauli and P. Secchiero, *RSC Adv.*, 2014, **4**, 18278–18285.
- 24 E. Rampazzo, R. Voltan, L. Petrizza, N. Zaccheroni, L. Prodi, F. Casciano, G. Zauli and P. Secchiero, *Nanoscale*, 2013, **5**, 7897.

CHAPTER 3

Shell Nanopolarities of Pluronic Silica nanoparticles

Polarity and proticity of confined nanoenvironments are able to tune the strength of noncovalent interactions such as H-bonds, electrostatic and van der Waals interactions or π - π stacking; as such, they play a fundamental role in many chemical and biochemical processes that are driven by local environmental heterogeneity, such as enzymatic catalysis,¹⁻⁴ molecular recognition, self-assembly of polymers, micelles and vesicles,⁵ molecular transport and delivery,⁶ and bottom-up formation of nanostructures and nanomaterials.⁷⁻¹⁰

Nanomaterials are expressing a rich potential in as much as they can implement such polarity heterogeneity at the nanoscale, featuring several environments with different physicochemical properties in a single structure. This richness, which can be compared to the complexity of biological species such as proteins and DNA, is at the basis of their peculiar versatility and of their ability to perform complex functions, such as drug delivery and targeted transport,^{6, 11-13} adsorption of pollutants,¹⁴ adhesion,¹⁵ and colloidal stabilization.¹⁵⁻¹⁶

Despite the extensive production of novel nanomaterials composed of several compartments with different polarities,^{13, 17} the characterization of polarity distribution in such a confined space is difficult and often remains an assumption based on chemical structure and morphology of these nanoarchitectures. Fluorescent solvatochromic dyes have been used in seminal works to investigate polarity of micelles and vesicles.¹⁸⁻¹⁹ Similar information could also be sought for more elaborate nanomaterials composed of multiple domains. Nonetheless, the complexity of such architectures makes it difficult to obtain a correct description of the multiple nanoenvironments, and to distinguish which environment is actually

being probed by the dye. The current models used to describe micropolarity, based on the Kamlet-Taft parameters, provide only an average description of polarity and proticity of the microenvironments.²⁰⁻²⁹ Some efforts have also been done to isolate the contribution of the bulk solvent.³⁰ A correct description of complex multicompartment nanostructures, on the contrary, requires to find unambiguous interpretation of multi-component fluorescence data. In this contribution, we describe a method based on spectral deconvolution and FRET analysis that yields polarity mapping of complex nanoarchitectures. Our approach overcomes the limits of current methods based on Kamlet-Taft parameters, since it allows to simultaneously quantify and visualize a wide range of polarities featured by the nanomaterial, and in addition it yields space-correlation of polarity and proticity information from compartments located few nanometers apart. In a first step we perform spectral deconvolution of the emission spectra of solvatochromic fluorescent probes: the complex spectrum of each solvatochromic probe in a multicompartment nanostructure is fitted using a set of spectra of the same probe in pure solvents, yielding coefficients that quantify the fraction of dyes probing similar polarity as that of the pure solvents inside the nanostructure. The number and type of solvents used for the fitting set determines the resolution of the technique and should be adequately chosen according to the polarity gradient to be explored and quantified. With the second step, the method allows to reconstruct the approximate distance between probed compartments: this result is achieved upon careful selection of at least two solvatochromic fluorescent dyes with suitable photophysical features and exploiting the occurrence of energy transfer from and to the probes. The multiple FRET contributions are sorted by polarity via spectral deconvolution. As a result, estimation of energy transfer efficiency for each individual spectral component of the probes yields fine mapping of nanoenvironment polarities within the nanostructure. We test this method by investigating a multilayer nano-architecture composed of

a silica core grown into a micelle of triblock copolymer Pluronic F127, previously named “PluS NPs”.³¹⁻³² It has been shown that this nanomaterial is composed of a dense silica core and of a soft polymeric shell, which among other things is responsible for the long term colloidal stability in water, and for the ability of these nanoparticles to host hydrophobic moieties close to the internal silica core.³³⁻³⁴ The shell should hence display both hydrophobic hosting sites and a hydrophilic surface ensuring favorable interaction with external water (figure 1 and figure Technical Notes 1). Despite the large knowledge on structure, behavior and abilities of this nanoarchitecture, the intimate distribution of its environments with different polarity and proticity still remains to be elucidated. Previous knowledge on morphology and on chemical properties of the components suggests a possible model for the nanoarchitecture that consists of a dense silica shell, in which the hydrophobic polypropylene oxide (PPO) segments are deeply buried, and of a permeable soft polymeric shell.^{31, 33, 35} The shell itself might be composed of two sections: a hydrophobic inner layer close to the silica, made of PPO (the part that is not completely buried in the silica network) and an outer layer made of the PEG terminations, which could be partly hydrated owing to its good affinity with water.

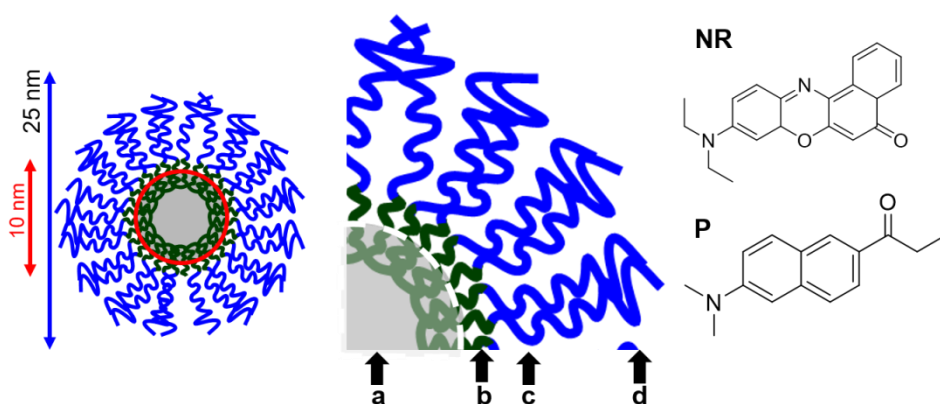


*Figure 1 – Cartoon of multicompartment nanostructures PluS NPs (left and center) probed by the luminescent solvatochromic dyes **P** and **NR** (right). Letters a-d indicate the compartments presumed from the known morphology, specifically: a) dense silica core embedding PPO chains; b) PPO brushes emerging from the silica core; c) interfacial region with PPO and PEG; d) external layer with PEG brushes.*

We select two well-known solvatochromic probes, i.e. Nile Red (**NR**) and Prodan (**P**) owing to their respective polarity and spectral features. They share a distinct preference for hydrophobic environments, even though they are partly soluble and emissive in polar solvents, with **P** in particular providing an appreciable signal also in water (see table 1). Furthermore, the emission spectra show almost no overlap, even accounting for the whole range of polarities that can be explored by each probe (figure 2), which allows for sensitive quantification of all polarity-dependent signals owing to the very low crosstalk. Finally, Forster Radius R_0 for **P-NR** couple is quite large and almost constant for all combinations of environments, due to the fact that spectral overlap increases in polar solvents, where quantum yield of the donor decreases (see table 2): the uniform R_0 allows to trace back the distance between different compartments via accurate estimation of FRET efficiency between dyes. The probes were added to the solution of NPs via addition of small aliquots of a concentrated acetonitrile solution (1 mM), which did not interfere with the nanoarchitecture. Neither of the two probes displays aggregation in the concentration range used in this study, therefore reported spectral observations are unequivocally ascribed to change of polarity and proticity of the nanoenvironment.

3.1 SPECTRAL FITTING

Quantification of number and polarity of probed hosting sites is a key step of this work. First, we measure the emission spectra $S_i(\lambda)$ of **NR** and **P** at a fixed concentration in a set of 5 reference environments i (the pure solvents toluene, dichloromethane, acetonitrile, methanol and water, respectively indicated as t , d , a , m , and w), covering a broad range of polarities and protic levels. Then, we use such reference spectra $S_i(\lambda)$ to fit the emission spectra of **NR** and **P** in the multicompartment nanostructure $PlusNP(\lambda)$: this yields the coefficients c_i that quantify the fraction of dye probing the polarity and proticity of the i^{th} environment (eq. 1).

$$PlusNP(\lambda) = \sum_{i=1}^n c_i S_i(\lambda) \quad (\text{eq. 1})$$

It has to be noted that the complex information obtained with this method is highly reproducible and that it can also be obtained for other nanostructures, opening the way for quantitative comparison of polarity and proticity of nanomaterials, not limited to description of average polarity.

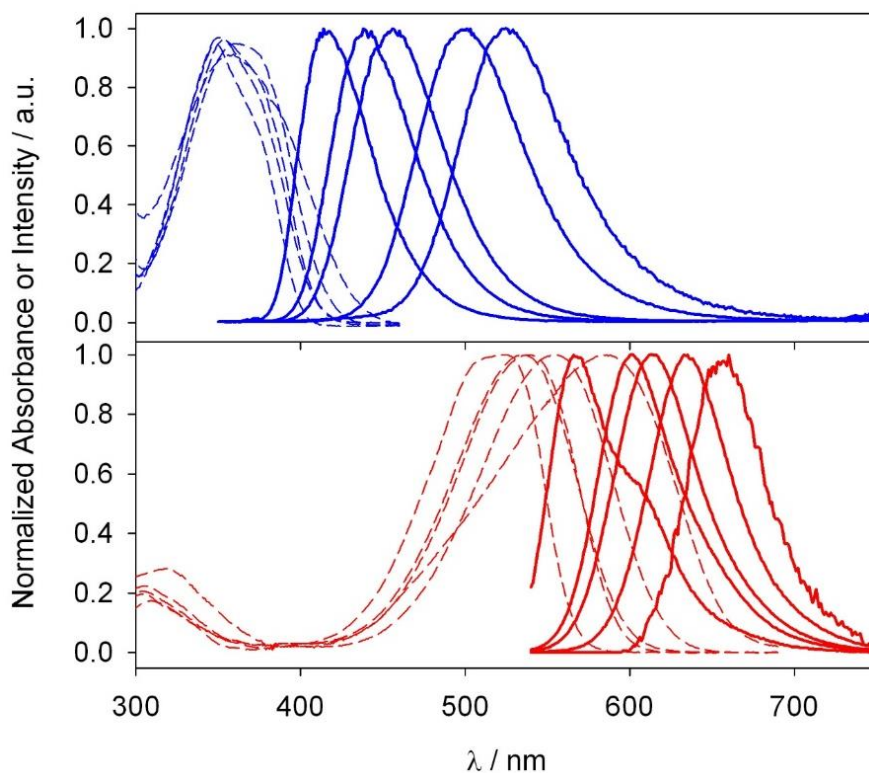


*Figure 2 – Absorption (dashed lines) and emission spectra (solid lines) of **P** (a) and **NR** (b) in toluene, dichloromethane, acetonitrile, methanol and water (bands shifting from left to right respectively). All spectra are normalized; note that intensity of Nile Red emission in water is extremely weak compared to other solvents (see quantum yields in table 2) The not-normalized emission spectra are used in equation 1 as $S_t(\lambda)$, $S_d(\lambda)$, $S_a(\lambda)$, $S_m(\lambda)$, and $S_w(\lambda)$ (Figure 2 Technical Notes).*

3.2 SOLVATOCHROMIC, ENERGY TRANSFER

Table 2 Photophysical data for the probes P and NR in the five solvents used in this study, i.e. toluene (*t*), dichloromethane (*d*), acetonitrile (*a*), methanol (*m*) and water (*w*).

		QY%	τ / ns	$\lambda_{em,max}$ /nm	$\lambda_{abs,max}$ /nm	ϵ / M ⁻¹ cm ⁻¹
PRODAN	<i>t</i>	56	2.21	414	348	18400
	<i>d</i>	98	3.20	438	353	24600
	<i>a</i>	95	3.30	456	350	21400
	<i>m</i>	77	2.57	501	360	19500
	<i>w</i>	25	0.98	524	359	13200
NILE RED	<i>t</i>	80	3.97	566	535	29500
	<i>d</i>	78	4.52	600	538	35500
	<i>a</i>	76	4.63	613	556	38600
	<i>m</i>	40	2.76	633	526	32800
	<i>w</i>	0,5	0.55	660	588	14400

Table 3. – Forster Radii (Angstrom) for the FRET pair P-NR in the investigated solvent combinations

R0		PRODAN				
		<i>t</i>	<i>d</i>	<i>a</i>	<i>m</i>	<i>w</i>
NILE RED	<i>t</i>	29.7	40.7	43.6	46.4	37.2
	<i>d</i>	29.1	40.0	43.3	47.9	39.7
	<i>a</i>	29.1	40.1	43.5	48.3	40.1
	<i>m</i>	26.7	37.1	40.6	46.5	39.5
	<i>w</i>	24.5	33.4	36.0	40.8	35.0

Both **NR** and **P**, when added in small amounts to a water solution of Plus NPs (1*10⁻⁶M), find a heterogeneous variety of hosting sites to occupy and therefore generate complex and multicomponent signals. The information obtained by the two probes is

complementary since they exhibit different spectral responses and cover different ranges of polarity. The gradual shift of the emission maximum displayed by **NR** upon increasing its concentration in presence of PluS NPs reveals that polarity of populated hosting sites shifts progressively from an environment similar to toluene to one comparable to methanol (see normalized emission spectra in figure 3b, not normalized spectra are reported in figure SI3). On the other hand, **P** displays a peculiar emission spectrum with two well separated bands, which respectively report on aprotic (higher energy emission band) and protic microenvironments (lower energy emission band).¹⁸⁻¹⁹ Interestingly, each band is also sensitive to polarity, so that it is possible to distinguish between strongly and mildly apolar environments (corresponding to toluene and dichloromethane in our set of 5 solvents references) and between mildly and strongly hydrophilic sites, up to a purely aqueous environment (acetonitrile, methanol and water, see figure 3a). Differently from **NR**, **P** displays even at the lowest concentration a significant contribution of polar protic environments (lower energy band), whose weight increases with **P** concentration and that concomitantly shows a relevant bathochromic shift (figure 3a).

Coefficients found upon fitting the experimental emission spectra of **P** and **NR** show comparable trends: coefficients of toluene and dichloromethane (c_t and c_d) show an initially high slope (indicating efficient population of hydrophobic hosting sites) which decreases until reaching a plateau at high probe concentration, indicating that such hydrophobic sites are soon saturated by the probes. On the other hand, the more hydrophilic hosting sites, which are here monitored via the coefficients of acetonitrile and methanol (c_a and c_m respectively) are able to host a larger number of dyes: the coefficients c_a and c_m overcome c_t and c_d respectively, when these latter go towards a plateau. This analysis thus shows that the two solvatochromic probes **P** and **NR** are first hosted by both hydrophilic and hydrophobic sites of PluS NPs, with a preference for

hydrophobic sites; then, at higher probe concentration, hydrophobic sites are saturated, and the probes largely populate hosting sites that are as hydrophilic and protic as methanol environment. **P** also feature a rather large coefficient for water (c_w) since the very first additions, which deserves separate considerations (see trend of c_w in figure 3). **P** is indeed clearly reporting on a water-like microenvironment: this might correspond to either a water pocket inside the PEG shell, or simply to bulk water outside Plus NPs.

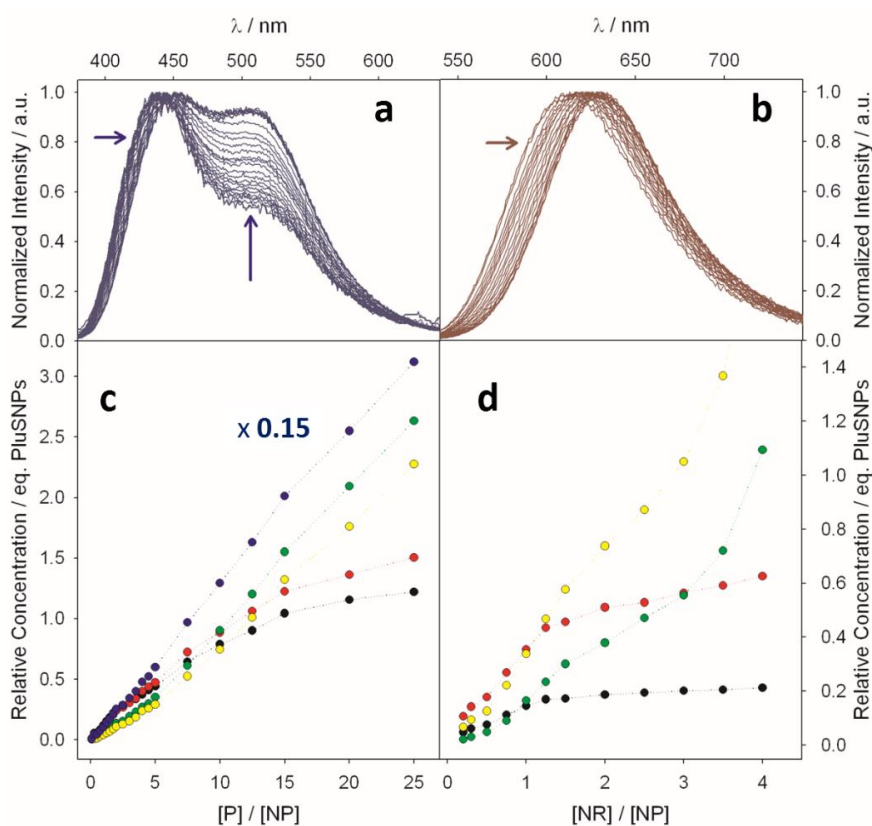


*Figure 3 – Normalized emission spectra of titration of Plus NPs with **P** (a) and **NR** (b) and fitting coefficients of the spectral components relative to toluene (c_t , black), dichloromethane (c_d , red), acetonitrile (c_a , green), methanol (c_m , yellow) and water (c_w , blue),*

*obtained from the not-normalized emission spectra of titration of Plus NPs with **P** (c) and **NR** (d).*

The presence of water molecules inside the PEG shell is crucial for many applications of Plus NPs and of PEG stabilized nanostructures in general: they can for instance be involved in catalytic reactions taking place in the nanocompartment, they can stabilize or decompose hosted drugs, they can regulate kinetics of delivery or transport and permeation of small molecules and ions inside nanostructures.³⁶⁻³⁷ To determine whether the polar protic environments (here quantitatively described by coefficients c_m and c_w) are reporting on hydration molecules inside PEG shell or on bulk water outside the Plus NPs, we developed an approach based on FRET between different solvatochromic probes, which unambiguously localize the hydrated compartments relative to the hydrophobic ones. To this aim, we loaded $5 \cdot 10^{-6} \text{M}$ **P** in Plus NPs, corresponding to 5 **P** dyes per NP, so that environments probed by the donor **P** dyes in these conditions cover all polarities, including water. Then, we added increasing amounts of **NR** to this system, following its localization via its selective excitation at 520 nm (Figure 11 Technical Notes). Interestingly, upon addition of **NR** and direct excitation of **P** at 330 nm, we observe a pronounced quenching of **P** emission and a concomitant sensitization of **NR**. This preliminary observation confirms that the two probes are located in compartments within the same nanostructure and thus close enough to transfer energy quite efficiently, also owing to their rather large R_0 (table 2).

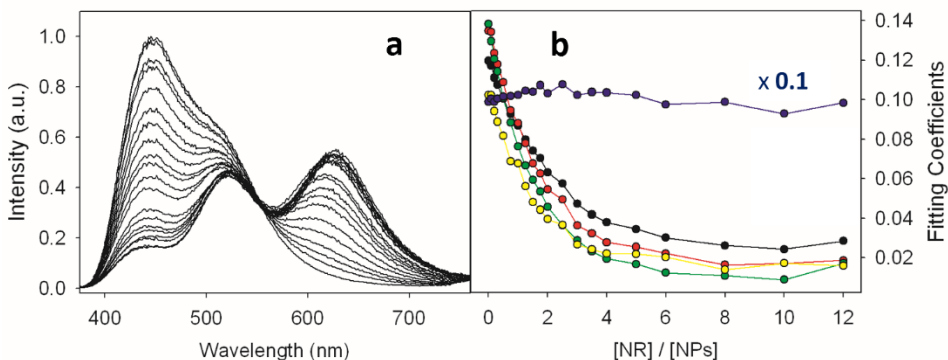


*Figure 4 –Normalized emission spectra (a) and fitting emission coefficients (b) of FRET titration of PluS NPs and **P** ($5 \cdot 10^{-6}M$) with increasing amounts of **NR** (from 0.1 to $12 \cdot 10^{-6}M$).*

Beside this general observation, the spectral deconvolution method here developed allows to resolve the various polarities probed by **P** and **NR**, and consequently to resolve FRET efficiency as a function of the microenvironment. This procedure opens the way to a fine understanding of the system, since it reveals whether **P** is transferring energy to **NR** from all probed compartments, including the hydrated (protic) ones, quantitatively described by c_m and c_w . We analyze the quenching of **P** after separating its complex emission spectrum in the 5 components and then we follow the trend of the coefficients, with particular attention to c_m and c_w . Interestingly, while the coefficients c_t , c_d , c_a and c_m are heavily depleted by the increasing concentration of **NR**, c_w is independent on it and remains substantially constant (Figure 4b). This analysis leads to two important findings: first, 4 very different nanoenvironments in terms of polarity and proticity are very close to each other, within few nanometers distance (toluene, dichloromethane, acetonitrile and methanol); in particular, a compartment of PluS NPs features polar protic hosting sites (methanol nanoenvironments), which can be ascribed to PEG branches hydrated by a restricted number of water molecules;

second, the “water-like” compartment probed by **P** is far away from the other hydrophobic and hydrophilic sites hosting the **NR** dyes, and can therefore be ascribed to bulk water, external to the nanostructure; therefore, no water pockets are detected by **P** inside the nanostructure.

Finally, the method allows to perform an analogous polarity-resolved spectral analysis of FRET on the acceptor, **NR**. Deconvolution of directly excited **NR** spectra ($\lambda_{\text{exc}} = 520 \text{ nm}$) and of sensitized **NR** spectra (i.e., excited via FRET from **P**, $\lambda_{\text{exc}} = 330 \text{ nm}$) provides coefficients of environments probed by **NR** and coefficients of the environments in which **NR** accepts energy from **P**, respectively. Quantitative comparison of such coefficients reveals that all components of **NR** are equally sensitized by **P**, confirming that all emissive **NR** probes are distributed inside the various compartments of Plus NPs –from apolar (c_t and c_d) to polar (c_a) and polar protic ones (c_m) – (Figure 11 Technical Notes).

The highly informative results collected with this method demonstrate that the two-compartment model (silica core / PEG shell) used so far to describe the Plus NP architecture is by far too simplified. A variety of nanoenvironments were probed and localized within the nanostructure, featuring very different polarity and proticity. A more rigorous description of the system should hence consider a small apolar region (matching with the inner layer of dense, not hydrated PPO), and an increasingly polar layer (ascribable to the PEG branches) with a volume able to host tens of dyes. The polar layer reaches, in the outer part, a very high polarity and proticity, comparable to the ones of methanol: this finding allows us to ascribe this nanoenvironment to strongly hydrated PEG branches.

3.3 CONCLUSION

In conclusion, we developed a new method to investigate the multifaceted polarity and proticity of complex nanostructures, with the unique ability of co-localizing the different probed environments.

The method is based on the use of at least two solvatochromic fluorescent probes with suitable photophysical properties (including similar R_0 for all combinations of environments) to efficiently exchange energy via FRET. These species can hence (i) report on multiple environments to be found in the nanoarchitectures, and (ii) colocalize the various environments via FRET. The method has been tested here on a well-known multicompartment nanomaterial –PluS NPs– using two solvatochromic probes –Prodan and Nile Red–. I found a wide range of polarities, ranging from apolar, to polar, and also to polar protic nanoenvironments, within R_0 distance, ascribable to dense PPO, PEG and to partly hydrated PEG branches respectively. In addition, it was possible to experimentally prove that the component similar to water does not belong to the nanostructure, but it is merely due to bulk water.

This simple method is general and can be applied in a versatile, modular fashion to a broad range of nanomaterials. We believe that it could be of inspiration for a wide scientific community involved in fabricating, investigating and using nanostructured materials, since understanding polarity distribution in these systems is essential to grasp their potential in a variety of fields and applications, ranging from their use as nanoreactors and artificial enzymes, to molecular adsorption, storage and release such as required in drug delivery applications.

3.4 EXPERIMENTAL METHODS

Synthesis of PluS NPs: Plus NPs are synthesized as reported in previous papers.³² Briefly, Tetraethylorthosilicate (TEOS, 180 μL , 0.8 mmol) was added to an acidic aqueous solution (Acetic Acid 1M) of Pluronic F127 (100 mg) and NaCl (67 mg) under magnetic stirring, and its hydrolysis and condensation was allowed to proceed for 3 hours. Trimethylsilylchloride (TMSCL, 10 μL , 0.08 mmol) was then added and the solution was stirred overnight. So, obtained Plus NPs solution was purified via dialysis for at least 4 days, using RC membrane (cut off 12 KDa) against water. The solution in the membrane was recovered and diluted to 10 ml to obtain a final concentration of the nanoparticles of 10 μM .³³ The morphology of PluS NPs was characterized with DLS and TEM, yielding the hydrodynamic radius ($R_h = 13$ nm, polydispersity index $PdI = 0.11$) and the diameter of the silica core ($d_c = 11 \pm 1$ nm), respectively. A representative TEM image used for image analysis is shown below.

Fluorescence titrations of PluS NPs with solvatochromic probes: 2.5 mL of 1×10^{-6} M solution of PluS NPs in water was titrated with a small amount (1 μL to 50 μL) of a millimolar acetonitrile solution of solvatochromic dye (**P** or **NR**). Absorption spectra were recorded on a Perkin Elmer Lambda45 spectrophotometer, while emission spectra were recorded on an Edinburgh F900 fluorometer equipped with a photomultiplier Hamamatsu R928P. FRET experiments were performed by titrating an aqueous solution of PluS NPs 1×10^{-6} M and **P** 5×10^{-6} M with a millimolar solution of **NR** in acetonitrile.

Data analysis: spectral deconvolution was performed through the fitting algorithm of SigmaPlot (Systat Software Inc., Technical Notes) following eq. 1. The input spectra $S_i(\lambda)$ were recorded at equimolar concentration of solvatochromic probe in the five selected solvents, using constant instrumental conditions and excitation wavelengths ($\lambda_{\text{exc}} = 330$ nm for **P** and $\lambda_{\text{exc}} = 520$ nm for **NR**). The water component

is not used to fit **NR** emission spectra, due to the very low quantum yield and solubility of this solvatochromic probe in this solvent.

3.5 TECHNICAL NOTES

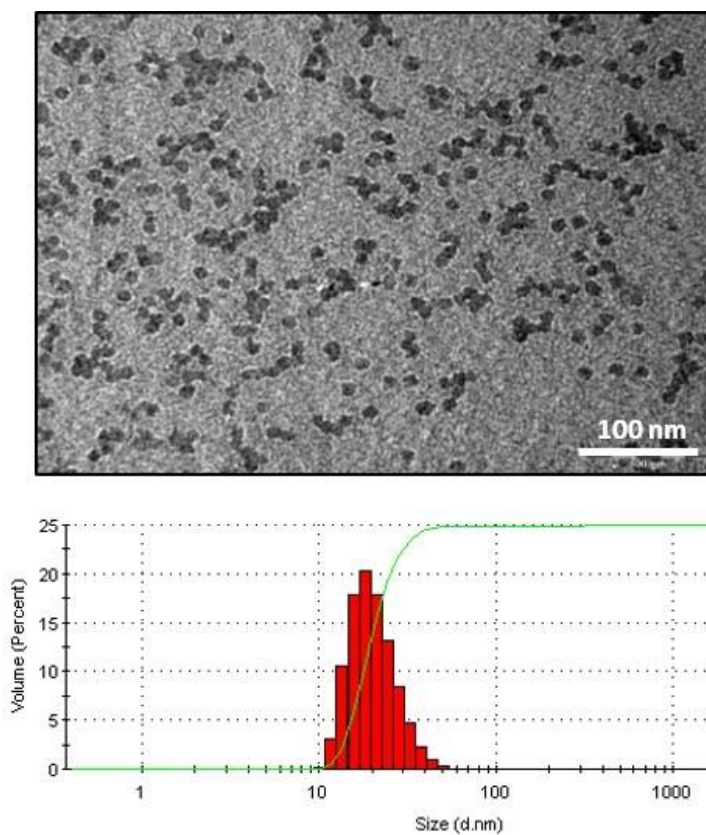


Figure 5 TEM micrograph (top) and hydrodynamic diameter distribution as obtained by DLS measurements (bottom).

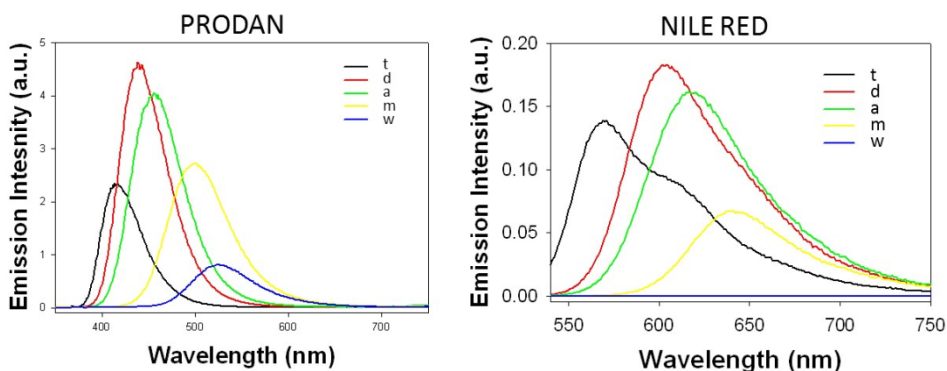


Figure 6. Emission spectra of equimolar solutions of Prodan (left) and Nile Red (right) in the five solvents used in this study (t=toluene, d=dichloromethane, a=acetonitrile, m=methanol, w=water). Excitation wavelength is 330 nm and 520 nm for Prodan and Nile Red respectively

Curve-fitting Algorithm

The SigmaPlot curve fitter uses the Marquardt-Levenberg algorithm to find the coefficients (parameters) of the independent variable(S) that give the best fit between the equation and the data. This algorithm seeks the values of the parameters that minimize the sum of the squared differences between the values of the observed and predicted values of the dependent variable.

$$SS = \sum_{i=0}^n W_i (y_i - y_2)^2 \quad (\text{eq 2})$$

where y_i is the observed and y_i is the predicted value of the dependent variable. This process is iterative the curve fitter begins with a guess at the parameters, checks to see how well the equation fits, then continues to make better guesses until the

differences between the residual sum of squares no longer decreases significantly. This condition is known as convergence.

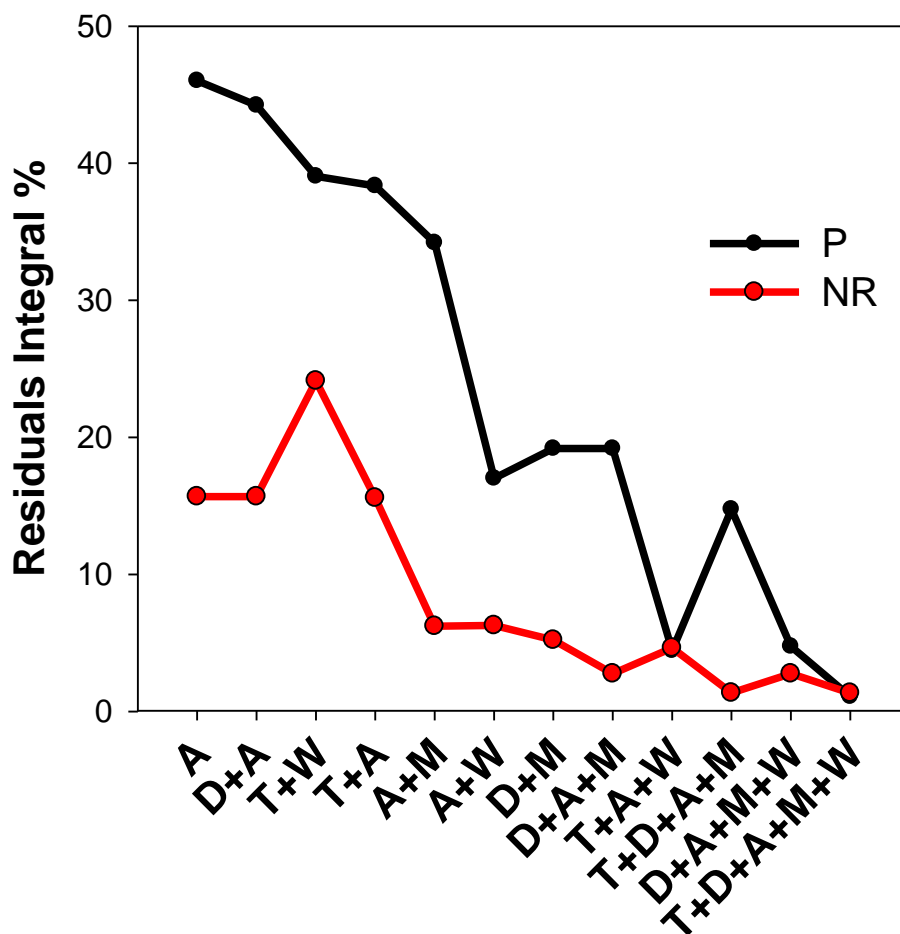


Figure 7. Trends of Residuals Integral% (Residuals integral/ Experimental Spectrum Integral *100) of the fitting with different basis sets for Prodan (black line) and Nile Red (red line) $5 \cdot 10^{-6} M$ in presence of PluSNPs $1 \cdot 10^{-6} M$

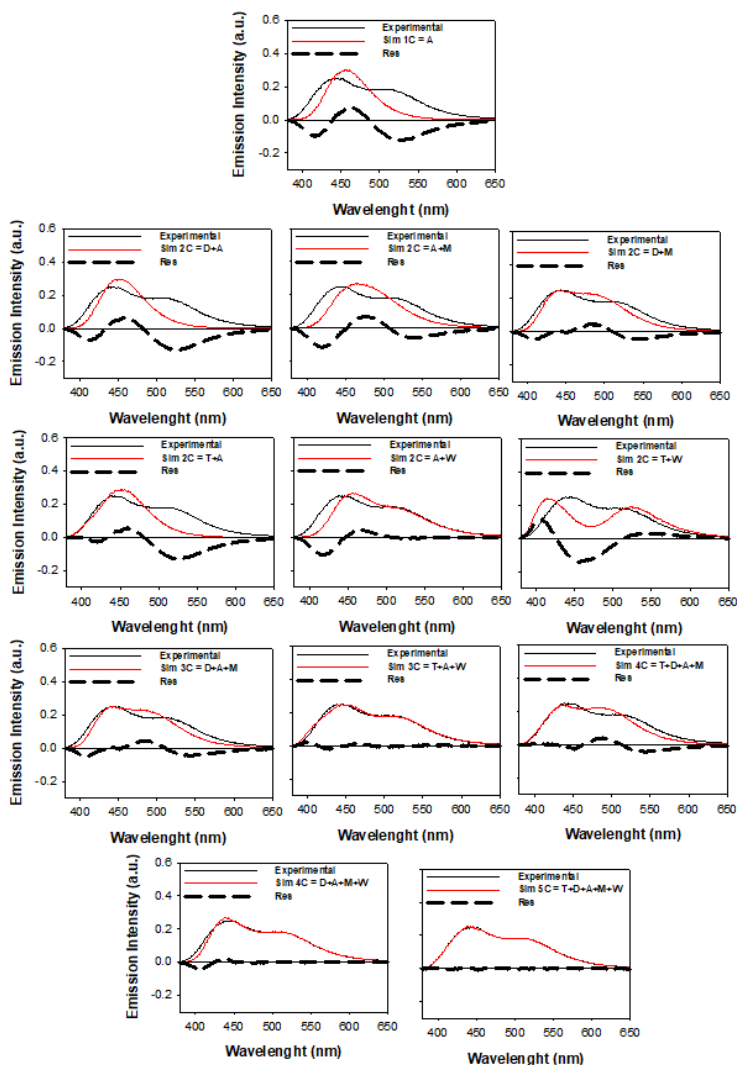


Figure 8. Display of the fitting combinations for Prodan $5 \cdot 10^{-6} M$ in presence of $1 \cdot 10^{-6} M$ of PluSNPs. From the top to the bottom different composition of the basis set for the fitting are showed, in particular, from one component A to the five components T, D, A, M and W. the black solid line represent the experimental spectra in red the fitted one. The dashed black line rapresent the residuals (Fitted-Experimental Spctra).

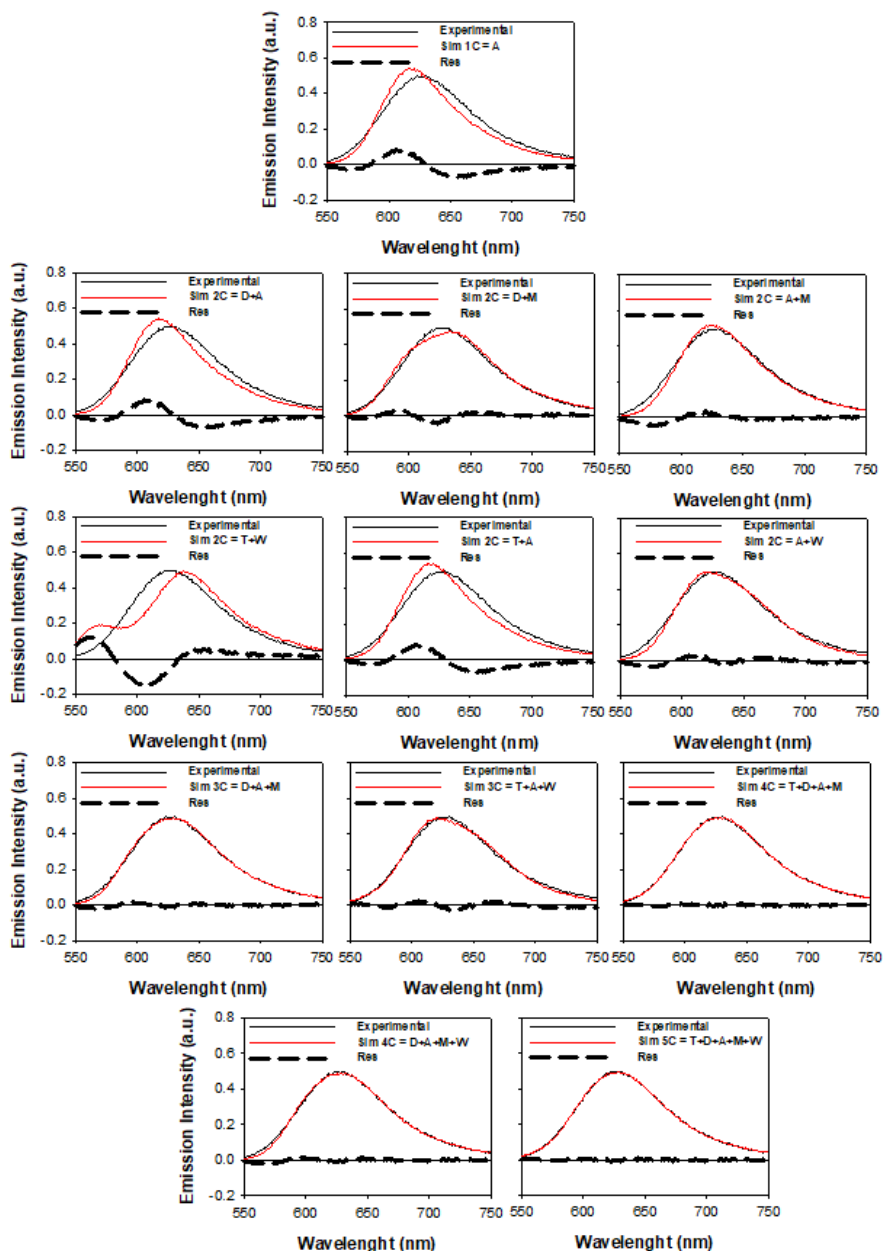


Figure 9. Display of the fitting combinations for Nile Red $5 \cdot 10^{-6} M$ in presence of $1 \cdot 10^{-6} M$ of PluSNPs. From the top to the bottom different composition of the basis set for the fitting are showed, in

particular, from one component A to the five components T, D, A, M and W. the black solid line represent the experimental spectra in red the fitted one. The dashed black line represent the residuals (Fitted -Experimental spectra).

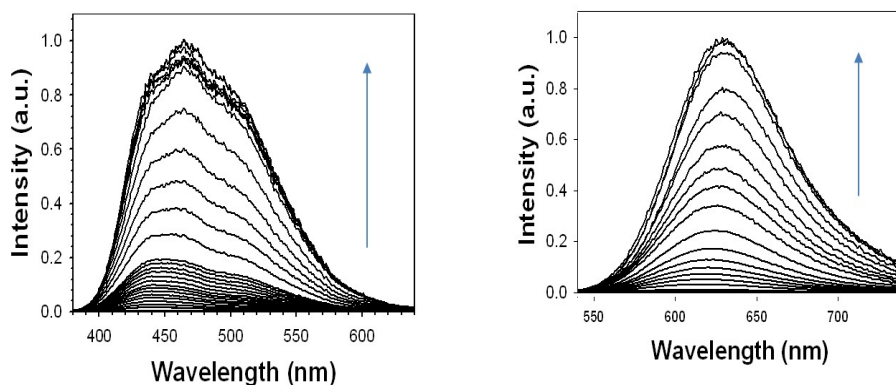


Figure 10. Emission spectra of PluS NPs 10^{-6} M in water titrated with Prodan (excitation wavelength 330 nm, left) or with Nile Red (excitation wavelength 520 nm, right).

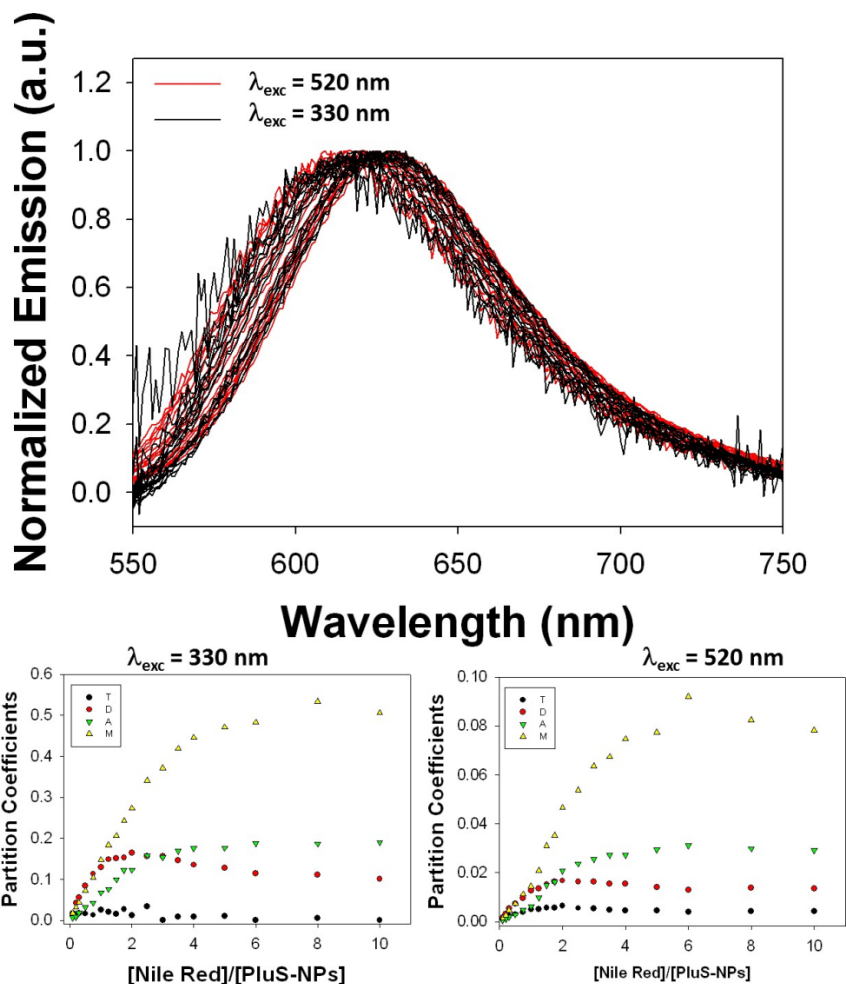


Figure 11. Top graph: Emission spectra of Nile Red added to a solution containing PluS NPs 10^{-6} M and Prodan $5 \cdot 10^{-6}$ M, excited directly at 520 nm (red spectra) or excited via FRET through Prodan at 330 nm (black spectra). The latter spectra were obtained by measuring the overall emission spectra which includes emission from Prodan (shown in figure 4), followed by fitting the spectra with the nine spectral components (5 for Prodan and 4 for Nile Red), and finally subtracting the emission components relative to Prodan to the original spectra shown in figure 4, hence yielding uniquely the Nile

Red emission. Bottom graphs: fitting coefficients ct , cd , ca and cm obtained for emission spectra reported above, i.e. for sensitized (left) and for directly excited Nile Red (right).

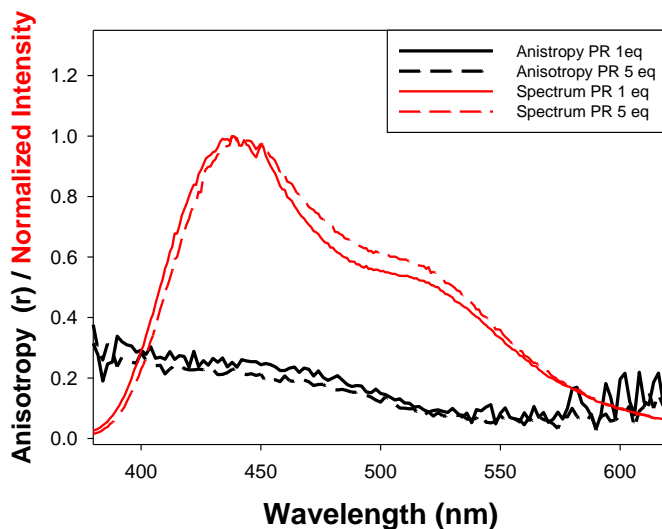


Figure 12. Fluorescence Anisotropy (black line) and Normalized Fluorescence Emission intensity (red line) of Prodan 1 and $5 \cdot 10^{-6}$ M (solid and dashed respectively) added to $1 \cdot 10^{-6}$ M of PluSNPs. ($\lambda_{ex}=330$ nm)

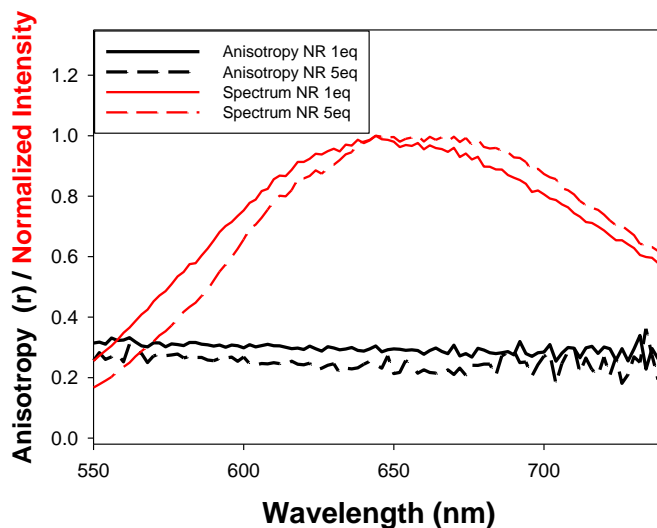


Figure 13. Fluorescence Anisotropy (black line) and Normalized Fluorescence Emission intensity (red line) of Nile Red 1 and 5×10^{-6} M (solid and dashed respectively) added to 1×10^{-6} M of PluSNPs. ($\lambda_{ex}=520$ nm)

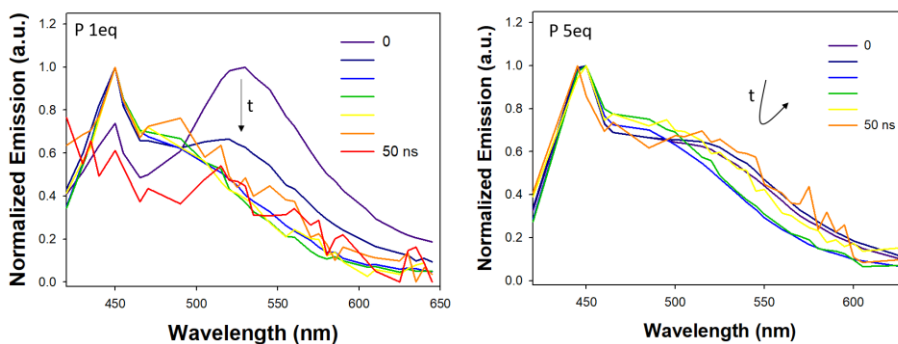


Figure 104. Time Resolved Spectral Emission of Prodan 1 eq. and 5 eq. respect to 1×10^{-6} M of PluSNPs ($\lambda_{ex}=405$ nm)

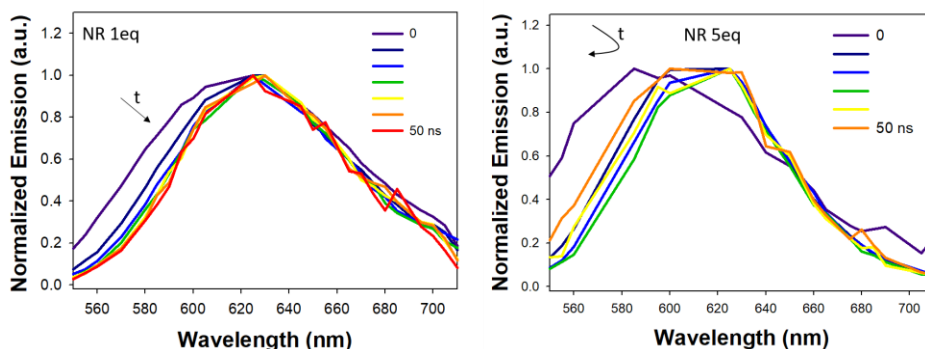


Figure 11. Time Resolved Spectral Emission of Nile Red 1 eq. and 5 eq. respect to $1 \cdot 10^{-6} M$ of PluSNPs ($\lambda_{ex}=405 \text{ nm}$)

REFERENCES

The contents of this chapter are based on Francesco Palomba, Luca Petrizza, Enrico Rampazzo, Nelsi Zaccheroni, Damiano Genovese and Luca Prodi, “Mapping heterogeneous nanopolarity in multicompart ment nanoarchitectures”, submitted at Journal of Physical Chemistry Letters.

1. Mertz, E. L.; Krishtalik, L. I., Low dielectric response in enzyme active site. *PNAS* **2000**, *97* (5), 2081-2086.
2. Affleck, R.; Xu, Z. F.; Suzawa, V.; Focht, K.; Clark, D. S.; Dordick, J. S., Enzymatic catalysis and dynamics in low-water environments. *PNAS* **1992**, *89* (3), 1100-1104.
3. Michels, P. C.; Dordick, J. S.; Clark, D. S., Dipole Formation and Solvent Electrostriction in Subtilisin Catalysis. *J. Am. Chem. Soc.* **1997**, *119* (40), 9331-9335.

4. de Visser, S. P.; Shaik, S., A Proton-Shuttle Mechanism Mediated by the Porphyrin in Benzene Hydroxylation by Cytochrome P450 Enzymes. *J. Am. Chem. Soc.* **2003**, *125* (24), 7413-7424.
5. Mai, Y.; Eisenberg, A., Self-assembly of block copolymers. *Chem. Soc. Rev.* **2012**, *41* (18), 5969-5985.
6. Ulbrich, K.; Holá, K.; Šubr, V.; Bakandritsos, A.; Tuček, J.; Zbořil, R., Targeted Drug Delivery with Polymers and Magnetic Nanoparticles: Covalent and Noncovalent Approaches, Release Control, and Clinical Studies. *Chem. Rev.* **2016**, *116* (9), 5338-5431.
7. Whitesides, G.; Mathias, J.; Seto, C., Molecular self-assembly and nanochemistry: a chemical strategy for the synthesis of nanostructures. *Science* **1991**, *254* (5036), 1312-1319.
8. Reinhoudt, D. N.; Crego-Calama, M., Synthesis Beyond the Molecule. *Science* **2002**, *295* (5564), 2403-2407.
9. Lehn, J.-M., Toward Self-Organization and Complex Matter. *Science* **2002**, *295* (5564), 2400-2403.
10. Whitesides, G. M.; Boncheva, M., Beyond molecules: Self-assembly of mesoscopic and macroscopic components. *PNAS* **2002**, *99* (8), 4769-4774.
11. Tan, S.; Li, X.; Guo, Y.; Zhang, Z., Lipid-enveloped hybrid nanoparticles for drug delivery. *Nanoscale* **2013**, *5* (3), 860-872.
12. Swaminathan, S.; Garcia-Amoros, J.; Fraix, A.; Kandoth, N.; Sortino, S.; Raymo, F. M., Photoresponsive polymer nanocarriers with multifunctional cargo. *Chem. Soc. Rev.* **2014**, *43* (12), 4167-4178.
13. Talelli, M.; Barz, M.; Rijcken, C. J. F.; Kiessling, F.; Hennink, W. E.; Lammers, T., Core-crosslinked polymeric micelles: Principles, preparation, biomedical applications and clinical translation. *Nano Today* **2015**, *10* (1), 93-117.
14. Brandl, F.; Bertrand, N.; Lima, E. M.; Langer, R., Nanoparticles with photoinduced precipitation for the extraction of pollutants from water and soil. *Nat. Commun.* **2015**, *6*, 7765.
15. Dinsmore, A. D.; Hsu, M. F.; Nikolaides, M. G.; Marquez, M.; Bausch, A. R.; Weitz, D. A., Colloidosomes: Selectively Permeable

Capsules Composed of Colloidal Particles. *Science* **2002**, 298 (5595), 1006-1009.

16. Tohver, V.; Smay, J. E.; Braem, A.; Braun, P. V.; Lewis, J. A., Nanoparticle halos: A new colloid stabilization mechanism. *PNAS* **2001**, 98 (16), 8950-8954.

17. De Crozals, G.; Bonnet, R.; Farre, C.; Chaix, C., Nanoparticles with multiple properties for biomedical applications: A strategic guide. *Nano Today* **2016**, 11 (4), 435-463.

18. Klymchenko, A. S.; Duportail, G.; Demchenko, A. P.; Mély, Y., Bimodal Distribution and Fluorescence Response of Environment-Sensitive Probes in Lipid Bilayers. *Biophys. J.* **2004**, 86 (5), 2929-2941.

19. Krasnowska, E. K.; Gratton, E.; Parasassi, T., Prodan as a Membrane Surface Fluorescence Probe: Partitioning between Water and Phospholipid Phases. *Biophys. J.* **1998**, 74 (4), 1984-1993.

20. Sarkar, A.; Kedia, N.; Purkayastha, P.; Bagchi, S., UV-Vis spectral investigation of photophysical properties of a solvatochromic electron donor/acceptor dye within a reverse micelle domain. *Chem. Phys. Lett.* **2014**, 592, 138-143.

21. Picco, A. S.; Silbestri, G. F.; Falcone, R. D.; Azzaroni, O.; Ceolin, M.; Correa, N. M., Probing the microenvironment of unimicelles constituted of amphiphilic hyperbranched polyethyleneimine using 1-methyl-8-oxyquinolinium betaine. *Phys. Chem. Chem. Phys.* **2014**, 16 (26), 13458-13464.

22. Beld, J.; Cang, H.; Burkart, M. D., Visualizing the Chain-Flipping Mechanism in Fatty-Acid Biosynthesis. *Angew. Chem. Int. Ed.* **2014**, 53 (52), 14456-14461.

23. Pippa, N.; Kaditi, E.; Pispas, S.; Demetzos, C., PEO-b-PCL-DPPC chimeric nanocarriers: self-assembly aspects in aqueous and biological media and drug incorporation. *Soft Matter* **2013**, 9 (15), 4073-4082.

24. Baker, G. A.; Rachford, A. A.; Castellano, F. N.; Baker, S. N., Ranking Solvent Interactions and Dielectric Constants with

[Pt(mesBIAN)(tda)]: A Cautionary Tale for Polarity Determinations in Ionic Liquids. *ChemPhysChem* **2013**, *14* (5), 1025-1030.

25. Nizri, G.; Magdassi, S., Solubilization of hydrophobic molecules in nanoparticles formed by polymer–surfactant interactions. *J. Colloid Interface Sci.* **2005**, *291* (1), 169-174.

26. Voigt, I.; Simon, F.; Estel, K.; Spange, S., Structure and Surface Polarity of Poly(vinylformamide-co-vinylamine) (PVFA-co-PVAm)/Silica Hybrid Materials. *Langmuir* **2001**, *17* (10), 3080-3086.

27. Spange, S.; Schmidt, C.; Kricheldorf, H. R., Probing the Surface Polarity of Poly(α -amino acids) and α -Amino Acid Crystals with Genuine Solvatochromic Dyes. *Langmuir* **2001**, *17* (3), 856-865.

28. Rottman, C.; Grader, G.; Avnir, D., Polarities of Sol–Gel-Derived Ormosils and of Their Interfaces with Solvents. *Chem. Mater.* **2001**, *13* (10), 3631-3634.

29. Spange, S.; Zimmermann, Y.; Graeser, A., Hydrogen-Bond-Donating Acidity and Dipolarity/Polarizability of Surfaces within Silica Gels and Mesoporous MCM-41 Materials. *Chem. Mater.* **1999**, *11* (11), 3245-3251.

30. Vitha, M. F.; Weckwerth, J. D.; Odland, K.; Dema, V.; Carr, P. W., An Adaptation of Kubista's Method for Spectral Curve Deconvolution. *Anal. Chem.* **1997**, *69* (13), 2268-2274.

31. Genovese, D.; Rampazzo, E.; Bonacchi, S.; Montalti, M.; Zaccheroni, N.; Prodi, L., Energy transfer processes in dye-doped nanostructures yield cooperative and versatile fluorescent probes. *Nanoscale* **2014**, *6* (6), 3022-3036.

32. Rampazzo, E.; Bonacchi, S.; Genovese, D.; Juris, R.; Montalti, M.; Paterlini, V.; Zaccheroni, N.; Dumas-Verdes, C.; Clavier, G.; Méallet-Renault, R.; Prodi, L., Pluronic-Silica (PluS) Nanoparticles Doped with Multiple Dyes Featuring Complete Energy Transfer. *J. Phys. Chem. C* **2014**, *118* (17), 9261-9267.

33. Rampazzo, E.; Bonacchi, S.; Juris, R.; Montalti, M.; Genovese, D.; Zaccheroni, N.; Prodi, L.; Rambaldi, D. C.; Zattoni, A.; Reschiglian, P., Energy Transfer from Silica Core–Surfactant

Shell Nanoparticles to Hosted Molecular Fluorophores. *J. Phys. Chem. B.* **2010**, *114* (45), 14605-14613.

34. Bonacchi, S.; Genovese, D.; Juris, R.; Montalti, M.; Prodi, L.; Rampazzo, E.; Zaccheroni, N., Luminescent Silica Nanoparticles: Extending the Frontiers of Brightness. *Angew. Chem. Int. Ed.* **2011**, *50* (18), 4056-4066.

35. Zanarini, S.; Rampazzo, E.; Bonacchi, S.; Juris, R.; Marcaccio, M.; Montalti, M.; Paolucci, F.; Prodi, L., Iridium Doped Silica-PEG Nanoparticles: Enabling Electrochemiluminescence of Neutral Complexes in Aqueous Media. *J. Am. Chem. Soc.* **2009**, *131* (40), 14208-14209.

36. Yi, D.; Zhang, Q.; Liu, Y.; Song, J.; Tang, Y.; Caruso, F.; Wang, Y., Synthesis of Chemically Asymmetric Silica Nanobottles and Their Application for Cargo Loading and as Nanoreactors and Nanomotors. *Angew. Chem. Int. Ed.* **2016**, *55* (47), 14733-14737.

37. Zhao, Z.; Fu, J.; Dhakal, S.; Johnson-Buck, A.; Liu, M.; Zhang, T.; Woodbury, N. W.; Liu, Y.; Walter, N. G.; Yan, H., Nanocaged enzymes with enhanced catalytic activity and increased stability against protease digestion. *Nat. Commun.* **2016**, *7*, 10619.

CHAPTER 4

DRUG DELIVERY OF PluSNPs

4.1 DRUG DELIVERY NANOPARTICLES

The use of nano-based materials for sustained release of drugs presents advantages over the use of free drugs. These materials can improve the availability of molecules in the body and, when they are targeted, can increase the drug concentration in sites of interest, thus enabling the use of smaller doses^{1,2,3}. Moreover, nanostructured material can allow the formulation and design of multimodal agents combining therapeutic and diagnostic tools. These systems, referred as theranostic nanomaterials, can be developed for the investigation and treatment against invasive tumors. Tumor tissues, in general, show abnormal permeability for nanostructures because of their abnormal vascularization, so that large objects of suitable dimension are physically entrapped. This extravasation effect is called enhanced and permeability retention (EPR), can be considered as a form of passive targeting of nanostructured materials and offer a possibility to vehiculate nanocarriers selectively in tumor tissue.

The kinetics of entrapment can be modulated by controlling the surface properties (hydrophilicity, charge, functional groups) and the size of the nanoobjects.⁴ FDA has approved nanomaterials ranging from 10 to 130 nm based on EPR.⁵ For smaller objects the EPR shouldn't be effective while bigger ones can be bio-accumulated resulting toxic. Here, I proposed a nanoarchitecture based on dye doped silica which can be designed for drug delivery application combined in a unique structure with diagnostic features. This kind of luminescent silica core/Pluronic shell nanostructures are nowadays an interesting material because they are biocompatible, monodisperse, and the dyes which decorate the silica core yield tunable and size independent optical properties⁵. Recently, these dye doped nanoparticles are investigated in *in vivo* assays as a fluorescent agent, for diagnosis as a contrast agent for sentinel

lymph nodes and for therapeutic as photo-thermal agent^{6,7}. The synthesis of dye doped Pluronic Silica nanoparticle is made with a micellar assisted method where the Pluronic F-127 (F-127) micelle works as nanoconfined environment where the silica precursor can react and form a unique structure. At the end of the synthesis, the polymer is entrapped in a porous silica core with a whole diameter of 25 nm. The synthesis can be designed, using the micelle as a container for huge amount of lipophilic drug which can be partially entrapped by the silica core, with a final goal of controlling the kinetics of drug release respect to the system composed by Pluronic micelles. Polymer micelles have the potential to meet many of the requirements and have been extensively investigated for drug delivery, for gene delivery, and for carrying various contrast agents for diagnostic imaging. As a result, micelles can be used to effectively solubilize and carry in the core structure compounds that have poor solubility, low stability, or undesirable pharmaceutical properties. Micelles as drug carriers are inexpensive to make and are available in large quantities. Their small sizes also allow them to circulate in the body and accumulate in the affected area with leaky, pathological vasculature. The physical stability of the drug carrier is however a critical issue. For many applications it is desirable to have good stability and keep the pharmaceuticals and contrast agents in the blood pool over an extended period. Recent studies have shown that the *in vivo* antitumor activity of a drug incorporated into the polymer micelles is positively correlated with the stability of micelles. However, micelles may be intrinsically unstable in a natural, biological environment, even though some polymeric micelles are significantly better in terms of having a higher CMC and a more rigid structure. The micelle stability is particularly important for applications involving changes in temperature, solution concentrations, aggressive physical forces (mechanical shearing for example), or competing interactions in *in vivo* conditions. For example, Pluronic block copolymer micelles dissociate readily upon dilution. This could be a serious problem because when delivered

into body fluids, the surfactant concentration will be diluted by many orders of magnitude, possibly to below the CMC. Under these conditions, the micelles would disintegrate, and the drug would precipitate. The strategy of forming the PluSNPs by hindering the structure of the micelle within the formation of a silica core, can thus allow taking advantages of the micellar properties and overcome the instability limitations.⁸

The synthesis of Pluronic Silica nanoparticles is made by a micellar assisted method where the micelle, for drug delivery purposes works as a magazine. Pluronic F-127 micelles are widely investigated as carrier for lipophilic molecules.

In this context, Sorafenib Tosylate, a lipophilic drug for the human clinical treatment of renal carcinoma has been chosen as drug model (SRF, Figure 1).⁹

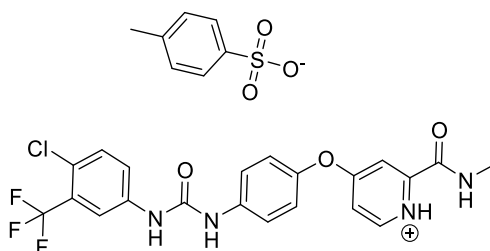


Figure 12. Chemical structure of Sorafenib Tosylate

This drug is very insoluble in water, since it precipitates at very low concentration (about 10^{-5} M). If Sorafenib (about 5 mg/ml) is solubilized in a F-127 micellar solution (F-127 5mM), the solution remains clear up to one hour and half; after that precipitation occurs. This behavior allows to design a suitable synthetic strategy for the formulation of fluorescent silica nanoparticles which can carry a large amount of drug and they are suitable, and can allow optical imaging.

4.2 Design of the Synthesis of dye doped PluSNPs

The transient Sorafenib entrapment in the Pluronic F-127 micelles offers the possibility to design the synthesis forming the silica core before the drug could diffuse massively in the bulk of solution where it precipitates. The synthesis of Pluronic silica nanoparticles is composed, in a typical synthesis by three principal steps:

- 1) The self-assembly of the micelles by Pluronic F-127. The kinetics of formation of micelles can take some minutes. The solution is kept under stirring until the solid is completely dissolved.
- 2) The hydrolysis in acidic media and condensation of the silica precursor in the nanoconfined reactor of the micelles: the most common silica precursor used is Tetraethylorthosilicate (TEOS) which is quite stable and, in these conditions, can react completely only after two-three hours. This reaction kinetics is too long for an efficient entrapment of the drug. Since alkoxy silane derivatives show a faster hydrolysis kinetics when the length of the alkyl chains is short, we choose for these purposes the smallest tetramethoxyorthosilicate (TMOS) which, in these conditions, can react completely in very few minutes.
- 3) The purification usually is carried out with a dialysis membrane. This purification method allows to neutralize the acidic medium and to eliminate the not reacted species. An efficient dialysis, however, takes at least one day, a too long period for this purpose since the drug can be released at least partially by the NPs. For this reason, we chose size exclusion chromatography (SEC, Sephadex® G-25); using PBS for the elution it was possible to neutralize the medium and remove the drug/dyes not entrapped in the nanoparticles.

4.3 Synthesis of SORAFENIB LOADED RHODAMINE B PLURONIC SILICA NANOPARTICLES.

molecule shows an extinction coefficient of $28500 \text{ cm}^{-1} \text{ M}^{-1}$. The same strategy is used for the computation of the Rhodamine as reported previously⁵. In the case of the SRF loaded NPs, the synthesis yields nanostructure with an average value of about 80-100 drug molecules loaded per nanoparticle and a dye doping degree lower than 1 dye per nanoparticles. The same dye doping degree is recorded for the control nanoparticles. This is due to the hydrolysis reaction of the dye triethoxy derivative which is too slow for this reaction resulting very inefficient. However, as a preliminary formulation, these nanoparticles show a very good loading property; for this reason, they can be considered a good compromise (in terms of drug loading) for the study of kinetics of release and for their biological investigation.

4.4 SORAFENIB RELEASE and NANOPARTICLE STABILITY

As already mentioned, the water solubility of Sorafenib is very low and precipitation occurs at very low concentration (10^{-5} M). Typically, when the molecules aggregate in solution the absorbance becomes decreases while scattering increases. When SRF is entrapped inside the nanoparticles, it shows an optical behavior very similar to the one solubilized in methanol. In this condition, the absorption spectrum is composed by a main band at 265 nm. The kinetics of the release is studied monitoring the decrease of absorbance at this wavelength. This method allows to monitor directly the release and can be more accurate than other assays, as dialysis or chromatography, where the process of separation can alter the kinetics^{10,11}.

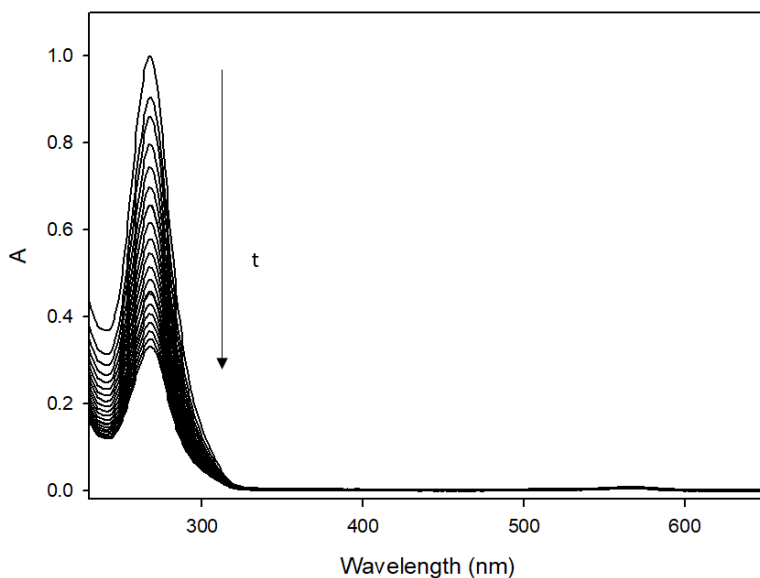


Figure 14. Absorbance of Sorafenib loaded Nanoparticles during the drug release.

The amount of drug released by diffusion from the silica core to the bulk of solution is obtained by the equation:

$$\% \text{Release} = \left[1 - \left(\frac{A_{265 \text{ nm}}(t)}{A_{265 \text{ nm}}(t=0)} \right) \right] * 100$$

The SRF entrapped in the nanoparticle diffuse spontaneously and it is released almost quantitatively in three days, a much larger time if compared with the micellar architecture where the drug is release in few hours at the same concentration (0.5 μM).

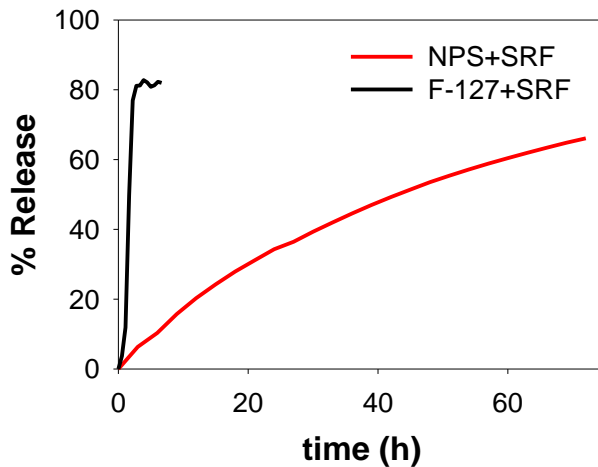


Figure 15. Trends of Sorafenib release % of Sorafenib Loaded Nanoparticles (red line) Pluronic F-127 Micelles (black line)

In order to verify the stability of the nanoparticles, DLS analysis is performed, following their hydrodynamic size during the drug release. The DLS distributions confirm, as expected, that the hydrodynamic size remains constant during the drug release at about 33 nm.

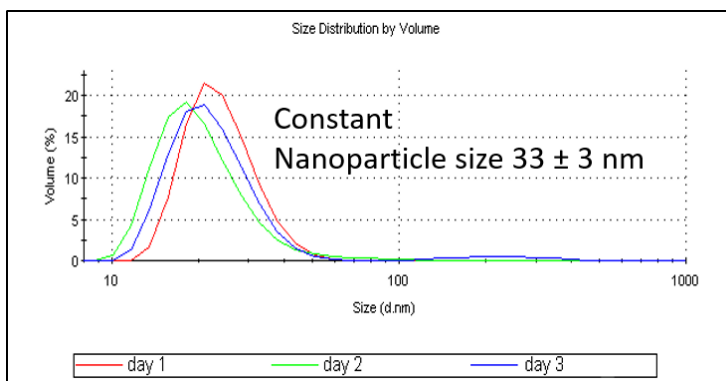


Figure 16. Dynamic light scattering distribution of Sorafenib Loaded Nanoparticles during the release

The profile of nanoparticle stability and the drug release features allows proceeding with biological investigation in order to check the *in vitro* effects of this nanocarrier on a tumor tissue.

4.5 PRELIMINAR IN VITRO TESTS

The biological investigations have been made in collaboration with Prof. Lucia Morbidelli of University of Siena.

Sorafenib is able to inhibit the cell proliferation and the tumor vascularization through inhibition of receptor tyrosine kinases (RTKs) inducing autophagy of the cells.

The main disadvantages related to the use of this drug are due to its short half-life (24-48h)¹² and toxicity¹³. Looking the mechanism of action of Sorafenib and its disadvantages, a SRF loaded nanostructure which can be entrapped inside a metastasis and is able to manage the drug release, can block the proliferation of the cancer cells and can inhibit in a more efficient way, respect to the free drug, the vascularization of the tumor mass, permitting to decrease the amount of drug used in the treatment and thus the side effects.

In order to prove the effects of this nanoarchitecture on the growth of metastasis the *in vitro* tests are focused to investigate the proliferation and migration of a model cell (HUVEC, Human umbilical vein endothelial cells). They are typically used as a laboratory model system for the study of the function and pathology of endothelial cells (e.g., angiogenesis). These assays are able to highlight the differences about the effect of free molecules SRF and SRF Silica nanoparticles on the control of the growth and the organization of HUVEC cells over time (24-48h). Sorafenib shows an EC₅₀ at concentration 5µM. The *in vitro* tests reported below are carried out setting the same concentration (5 µM) of drug for SRF and SRF-NPs. The control NPs are at the same concentration of the nanoparticles loaded with SRF.

4.6.1 Proliferation of endothelial HUVEC cells

The experiment is performed in medium containing 1 and 5 % of serum as growth factor. The number of cells is counted after 24 and 48 h of incubation. Firstly, the results show that cell proliferation in presence of NPs+Sorafenib is milder than the one observed with Sorafenib alone for both the serum concentration. This probably could be due to the slow release of the drug also in complex media. The nanoparticles without drug didn't affect the cell viability, meaning that these nanostructures, as already previously observed,⁶ exhibits a good biocompatibility.

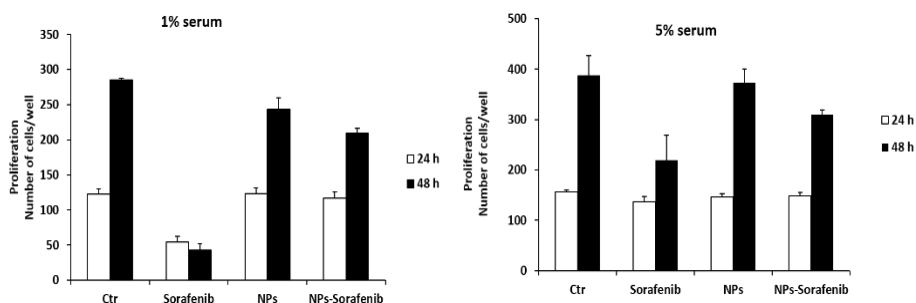


Figure 17. HUVEC cells viability over 24h and 48h after the incubation with SRF, SRF+NPs and NPs with different percentage of serum as growth factor

4.6.2 Morphology of HUVEC after 24 h

The results about the slow release of NPs+Sorafenib obtained by the proliferation assay are confirmed by looking the morphology of the cells after 24h from the incubation with the nanoparticle and the drug. Moreover, the cell morphology (and number) is altered in the presence of Sorafenib and NPs-Sorafenib: cells are elongated and spread while NPs without drug do not shows any cell deformation.

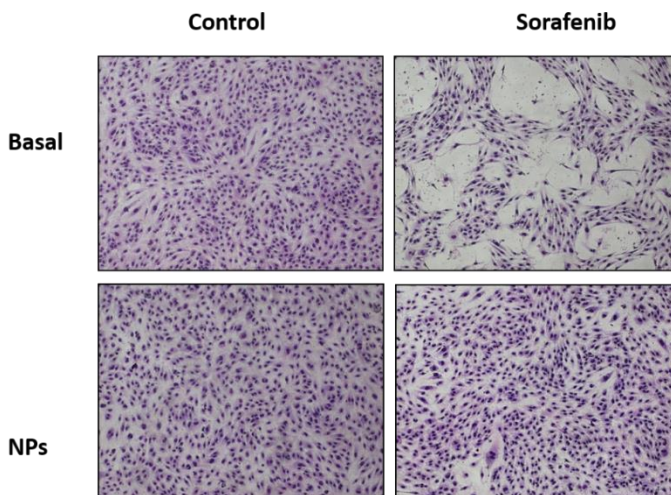


Figure 18. Morphology of HUVEC cells exposed with NPS, NPS+SRF, SRF, and control for 48h with 1% of serum as growth factor

4.6.3 Migration by scratch assay

The migration by scratch assay allows to measure cell migration *in vitro*. The basic steps involve creating a “scratch” in a cell monolayer, capturing the images close to the scratch, and comparing the images to quantify the migration rate of the cells. This analysis is suitable for studies on the effects of cell–matrix and cell–cell interactions, because it can mimic cell migration *in vivo* as wound-healing behavior. For this reason, the migration by scratch assay is commonly used for the evaluation of angiogenic control of endothelial cells. In this case, it is useful to highlight the effect of sorafenib and sorafenib nanoparticles in growing tissues processes. In this assay, empirically, confluent cells are scratched with a tip and then treated with nanoparticles and drug in presence of different amount of serum. After 18 h the area not covered by the cells is measured by image analysis. Data are reported as wound area^{14–16}.

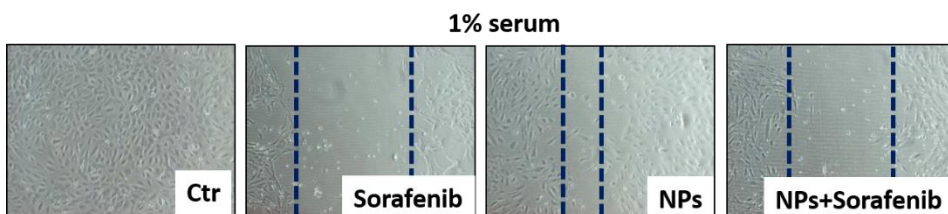
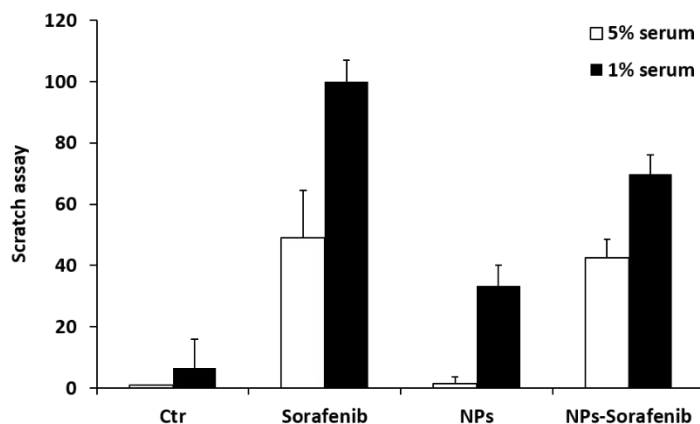


Figure 19. Migration scratch assay wound area of control, NPs, NPS+SRF and SRF incubated with 1% and 5% of serum as growth factor

For the NPs control a complete healing of the wound is observed, again confirming the biocompatibility of this nanoplatform. On the contrary, for Sorafenib and NPs+Sorafenib a large wound area is measured, highlighting that the NPs+Sorafenib can affect cell migration in a similar manner as the SRF alone. For these reasons the SRF loaded nanoparticles can be consider as a potential drug delivery system able to control the growth of cancer tissue.

4.6.4 Improvement for the *In vivo* Test

The aims of this study are the design of a theranostic nanostructure based on Sorafenib loaded Pluronic F-127 Silica nanoparticles. A theranostic platform should provide a diagnostic tool (optical imaging) and at the same time a therapeutic agent. In this case, the

three-days drug release showed by the nanoparticle is particularly suitable for an *in vivo* evaluation because it could match well with the kinetics of tumor entrapment by EPR and body-clearance (within 7 days) of the nanoparticles. However, the fluorescence features have to be improved increasing the dye doping degree for having an even higher sensitivity. Furthermore, the synthesis of this nanocarrier must be carried out immediately before the treatment because the drug is released spontaneously from the nanoparticle. To overcome these two problems, we modified the synthesis following these strategies:

- i) we derivatized the Rhodamine B with trimethoxy silane derivative, because of its faster hydrolysis, in order to increase the efficiency of the dye functionalization. In this way, we were able to include 4 Rhodamine B dyes per nanoparticle, a doping degree that is higher than the FDA approved Cornell Dots;¹⁸
- ii) we formulated by lyophilization a stable “ready to use” water dispersible solid powder keeping a similar drug loading.

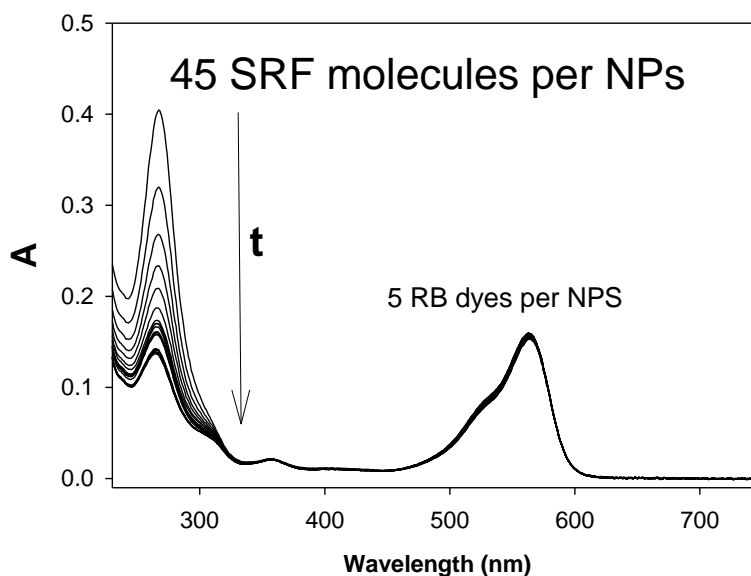


Figure 20. Absorbance of lyophilized SRF PluSNPs ($2 \times 10^{-7} M$) monitored for 12 hours.

These nanoparticles have showed promising preliminarily *in vitro* results. In particular, the extracellular signal-regulated kinase (ERK) is inhibited by Sorafenib only in presence of vascular endothelial growth factor (VEGF). Monitoring the expression of ERK HUVEC for the cells treated with VEGF is possible to evaluate the activity of the nanostructured drug carrier compared with the clinical drug.

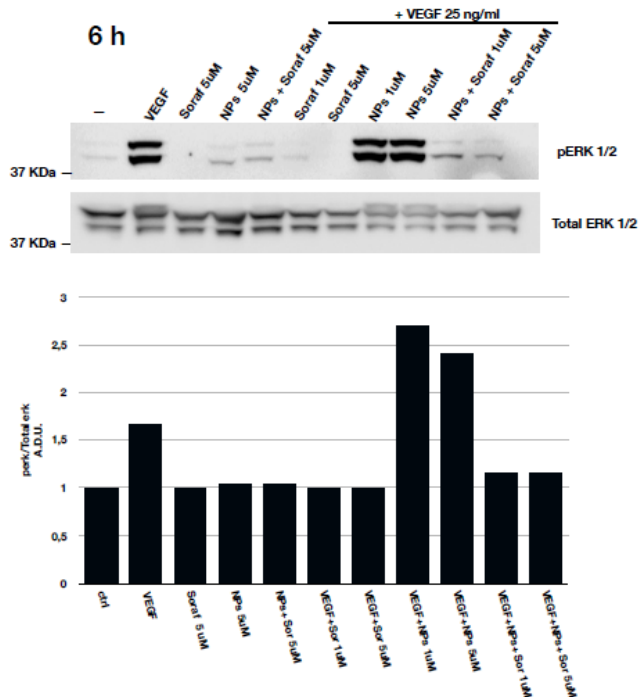


Figure 21. ERK expressed by HUVEC in presence and in absence of VEGFP. The cells have been incubated with SRF, NP_s+SRF and NP_s.

The expression of ERK in presence of VEGFP has revealed for the NP_s+SRF platform a similar effect in all the concentrations tested (Figure 9). This result showed with this assay could promote the evaluation of these engineered drug delivery systems for *in vivo* application.

4.7 CONCLUSION

Here I reported the design of core/shell Pluronic Silica Nanoparticles specifically as promising nanopatforms for drug delivery purposes. I engineered the synthesis of these nanoparticles in order to obtain a core entrapment of Sorafenib Tosylate - a lipophilic chemotherapy drug - which is used in clinical practice for malign renal and liver carcinoma treatment.

The drug release has been monitored looking at the decrease over three days of the absorption band of the drug localized about 260 nm. The nanoparticles are stable during the drug release, as confirmed by Dynamic Light Scattering analysis. The Sorafenib loaded Pluronic Silica Nanoparticles formulation has been then evaluated *in vitro* in different assays aimed to prove the slow release of the drug in biological environment and the effect of this drug delivery system as anti-angiogenic platform. The results obtained have been encouraging for extending the research to *in vivo* experiments, that are planned for the next future.

REFERENCES

- 1 Q. Qu, X. Ma and Y. Zhao, *Nanoscale*, 2015, **7**, 16677–16686.
- 2 S. Marrache and S. Dhar, *Proc. Natl. Acad. Sci.*, 2012, **109**, 16288–16293.
- 3 V. H. Shargh, H. Hondermarck and M. Liang, *Nanomedicine*, 2016, **11**, 63–79.
- 4 Y. Nakamura, A. Mochida, P. L. Choyke and H. Kobayashi, *Bioconjug. Chem.*, 2016, **27**, 2225–2238.
- 5 C.M. Dawidczyk et al. / *Journal of Controlled Release* 2014, **187**, 133–144
- 6 S. Biffi, L. Petrizza, E. Rampazzo, R. Voltan, M. Sgarzi, C. Garrovo, L. Prodi, L. Andolfi, C. Agnoletto, G. Zauli and P. Secchiero, *RSC Adv.*, 2014, **4**, 18278–18285.
- 7 S. Biffi, L. Petrizza, C. Garrovo, E. Rampazzo, L. Andolfi, P. Giustetto, I. Nikolov, G. Kurdi, M. B. Danailov, G. Zauli, P. Secchiero and L. Prodi, *Int. J. Nanomedicine*, 2016, **11**, 4865–4874.
- 8 M. Helle, E. Rampazzo, M. Monchanin, F. Marchal, F. Guillemin, S. Bonacchi, F. Salis, L. Prodi and L. Bezdetnaya, *ACS Nano*, 2013, **7**, 8645–8657.

- 9 Q. Huo, J. Liu, L. Q. Wang, Y. Jiang, T. N. Lambert and E. Fang, *J. Am. Chem. Soc.*, 2006, **128**, 6447–6453.
- 10 <https://www.cancer.gov/about-cancer/treatment/drugs/fda-sorafenib-tosylate>.
- 11 Y. Zambito, E. Pedreschi and G. Di Colo, *Int. J. Pharm.*, 2012, **434**, 28–34.
- 12 S. S. D'Souza and P. P. DeLuca, *Pharm. Res.*, 2006, **23**, 460–474.
- 13 <https://www.drugbank.ca/drugs/DB00398>.
- 14 <https://www.nexavar-us.com/possible-side-effects/?p=liver/>.
- 15 C. C. Liang, A. Y. Park and J. L. Guan, *Nat. Protoc.*, 2007, **2**, 329–333.
- 16 S. K. Nethi, S. Mukherjee, V. Veeriah, A. K. Barui, S. Chatterjee and C. R. Patra, *Chem. Commun.*, 2014, **50**, 14367–14370.
- 17 C. You, Q. Li, X. Wang, P. Wu, J. K. Ho, R. Jin, L. Zhang, H. Shao and C. Han, *Sci. Rep.*, 2017, **7**, 1–11.
- 18 Ulrich Wiesner et. al *J Clin Invest.* 2011;121(7):2768–2780.
doi:10.1172/JCI45600

CHAPTER 5

HYALURONIC ACID INTERACTION WITH PLURONIC SILICA NANOPARTICLES

5.1 INTRODUCTION

A very reliable and promising dye doped core/shell silica nanostructure, called PluSNP, was recently proposed by Prodi *et. al* as a bright luminescent nanoarchitecture suitable for bio imaging and drug delivery, with negligible *in vivo* and *in vitro* toxicity. PluSNPs are made of a silica core and biocompatible shell composed of Pluronic F-127, a PEGylated block co-polymer (Fig. 1). The PluSNP structure shows interesting features as a luminescent carrier for bio-sensing and as cellular marker^{1,2,3}. To develop and enhance the uptake properties of this kind of nanoparticles, colloidal self-assembly can be a very interesting and suitable strategy, yielding functional and dynamic nanoarchitectures.

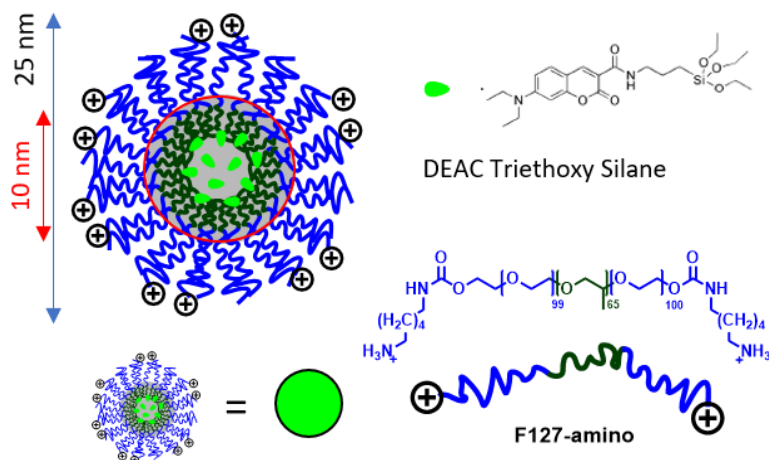


Figure 22. Illustration of DEAC doped Pluronic Silica Nanoparticles with a positive charged shell

Nanoparticle size, surface charge and composition are known to affect the uptake of nanoparticles by cells. Considering this, nanoparticle surface can be covered with biocompatible polymers, proteins, polysaccharides which are able to manage the cellular membrane trafficking^{4,5,6}. One of the most investigated structure able to control the nanoparticle surface and uptake properties is Hyaluronic acid (Hya, Fig. 2), a natural glycosaminoglycan widely distributed in the human body⁷.

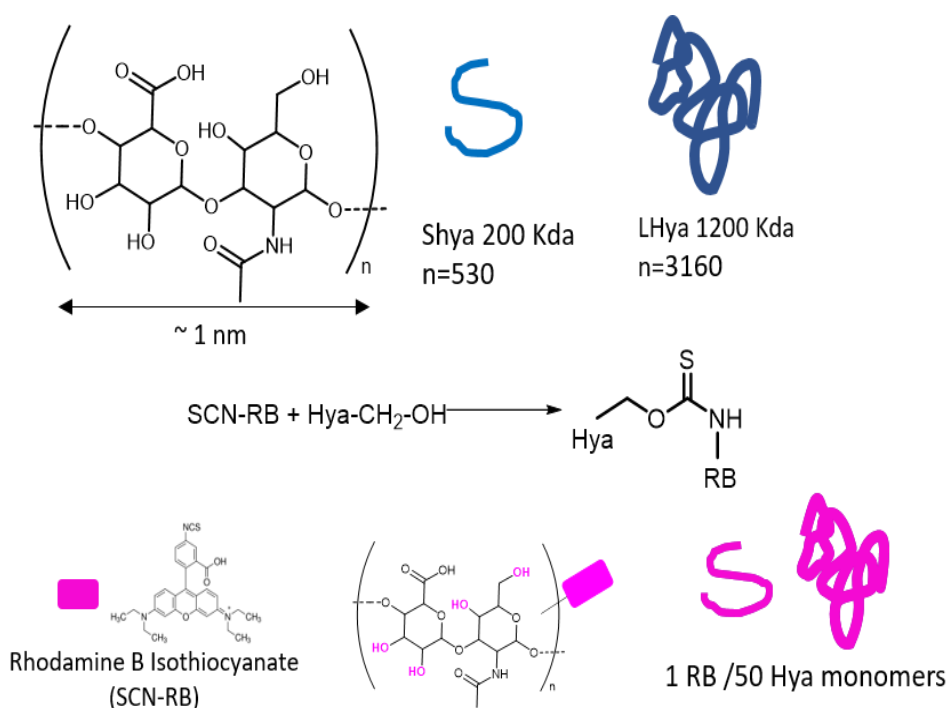


Figure 23. Illustration of hyaluronic acid: SHya 200 KDa and LHya 1200 KDa. Schematic representation of the reaction of RB isothiocyanate and Hya hydroxyl groups.

In physiological conditions Hya is negatively charged because of the deprotonation of the carboxylic groups that compose the structure of this polysaccharide. In addition, the polymer can interact with many water molecules via multiple hydrogen bonding: as a result,

hyaluronic acid is generally soluble in aqueous media. The biological, physical and chemical properties of this natural polymer can change drastically as a function of the molecular weight.⁸

This study is focused on the interaction of with PluSNPs with hyaluronic acid, labeled with fluorescent dyes, of two different molecular weight (200 and 1200 KDa).

Characterization of the interaction at the nanoscale has been carried out using: i) Forster Resonance Energy Transfer (FRET, that occurs in a nanoscale range, typically 1-10 nm) between dye doped PluSNPs (doped with a donor dye) and Rhodamine b labeled Hya (acting as acceptor in the FRET couple) and ii) the conformation-sensitive properties of the fluorescent hyaluronic acid, whose photophysical properties undergo significant changes when structural reorganization processes occur.

5.2 PROBING CONFORMATIONAL CHANGES OF HYALURONIC ACID

The Hya-Rhodamine B (Hya-RB) bioconjugate shows unique optical properties that depend on the folding conformation of the polymer chain. We exploited this behavior to probe the changes in the arrangements and reorganization of the hyaluronic acid when interacting with the environment and with other nano-objects. RB is a widely-used fluorophore for many applications, from bioimaging to lasing. This fluorophore, when well dispersed in a dilute condition displays remarkable optical properties such as very high brightness (extinction coefficient close to $100000 \text{ cm}^{-1} \text{ M}^{-1}$ and fluorescence quantum yields reaching 0.7 in ethanol) and a strong photo-stability. Moreover, the absorption and the emission spectra are localized in a spectral region suitable for bioimaging where phenomena of auto-bioluminescence are typically negligible. As other fluorescent

molecules, the optical properties are sensitive to the confinement when the local concentration of the dye is very high. Specifically, aggregation induces a decrease of the molar absorption coefficient of the band localized at 560 nm and strong quenching of the band.⁹ The chemical functionalization of hyaluronic acid with this fluorophore allows the investigation of the changes in the folding and polymer arrangements by monitoring the spectral properties of RB. The disaggregation of the polymer, increasing the distance among the dyes, promotes an increase of the brightness, because absorption spectra increase as well as fluorescence quantum yield.

The effect of addition of PluSNPs on the photophysical properties of Hya-RB is shown in figure 3. The absorption band of RB is slightly red shifted and the shoulder at 530 nm drastically decreases compared to the absorption peak (Figure 3A). In addition, the NP-Hya interaction induces an increase of the photoluminescence quantum yield (Figure 3B) of the RB by 250%.

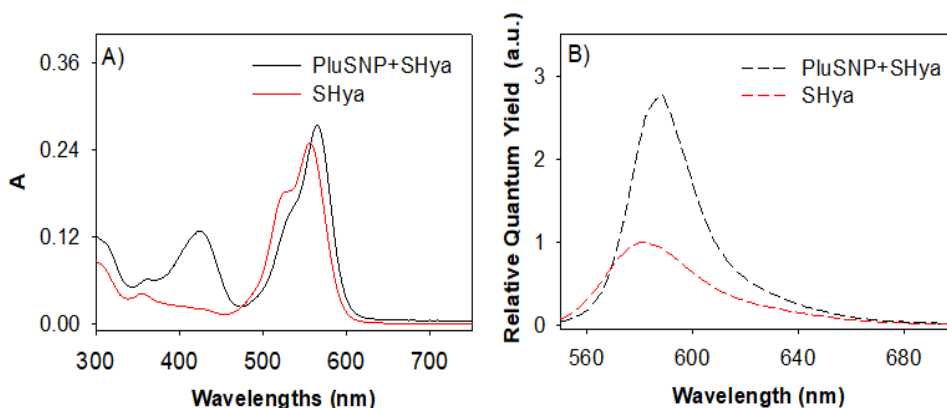


Figure 3. Spectral properties of Hyaluronic acid 0.5 μM in PBS pH 7.4. A) absorption spectra of PluSNP+SHya (black line) and SHya (red line). B) Relative Fluorescence Quantum yield of: PluSNP+SHya (black line) and SHya (red line). ($\lambda_{\text{exc}}=530 \text{ nm}$)

Given these peculiar photophysical changes, the unfolding process can be monitored via the following spectral parameters:

1. The value of the absorbance ratio at wavelengths (about 560 nm) $A_{\lambda_{\max}}/A_{530}$ nm, which provides an averaged information on the aggregation status of all rhodamine dyes in solution: the higher the $A_{\lambda_{\max}}/A_{530}$ ratio, the lower the aggregation of rhodamine dyes.
2. The value of the differential absorbance (A_i/A_{i-1} with i Hyaluronic acid concentration) ratio at wavelengths $A_{\lambda_{\max}}/A_{530}$ nm, which allows to focus on the last portion of hyaluronic acid added, or on its effect on the polymer already present in solution during the titration.
3. The increase of emission intensity at 580 nm, which is related to the decrease of rhodamine-self quenching.

Even though the effect of PluSNPs on the conformation of Hya-RB is clearly put in evidence, it is still unclear whether the “unfolded” Hya-RB remains in close contact with PluSNPs, or if it diffuses freely in solution, in the unfolded conformation, without further interacting with PluSNPs.

Thus, to probe not only the effect of the interaction between PluSNPs and Hya-RB, but also the persistence of the interaction and the distance at which it takes place, we designed a FRET couple between dyes embedded in the PluSNPs (diethylamino coumarin DEAC, donor dye) and dyes covalently linked to the polymer (RB, acceptor dyes). The large Forster Radius (3.83 nm), due do the high PLQY and ϵ of donor and acceptor, respectively, and to the good spectral overlap, allows to monitor the interactions between PluSNPs and Hya-RB, within 10 nm distance. It is indeed very important to note that energy transfer can occur only when donor and acceptor are very close (within roughly $2R_0$ distance). Bringing the spectral information of the RB status and its sensitization coupled to the quenching of DEAC due to energy transfer, the

polymer/nanoparticles interaction can be evaluated with nanoscale resolution.

FRET characterization is carried out by monitoring the fluorescence spectra obtained at two excitation wavelengths:

- 1) $\lambda_{\text{exc}} = 400 \text{ nm}$, where the absorption of DEAC is dominant, to check the quenching of the donor and the sensitized emission of the acceptor
- 2) $\lambda_{\text{exc}} = 530 \text{ nm}$, where only the rhodamine dye absorbs, to check the emission of the acceptor, when directly excited.

Experimentally, the interaction between SHya-RB (molecular weight 200 KDa) and DEAC-PluSNPs is evaluated recording the absorbance and emission spectra of a $0.2 \mu\text{M}$ solution of PluSNPs in PBS pH 7.4 and upon an addition of increasing amounts of the polymer solution. In addition, a control experiment is made starting from a solution without NPs to evaluate the dependence of SHya-RB conformation on its concentration. As shown before, the absorption spectra highlight notable differences in terms of absorption ratio at $\lambda_{\text{max}}/530 \text{ nm}$. For all the tested concentrations, the $A_{\lambda_{\text{max}}} / A_{530}$ ratio (Figure 4, C) shows the higher values in presence of PluSNPs.

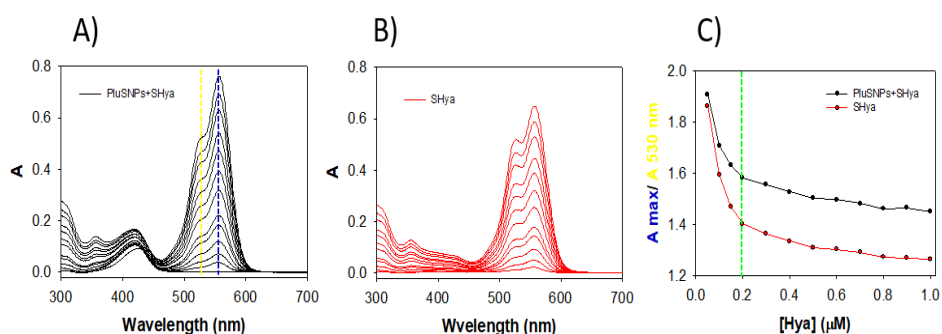


Figure 4. Absorption spectra of A) titration of PluSNPs $0.2 \cdot 10^{-6} \text{ M}$ with SHya (up to 5 eq.). B) Hya from 0 to $1 \cdot 10^{-6} \text{ M}$. C) Absorbance

ratio trends of RB $A_{\max}/530 \text{ nm}$ of PluSNPs and SHya (black) and SHya (red). $[PluSNP]/[SHya]=1$ green line

In order to check how each addition of hyaluronic acid affects the status of the rhodamine already present in solution, we computed the differential absorbance. This parameter allows to verify if the succeeding hyaluronic acid is able to modify the conformation of the polymer already in the system (in interaction with the nanomaterial and in the bulk of solution). As well as the absorption, the differential absorption ratio trends (Figure 5) indicate some differences when SHya interact with PluSNP respect the SHya alone. The decreasing trend of the absorbance ratio on the differential spectra of the SHya and nanoparticles system indicates that for each addition of hyaluronic acid a modification of the aggregation state of rhodamine occurs.

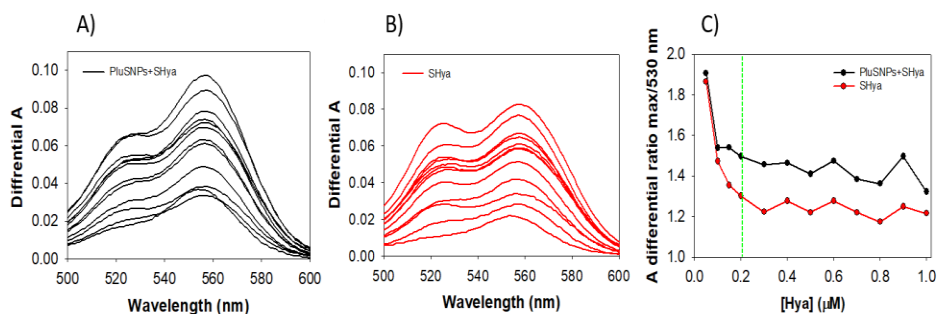


Figure 5. Differential Absorbance of: A) titration of PluSNPs $0.2 \times 10^{-6} \text{ M}$ with SHya (up to 5 eq.). B) Hya from 0 to $1 \times 10^{-6} \text{ M}$. C) Differential Absorbance ratio trends of RB $A_{\max}/530 \text{ nm}$ of PluSNPs and SHya (black) and SHya (red), $[PluSNP]/[SHya]=1$ green dashed line

The emission spectra confirm the information obtained by absorbance spectroscopy: Hya is interacting with PluSNPs at low concentrations, while at high concentrations it displays similar photophysical behaviours as in absence of PluSNPs. Indeed, RB displays high quantum yield associated with high $A_{\lambda_{\max}}/A_{530}$ ratios,

and low quantum yield associated with low $A_{\lambda_{\max}}/A_{530}$ ratios (figure 6).

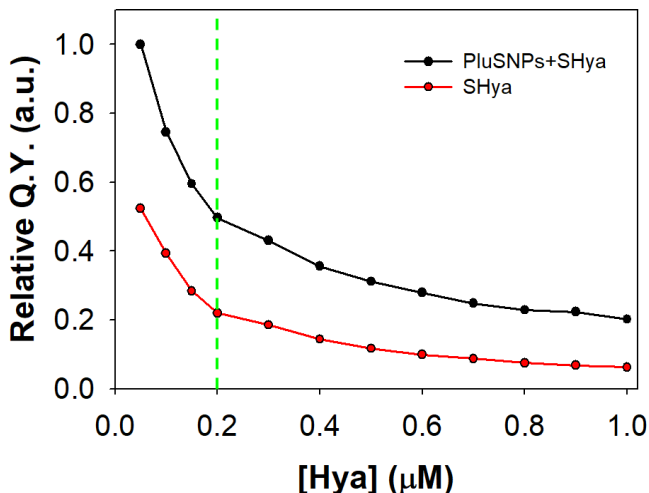


Figure 6. Rhodamine B Relative Quantum Yield of $2 \cdot 10^{-7} M$ PluSNP+SHya (black line) and SHya (red line). $[PluSNP]/[SHya]=1$ (green dashed line).

5.3 MODEL OF INTERACTION Hya 200 KDa (SHya) and PluSNPs

The trends of the absorbance ratio and of the quantum yield could be in agreement with two possible interaction mechanisms, based on either a “multilayer” or a “monolayer” process. In a multilayer process, many filaments can interact with a PluSNP forming several layers, where the additional layers not only have different properties, but can even change the properties of the first layer, while in a monolayer process the first layer passivates the surface which is thus not anymore available for interacting with other polymers, which thus remain in the bulk of the solution.

The information obtained by the absorbance spectra is not conclusive, since both models can justify the decrease of the peak/shoulder ratio observed in absorbance (figures 4 and 5). To select the most correct interaction model we carefully analyzed the information derived from the energy transfer between donor (DEAC dyes bound inside the core of the nanoparticle) and acceptor dyes (the RB linked to the polymer). Indeed, by combining the information gained exciting the donor (i.e., donor quenching and acceptor sensitized emission) and the information obtained by selectively exciting Hya-RB, it is possible to discriminate the amount and the properties of RB dyes in interaction with PluSNPs from the ones dispersed in the solution. Thus, we monitored the fluorescence properties of the sensitized RB (excited *via* DEAC with $\lambda_{exc} = 400$ nm) with those of directly excited RB dyes ($\lambda_{exc} = 530$ nm, yielding an average information of all rhodamine dyes present in solution). The emission intensity trend of the RB (Figure 7) increase as function of SHya concentration and after an inflection point at 0,75-1 polymer equivalents per nanoparticle seems to increase slightly, which is in line with the absorption trends. In presence of PluSNPs, the RB from the very first addition is more emissive than the system alone.

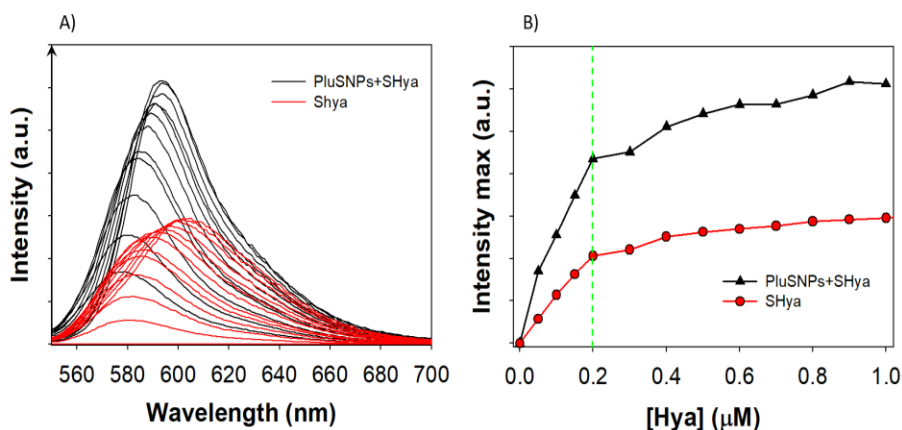


Figure 7. A) Emission spectra of solutions obtained upon addition of increasing amounts of Hya up to 1×10^{-6} M to a buffered 2×10^{-7} M

solution of PluSNPs with SHya (black line) and to a buffered solution only (red line). B) Emission Intensity trends of RB at 580 nm of PluSNPs and SHya (black) and SHya (red), $[PluSNP]/[SHya]=1$ (green dashed line). ($\lambda_{ex}=530$ nm)

For the description of the energy transfer process it is necessary to report the emission quenching of the donor (DEAC of PluSNPs) as a function of the concentration of the acceptor (Rhodamine B of Hya). The DEAC emission decrease for all the concentrations of Hya up to 80% of the initial intensity (Figure 8).

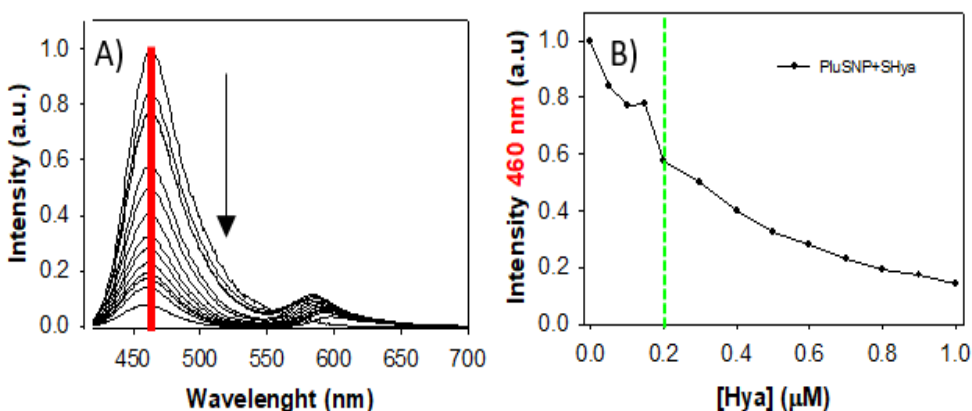


Figure 8. A) emission spectra of the titration of DEAC PluSNPs with SHya B) Emission Intensity trend of DEAC emission at 470 nm. ($\lambda_{ex}=400$ nm). $[SHya]/[Hya]=1$ (green line)

The clear indication of the model that describes the interaction is found on the sensitization of the acceptor. In agreement with the theory, a FRET sensitization derives from the product of the quenching of the donor and the quantum yields of the acceptor. From a theoretical view point the two models should show different sensitized emission trends. In the case of multilayer interaction, all RB dyes (Q.Y. decreasing with $[Hya]$) are sensitized, and the resulted trend features a maximum point (Figure 9, A); if self-

quenching occurs between the dyes of the different layers, a decrease of the luminescence is expected afterwards. In the case of monolayer interaction, sensitization involves only the dyes of the monolayer, that are the brightest because they are not self-quenched (QY approx. constant). A plateau is expected afterwards, because the Hya in excess would be not interact with the NPs, and thus not involved in the energy transfer process (Figure 9, B).

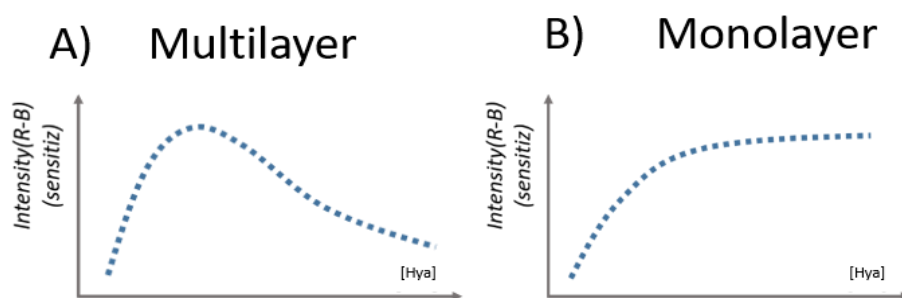


Figure 9. Schematic illustration of theoretical sensitized emission of A) Multilayer and B) Monolayer

The sensitized emission (Figure 10A) yields the information of only those RB dyes that are in interaction with the PluSNPs. The experimental sensitized emission, as well as the computed sensitized emission (which thus represents the sensitized emission of all RB dye in solution, calculated as the product of the average Q.Y. and the quenching ratio, Figure 10B), both suggest that the most correct interaction model is the “multilayer” one. In conclusion, the interaction of SHya and PluSNPs can be modeled as a multilayer process where the nanoparticles are surrounded by numerous layers of polymer, where the absorption of each layer induces reorganization and photophysical changes in the bottom layers. The experimental points follow in fact the same trend depicted in figure 9A.

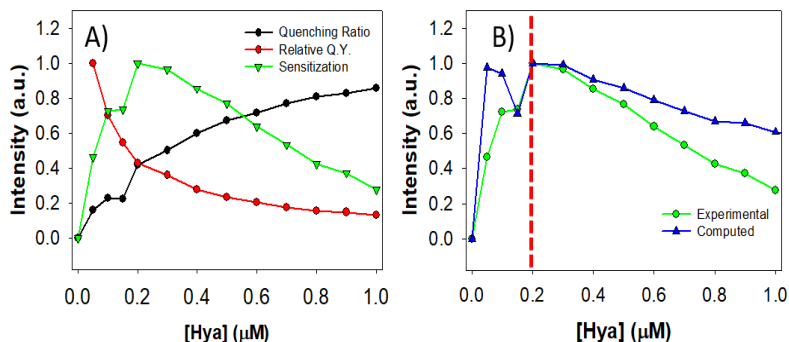


Figure 10. A) RB sensitized emission (green line) computed by the product of the DEAC quenching ratio computed as $1 - I/I_0$ (black line) and the SHya fluorescence quantum yield (red line). B) Comparison between the computed RB sensitized emission (green line) and the experimental one (blue line). $[SHya]/[PluSNP]=1$ (red dashed line).

5.4 HYALURONIC ACID 200 KDA (SHya) – MEDIA EFFECT

The multilayer model can describe the interaction between Hya and NPs in PBS at pH 7.4 a very high ionic strength condition, a pH at which the poly-anion can be considered fully deprotonated. As other polyelectrolytes, Hya can change its conformation as a function of the dispersion media. In order to verify the effects of different aqueous media on the polymer conformation, the same experiment has been carried out in deionized water, phosphate buffer saline pH 5.5 and phosphate buffer 7.4. The analysis of the absorbance ratios (Figure 11) shows that in all the media tested the fluorescence trend is different, confirming that the ionic strength and the pH play an important role.

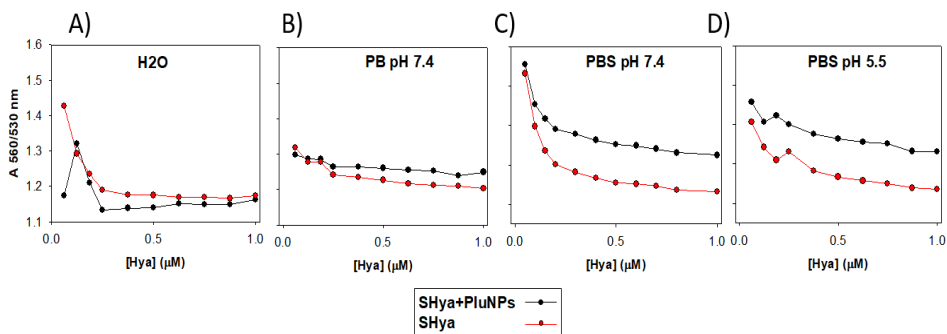


Figure 11. Absorbance ratio 560 /530 nm of SHya and PluSNPs in different media: A) Deionized water, B) Phosphate Buffer pH 7.4, C) Phosphate Buffer Saline pH 7.4 and D) Phosphate Buffer Saline pH 5.5.

The trends (Figure 12) of quenching ratio of DEAC and the RB relative quantum yields, and the computed and experimental sensitized emissions, highlight that the interaction in all the media tested can be described by a multilayer model.

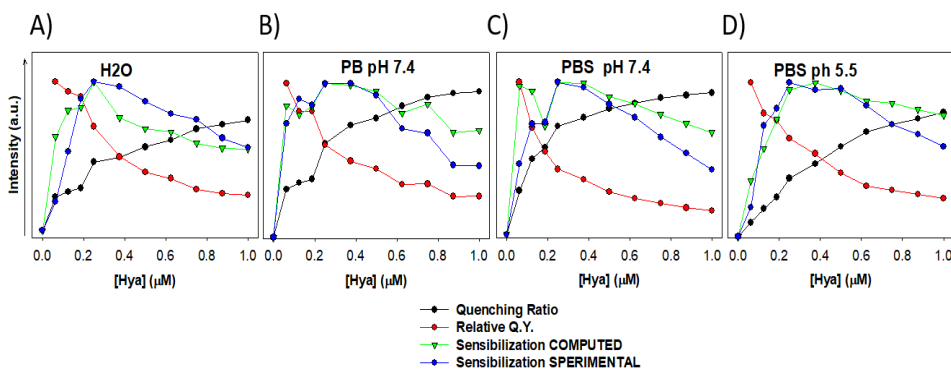


Figure 12. Emission, quenching and computed/sperimental sensitization of PluSNP+SHya in different media A) deionized water, B) Phosphate buffer pH 7.4, C) Phosphate buffer saline pH 7.4 and D) Phosphate buffer saline pH 5.5

5.5 Hyaluronic acid 1200 KDa (LHya)

The polymer properties in general can change drastically with the molecular weight. Moreover, in recent biological investigations, length of the Hya chain is indicated as a key factor that can influence the pathological regulation of a metastasis⁷. For these reasons is necessary to expand the characterization of the interaction between PluSNP and Hya to another molecular weight. We have functionalized a 1200 KDa Hya (LHya) as SHya obtaining a similar dye doping degree. Firstly, that polymer has been investigated in PBS pH 7.4 and water, to observe on the LHya the media effect (Figure 13). Also in this case the two trends were different, suggesting, as expected, that also for this heavier polymer the media can change the reorganization.

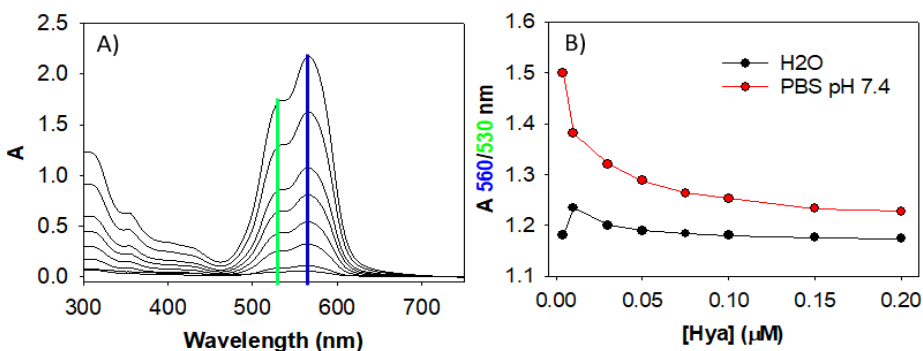


Figure 13. A) Absorption spectrum of LHya in PBS increasing the concentration. B) Absorption ratio 560/530 nm of LHya in water and PBS pH 7.4

Like SHya, LHya presents differences on the trend of absorbance ratio in presence of PluSNP. Also in this case, PluSNP increase the value of the absorbance ratio, indicating that interaction provokes changes on the polymer reorganization. The trend has an inflection point at about 2-3 PluSNPs per filament (Figure 14) while the trend of SHya, described previously, is centered at about 1 PluSNP per polymer.

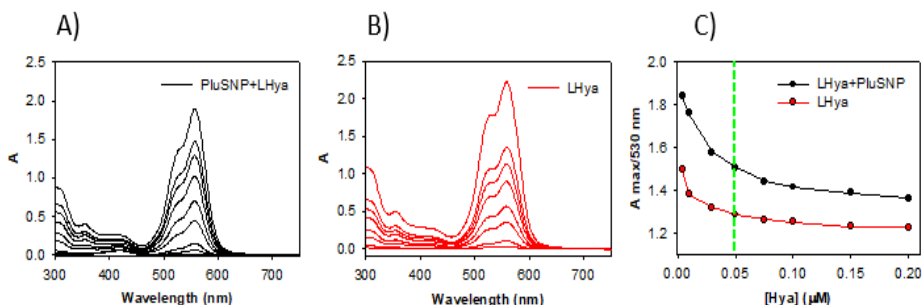


Figure 14. A) Absorbance LHyA+PluSNP $0.1 \cdot 10^{-7}$ M (black), B) and LHyA (red) and C) absorbance ratio in PBS pH 7.4. $[PluSNP]/[LHyA]=2.0$ (green dashed line)

As in the case of the lighter polymer, we performed experiments to quantify the efficiency of the energy transfer between NPs and LHyA in PBS pH 7.4. Fixing the concentration of the NPs ($0,1 \mu\text{M}$) and by several additions of LHyA, the emission properties of the donor and the acceptor have been recorded. The trends of the quenching of the DEAC and of the sensitized emission signals confirm that the interaction of the LHyA and PluSNPs occurs with a different ratio respect to the one observed SHyA: again the inflection point has been observed at 2-3 PluSNPs per filament.

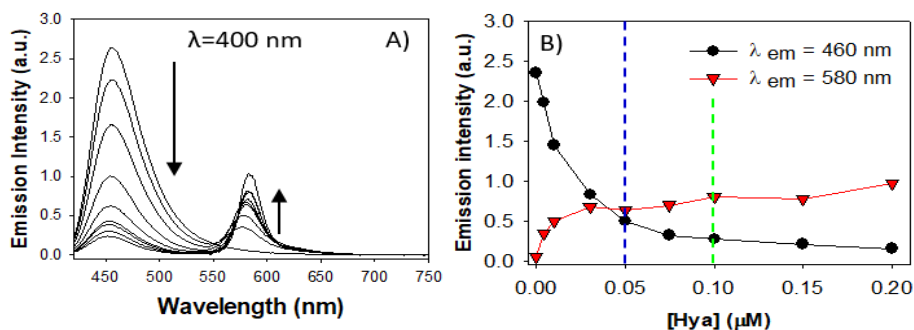


Figure 15. A) Emission Spectra of DEAC of PluSNP $1 \cdot 10^{-7}$ M in presence of different amount of LHyA (up to 5 eq.) B) Emission trend of DEAC at 455 nm (black line) and of RB at 580 nm (red line).

$[PluSNPs]/[LHya]=1$ (green dashed line), $[PluSNPs]/[LHya]=2$ (blue dashed line) ($\lambda_{ex}=400$ nm).

This conclusion is confirmed by the direct excitation of RB which is in line with the sensitized emission.

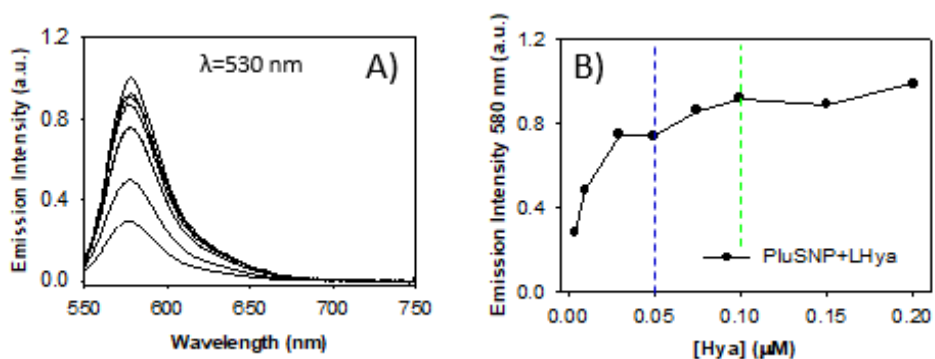


Figure 16. A) Emission Spectra of RB in different amount of LHya in presence of PluSNP $1 \cdot 10^{-7}$ M. B) Emission trend of RB at 580 nm. $[PluSNPs]/[LHya]=1$ (green dashed line), $[PluSNPs]/[LHya]=2$ (blue dashed line) ($\lambda_{ex}=530$ nm).

5.6 Interaction Mechanism comparison of LHya and SHya.

To highlight differences on these interactions between PluSNPs and Hya (SHya and LHya), a titration fixing the concentration, in term of monomer units, of hyaluronic acid and adding several amounts of nanoparticles has been carried out. In particular, the concentration of the polymer was 100 μ M for SHya and 16,6 for μ M LHya. RB absorbance ratio (Figure 17, E) shows an increase after each addition of the solution of PluSNPs. The absorbance ratio trends for these different polymers give an indication about the ratio of the interaction which provoke a drastic change on the polymer reorganization. The inflection points are localized at 6 PluSNPs per filament in the case of LHya and 1 PluSNP per filaments for SHya.

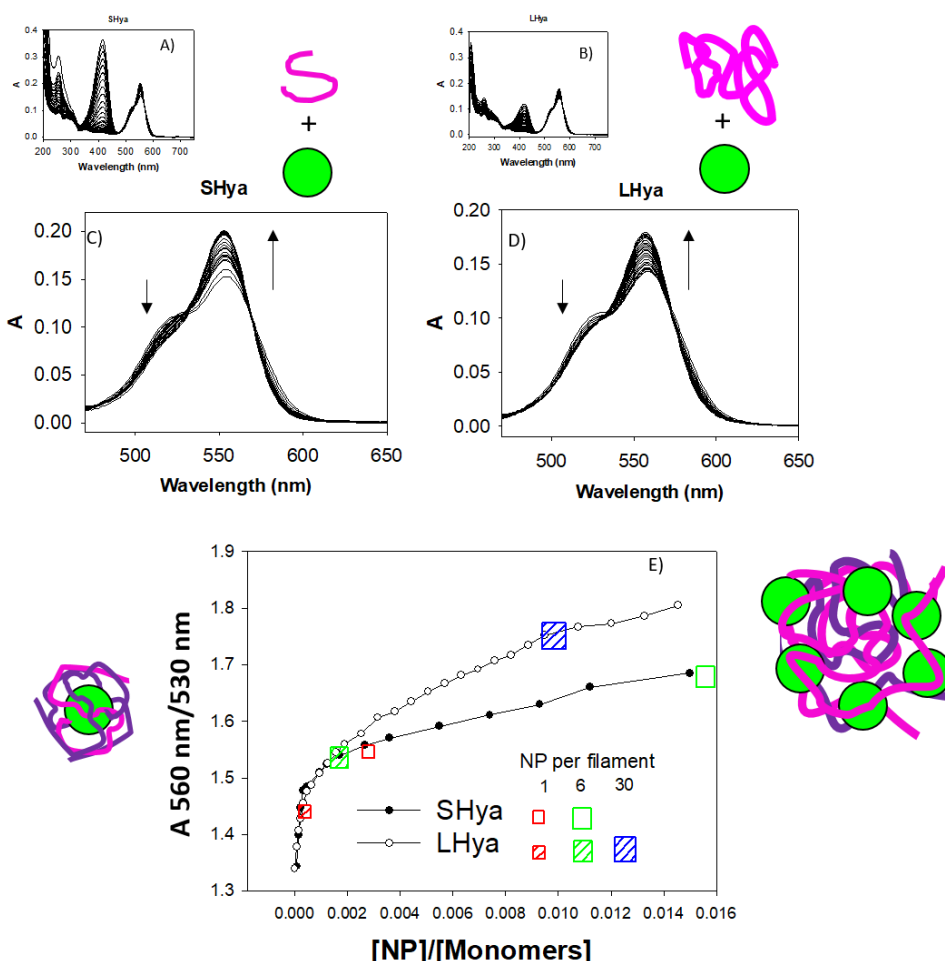


Figure 17. A) Absorption spectra of the titration of SHya and B) LHya with increasing amounts of PluSNPs in PBS pH 7.4. C-D) Detail of RB absorption spectra of the titration of SHya and LHya, respectively. E) Trend of the absorption ratio 560 nm/530 nm SHya (black dots) LHya (white dots).

The emission properties of the system, as the quenching ratio ($1 - I/I_0$, I = emission intensity of donor in presence of acceptor, I_0 = emission of the donor in absence of the acceptor) and the sensitized emission, can confirm the same ratios where the polymer change drastically its conformation. (Figure 18, C; Figure 19).

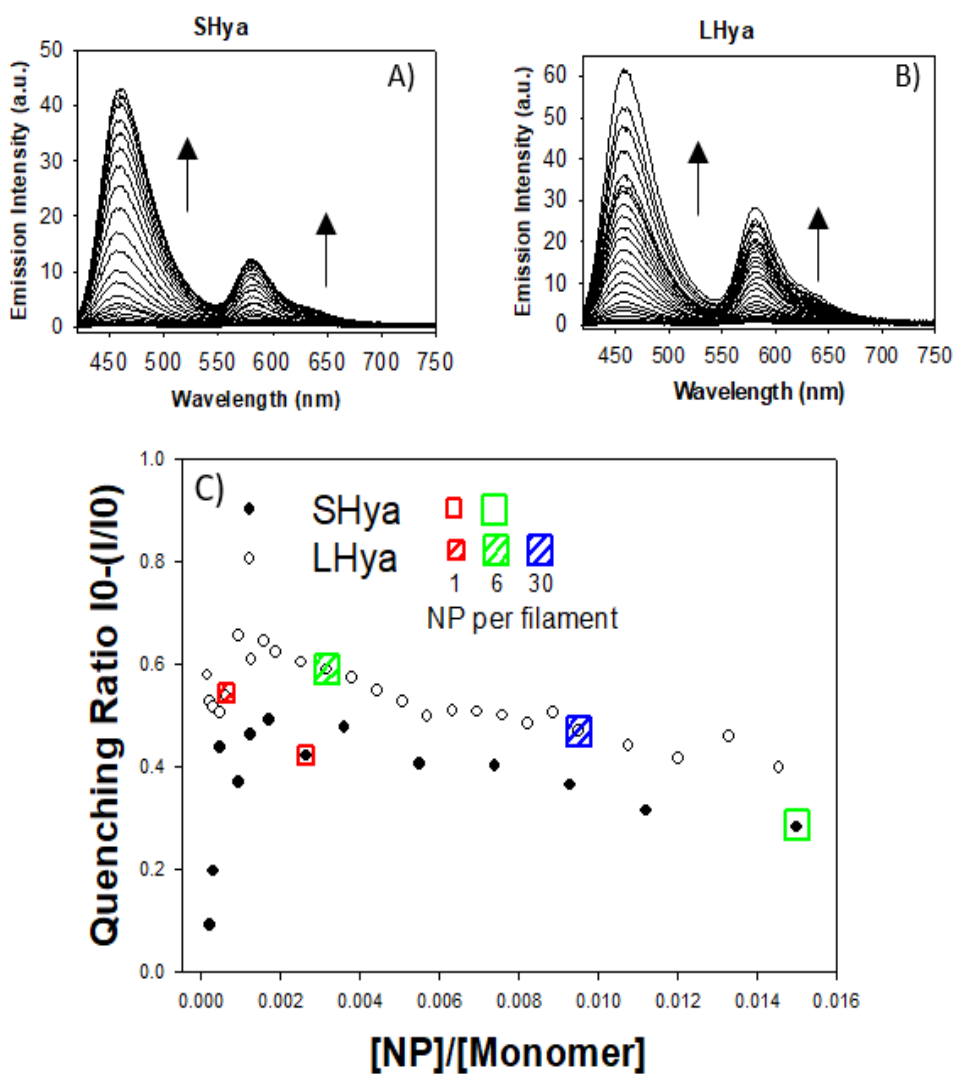


Figure 18. A-B) Emission spectra of SHya and LHya, respectively, upon addition of PluSNPs ($\lambda_{exc} = 400$ nm). C) the quenching ratio of the donor.

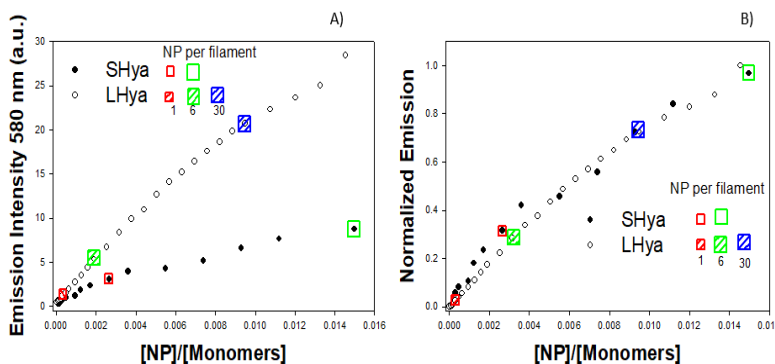


Figure 19. Sensitized emission and normalized sensitized emission

The direct excitation of the RB confirms, for the two polymers, the same results in terms of differences of PluSNPs/Hya ratios (Figure 20). In general, the interaction is driven by the ratio NP/Hya monomers concentrations meaning that LHya is able to interact with more nanoparticles than SHya. The results obtained suggest that a single chain of LHya is able, as expected, to wrap a higher number of NPs respect to SHya.

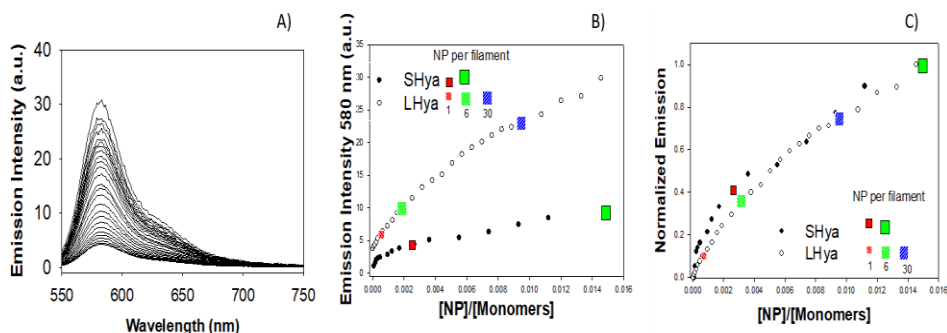


Figure 20. A) Spectra of the RB emission enhancement due to the PluSNP additions B-C) Trends of the emission intensity and the normalized emission of the titration for SHya (black dot) and LHya (white dot). ($\lambda_{ex}=530$ nm).

It is interesting to underline that the normalized trends are all very similar; probably, they can exclude differences on the nature of the interaction.

5.7 HYDRODYNAMIC SIZE DISTRIBUTION

To confirm the size difference of the PluSNPs and SHya/LHya aggregates the investigation of the hydrodynamic diameter measured by Dynamic Light scattering has been carried out. The dynamic light scattering (DLS) is a technique that can be used to determine the hydrodynamic diameter and its distribution of particles dispersed in a fluid.

In this system the analysis indicates which is the behavior of the hydrodynamic size of the hyaluronic acid and averagely the dimension of the aggregates in presence of nanoparticles. In general, the hydrodynamic diameter of Hya alone is very large and Hya in solution should compose very big aggregates. Averagely DLS reveals that (Figure 21) the aggregates between PluSNP and Hya are bigger than nanoparticle alone but smaller than the aggregates formed by Hya alone.

In general, DLS analysis cannot provide information about the behavior of the single component in solution; while additional information on the dynamic of Hya can be obtained using fluorescence correlation spectroscopy (FCS). This technique permits the selective observation of the diffusion of a fluorophore by a suitable excitation.

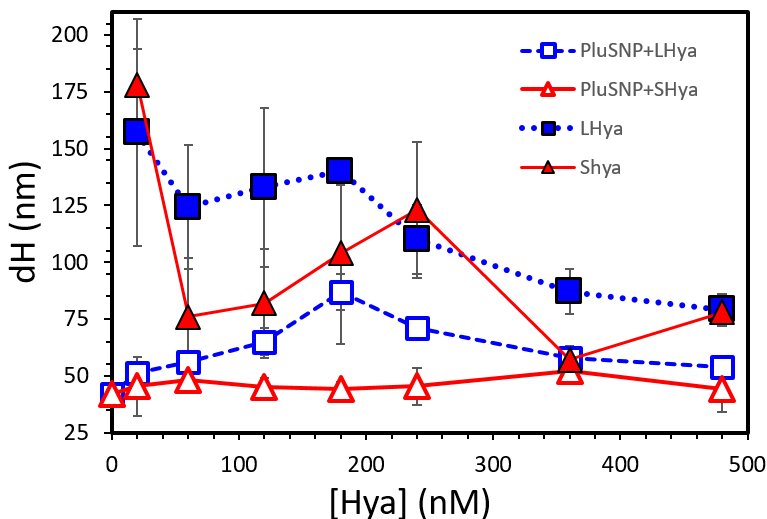


Figure 21. Hydrodynamic diameter of PluSNP $1 \cdot 10^{-7}$ M with different concentration SHya (red empty triangle) and LHya (Blu empty square) and SHya (red filled triangle), LHya (blue filled square) alone. (PBS pH 7.4).

5.8 Fluorescence Correlation Spectroscopy on Hya/PluSNPs ensemble

Fluorescence correlation spectroscopy (FCS) is an experimental technique using statistical analysis of the fluctuations of fluorescence in a system in order to observe dynamic molecular events, such as diffusion or conformational fluctuations of biomolecules. The diffusion of an object in solution is related to its hydrodynamic size. The FCS is a very powerful tool because permit the selective excitation of the dye of interest. In this case, it was possible to highlight the faith of the RB bound to the polymer and following with very high resolution what happened to the polymer when interacting with the nanoparticles (at very low concentration as well). Averagely, the Hyaluronic acid in solution forms very big aggregates (Fig 22). In particular, LHya forms bigger objects than SHya. The addition of PluSNPs brakes the matrix formed by the

polymer aggregates composing of ensembles which diffuse slower than the PluSNPs alone. SHya aggregates show a diffusion very similar to the nanoparticles alone and in interaction at low concentration. However, the breaking effect of the Hya matrix provoked by the nanoparticles is visible at the highest concentration (Figure 22, B). The FCS results are useful to imagine what happened during this interaction: the polymer composes aggregates where the rhodamine dyes are quenched, then the nanoparticle disrupts the aggregates provoking a decrease of the rhodamine self-quenching and a decrease of the size.

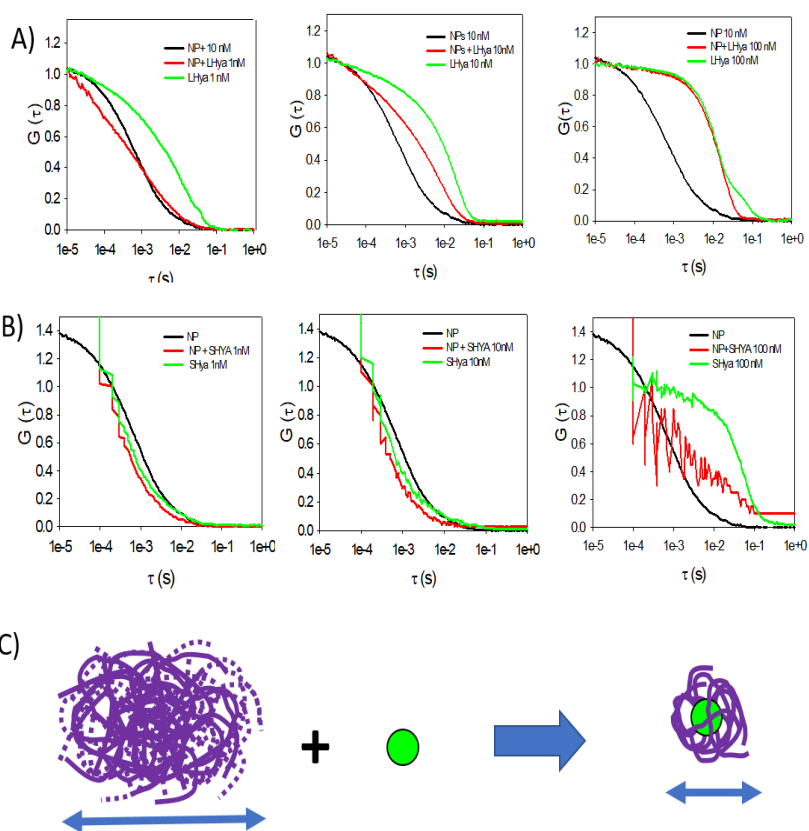


Figure 22. Plot of the correlation of Hya and PluSNPs and PluSNP+SHya at three different concentration respectively 1, 10,

100 nM of A) LHya and B) SHya. C) schematic representation of the Hya aggregates disruption provoked by the PluSNPs.

5.9 PRELIMINAR *IN VITRO* TEST

To investigate the effect of hyaluronic acid on the cellular uptake of PluSNPs, a preliminary *in vitro* test has been carried out using HeLa cells as a tumor cell line model. Moreover, the characterization has been carried out with a confocal microscope checking the emission intensity of Rhodamine B modified Pluronic silica nanoparticles (very bright). In this case we used a not labeled hyaluronic acid assuming that it could have the same effect on the cell interaction as the fluorescent one. The experiments are made incubating the cells for 3 hours with PluSNPs $1 \cdot 10^{-7}$ M and SHya $1 \cdot 10^{-7}$ M or LHya $1.6 \cdot 10^{-8}$ M ($[PluSNP]/[SHya]=1$, or $([PluSNP]/[LHya]=6)$) to observe if there were a different nanoparticle internalization upon changing the size of the polymer. As it can be observed in figure 23, the intensity ratio of the aggregates of PluSNP and Hya are internalized more efficiently than the nanoparticles alone. Moreover, the nanoarchitecture composed by LHya and nanoparticles shows the best uptake level (100% more than PluSNPs). This increase in the internalization kinetic, if confirmed also with other cell lines and in *in vivo* experiments, could suggest an interesting strategy to increase the theranostic abilities of the PluSNPs.

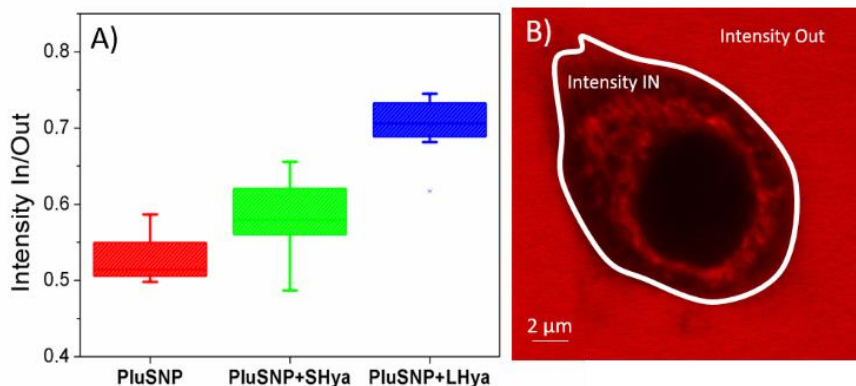


Figure 23. A) BOX plot of Intensity inside/outside the cell ratio of PluSNP 1×10^{-7} M (red box), PluSNP+SHya ($[PluSNP]/[SHya]=1$) (green box) and PluSNP+LHya ($[PluSNP]/[LHya]=6$) (blue box). B) example of HeLa cell incubated with PluSNPs.

5.10 CONCLUSION

Here I reported an extensive investigation of the interaction between core shell nanoparticles PluSNPs and a biocompatible polysaccharide, namely RB-derivatized Hyaluronic acid (Hya). This fluorescent biopolymer reveals a very promising property, since the changes of Hya conformation can be monitored following both the absorption and in emission spectra of RB. The information obtained by the changes in the photophysical properties of RB can also be suitably combined with the information obtained evaluating the energy transfer efficiencies between donor dyes embedded in PluSNPs (DEAC) and RB-Hya as acceptor. The FRET investigations allow the understanding at the nanoscale of the mechanism of interaction, indicating that a nanoparticle is surrounded by many Hya filaments yielding a multilayer structure. The effect of the molecular weight of Hya on the assembly has also been investigated. In this context, energy transfer is useful to determine the steps of this interaction. We observed similar

photophysical properties for RB when SHya interacts with 1 PluSNP, or when LHya (6 times longer polymer) interacts with 6 PluSNPs.

The hydrodynamic radius of Hya in bulk solution and in interaction with PluS NPs are evaluated with two different correlation techniques, namely DLS and FCS. The two techniques allow to confirm the hypothesis made evaluating the photophysical data, highlighting moreover the aggregated nature of Hya in solution which is disrupted in presence of the nanoparticles.

Finally, the different aggregates are evaluated in cellular tests where HeLa cells are incubated with PluSNP and SHya (1:1) and LHya (6:1) fixing the concentration of nanoparticle at $1 \cdot 10^{-7}$ M. The biological assay indicates that PluSNPs uptake is largely enhanced in presence of LHya, a very interesting and promising result for increasing the theranostic abilities of the PluSNPs.

5.11 TECHNICAL NOTES

MATERIALS AND METHODS

Following compounds are purchased by Sigma: Rhodamine B isothiocyanate mixed isomers (98%), 7-(Diethylamino) coumarin-3-carboxylic acid (98%, DEAC), Rhodamine B mixed isomers (98%, RB), Pluronic F127, Sodium Chloride (98%), glacial acetic acid (...), dialysis membrane 12 MWCO, N,N'- disuccinimidyl carbonate (94%), 4-(Dimethylamino)pyridine (DMAP, 99%). (3-Aminopropyl)triethoxysilane (99%, APTES), Tetraethyl Orthosilicate (98%, TEOS), 1,6Diaminohexane (98%), chlorotrimethylsilane (98%, TMSCL) Solvents used: dry tetrahydrofuran (dry, THF), acetone (technical grade), MilliQ water (18.2 μ S), Dichloromethane (technical grade). Phosphate buffer saline pH 7.4 and the other buffer are made dissolving the opportune amount of monohydrogen disodium phosphate and sodium phosphate setting the right pH with small amount of NaOH/HCl with a pH-meter. For the ionic strength

control are used sodium chloride (NaCl) and potassium chloride (KCl).

RHODAMINE B LABELED HYALURONIC ACID SYNTHESIS

Hyaluronic acid (200 KDa SHya and 1200 KDa LHya) is labeled with Rhodamine B isocyanate fixing the monomer/fluorophore molar ratio of 7 equivalents. A 50 mg di solid hyaluronic acid (200, 1200 KDa) are dispersed in 12 ml DMSO and the right amount of Rhodamine B dye (3 mg for 200 KDa and 18 mg for 1200 KDa) are dissolved and the reaction is carried out overnight. After that the reaction is diluted with 24 ml of d.i. water and the solutions are dialyzed against water (cut off membrane 12 MWCO) until the water is resulted colorless. the doping degree is checked by a UVvis spectroscopy and is the same for both polymer lengths about 1 fluorophore every 50 monomers. The average fluorescence quantum yield range for the SHya from $2.5 \cdot 10^{-3}$ to $2.5 \cdot 10^{-2}$ and for LHya $2.7 \cdot 10^{-3}$ to 0.11. the quantum yields are measured using the Rhodamine B in ethanol as a reference with Q.Y.=0.96.

TRIETHOXYSILANE DERIVATIVE OF COUMARIN-DEAC

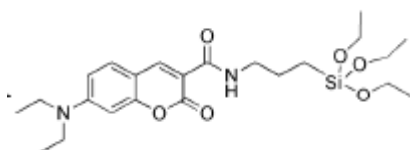


Figure 24. DEAC coumarin triethoxysilane derivative

DEAC: 7-(diethylamino)-N-(3-(triethoxysilyl)propyl)-2oxo-2-H-chromene-3-carboxamide (7-(diethylamino)-N-(3-(triethoxysilyl)propyl)Coumarin-3-carboxamide)

DEAC derivative has been synthesized using reported procedures¹⁰

TRIETHOXSILANE DERIVATIVE RHODAMINE B SYNTHESIS

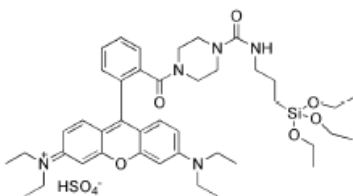


Figure 25. rhodamine B triethoxysilane derivative

The rhodamine B derivative has been synthesized using reported procedures¹¹.

AMINO DERIVATIZED PLURONIC F-127 SYNTHESIS

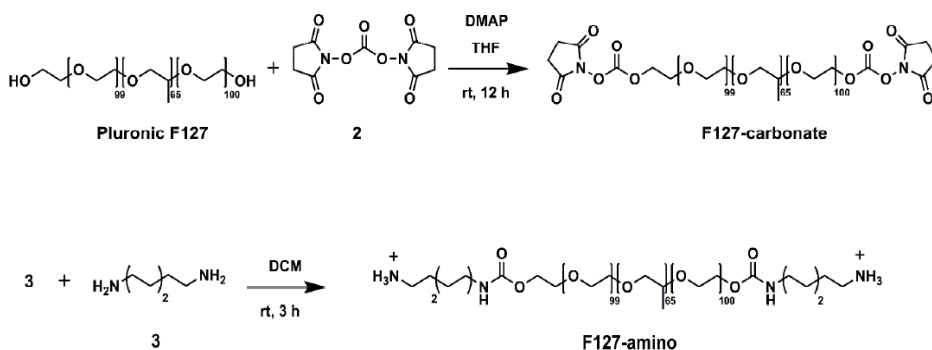


Figure 26. Schematization of the synthesis of F127-amino

Pluronic F127 N-disuccinimidyl carbonate F127-carbonate is synthesized adapting reported procedures¹². A toluene solution of Pluronic F127 (4.01 g, 0.32 mmol, 1.0 eq, 100 mL) is distilled under reduced pressure at 50-60°C in a 250 mL round bottom flask. The residue is dried under vacuum and finally solubilized with 15 mL of dry THF. N,N'- disuccinimidyl carbonate (2) (0.80 g, 3.1 mmol),

solubilized in 7.0 mL of acetone is added. DMAP (0.41 g, 3.32 mmol) was then slowly added at room temperature under stirring by a dropping funnel. After 12 hours, F127-carbonate is precipitated with Et₂O and recovered by centrifugation (25 minutes, 5000 rpm). The precipitate is resuspended and centrifugated several times with acetone (20 mL), until no trace of the excess reagent (TLC, chloroform-methanol 5:1) is present. The product is finally dried under vacuum and directly used for amine functionalization.

Pluronic F127-di-yl bis ((6-aminoesyl)carbamate) F127-amino is synthesized adapting reported procedures¹³. In a flamed 100 mL round bottom flask dried under vacuum, 1,6Diaminohexane (3) (1.908 g, 16.4 mmol) is solubilized with 10 mL of dry DCM. A 10 mL DCM solution of (F127-carbonate) (2.0 g, 0.16 mmol) is then slowly added under stirring at room temperature. After 3 hours the reaction mixture is distilled under reduced pressure and the residue is solubilized with 20 mL of water. The resulting solution is dialyzed vs. Milli-Q water (regenerated cellulose, 12 KDa) for about 20 h under gentle stirring. The dialyzed solution is evaporated under reduced pressure and finally dried under vacuum, obtaining 0.84 g of white solid (yield 42%).

- ¹H-NMR (300 MHz, CDCl₃, 25°C): δ = 8.21 (2H, s, -NHCO-), 5.09 (4H, s, -NH₂), 4.14 (4H, s, -CH₂OCO-), 3.76-3.75 (4H, m, -CH₂CH₂OH), 3.58 (s, -OCH₂CH₂O-) + 3.51-3.42 (m, -OCH₂CCH₃) + 3.33 (m, -OCH₂CHCH₃) ~1000H, 3.09 (4H, s, CH₂NH₂), 1.45 (8H, s, -NHCH₂CH₂CH₂CH₂CH₂CH₂NH₂), 1.25-1.24 (8H, s, NHCH₂CH₂CH₂CH₂CH₂CH₂NH₂), 1.08 (s, -OCH₂CHCH₃) ~195H;
- ¹³C-NMR (100 MHz, CDCl₃, 25°C): δ = 75.7, 75.6, 75.4, 75.3, 73.6, 73.5, 72.2-73.0 (m), 70.0, 17.7, 17.5.

**DYE DOPED AMINO PLURONIC F 127 SILICA
NANOPARTICLES (PluSNPs)**

In a typical preparation of core-shell silica-PEG (poly(ethylene glycol)) nanoparticles, 100 mg of Pluronic F127 (70 mg Pluronic 127 and 30 mg amino modified Pluronic f-127) and the desired amount of the silanized dyes (about 0.7 mg) are carefully solubilized with 1.0–2.0 mL of dichloromethane in a 20 mL glass scintillation vial. The solvent is evaporated from the homogeneous solution by means of a gentle nitrogen flow and subsequently under vacuum at room temperature. NaCl (68.6 mg) is added to the solid residue, and the mixture is solubilized at 25 °C under magnetic stirring with 1565 μ L of acetic acid 1 M. Tetraethyl orthosilicate (TEOS, 179 μ L, 0.8 mmol) is then added to the resulting aqueous homogeneous solution followed by chlorotrimethylsilane (TMSCL, 10 μ L, 0.08 mmol) after 180 min. The mixture is kept under stirring for 48 h at 25 °C before dialysis treatments. The dialysis purification step is carried out versus water on a precise amount of nanoparticle solution (1500 μ L) finally diluted to a total volume of 5 mL with water.

SPECTROFLUOROMETRIC TITRATION

The spectrofluorimetric titration is carried out recording the absorption spectra with a Perkin Elmer Lambda 45, and the emission spectra with Perkin Helmer Ls 55. of solutions with different ratio of nanoparticles and Hyaluronic acid (and Hyaluronic acid alone as a control). These spectra are recorded putting the sample on PMMA plastic cuvette for optical purposes. All the solutions are made from Hya (0.4 μ M LHya and 5.1 μ M SHya) and PluSNPs (20 μ M) water stock solutions. The solutions in cuvette are prepared in different media (d.i. water, Phosphate buffer Ph 7.4, PBS pH 7.4 and PBS pH 5.5). For the fluorescence investigation each sample is excited at 400 nm to observe the quenching of the dye bound to nanoparticles and sensitized emission of the RB and at 530 nm in order to observe the emission of the RB bound to the polymer. Each emission spectrum is corrected by FG factor and by auto-absorption as reported before¹⁴.

DLS

The solutions of Nanoparticle and Hyaluronic acid are prepared in PBS pH 7.4 from the respective stock solution in a Semi-micro sized plastic cuvette. For each cuvette the DLS is measured averaging three runs where ten accumulations of 20 seconds are recorder for the correlation. The analysis is carried out with Zeta-sizer Nano form Malvern instrument with a laser excitation of 633 nm.

FCS

FCS is recorded using the correlator module of Zeiss LSM 880 confocal microscope, exciting the nanoparticle with a laser at 405 nm and the Hya at 564 nm. The measures are obtained averaging ten correlogram obtained recording the fluorescence fluctuations for 20 seconds with a bin time of 10^{-6} – 10^{-4} seconds. The sample are tested on a coverslip posed on 40x water objective with an aperture number of 1.2. The sample are made dissolving the opportune dilution of nanoparticles (10 nM) with different amount of Hyaluronic acids (1, 10 100 nM) in PBS pH 7.4.

Cell culture

The cell culture is provided by Prof. Stefania Rapino from University of Bologna. The HeLa cell are plated in a 35 mm petri optical dish with Dulbecco's Modified Medium 12 hours before the incubation with nanoparticles and hyaluronic acids.

Confocal Microscope

The images of the cells incubated with Rhodamine B labeled PluSNPs and Hyaluronic acid has been obtained with Olympus FV 3000 using a laser excitation of 514 nm and a water-immersion 40x apochromat objective 1.2 NA.

REFERENCES

- 1 S. Biffi, L. Petrizza, E. Rampazzo, R. Voltan, M. Sgarzi, C. Garrovo, L. Prodi, L. Andolfi, C. Agnoletto, G. Zauli and P. Secchiero, *RSC Adv.*, 2014, **4**, 18278–18285.
- 2 E. Rampazzo, S. Bonacchi, D. Genovese, R. Juris, M. Sgarzi, M. Montalti, L. Prodi, N. Zaccheroni, G. Tomaselli, S. Gentile, C. Satriano and E. Rizzarelli, *Chem. - A Eur. J.*, 2011, **17**, 13429–13432.
- 3 M. Helle, E. Rampazzo, M. Monchanin, F. Marchal, F. Guillemin, S. Bonacchi, F. Salis, L. Prodi and L. Bezdetsnaya, *ACS Nano*, 2013, **7**, 8645–8657.
- 4 S. Ganesh, A. K. Iyer, D. V. Morrissey and M. M. Amiji, *Biomaterials*, 2013, **34**, 3489–3502.
- 5 K. . L. L. . M. J. . Z. Y. . X. L. . c W. D. . Liu H.a b Li, *J. Mater. Chem. B*, 2014, **2**, 5238–5248.
- 6 B. Xiao, M. K. Han, E. Viennois, L. Wang, M. Zhang, X. Si and D. Merlin, *Nanoscale*, 2015, **7**, 17745–55.
- 7 K. Fuchs, A. Hippe, A. Schmaus, B. Homey, J. P. Sleeman and V. Orian-Rousseau, *Cell Death Dis.*, 2013, **4**, e819.
- 8 J. E. Rayahin, J. S. Buhrman, Y. Zhang, T. J. Koh and R. A. Gemeinhart, *ACS Biomater. Sci. Eng.*, 2015, **1**, 481–493.
- 9 I. Shulov, S. Oncul, A. Reisch, Y. Arntz, M. Collot, Y. Mely and A. S. Klymchenko, *Nanoscale*, 2015, **7**, 18198–18210.
- 10 E. Rampazzo, S. Bonacchi, D. Genovese, R. Juris, M. Montalti, V. Paterlini, N. Zaccheroni, C. Dumas-Verdes, G. Clavier, R. Méallet-Renault and L. Prodi, *J. Phys. Chem. C*, 2014, **118**, 9261–9267.
- 11 E. Rampazzo, S. Bonacchi, R. Juris, M. Montalti, D. Genovese, N. Zaccheroni, L. Prodi, D. C. Rambaldi and A. Zattoni, 2010, 14605–14613.
- 12 K. Huang, B. P. Lee, D. R. Ingram and P. B. Messersmith, *Biomacromolecules*, 2002, **3**, 397–406.

- 13 M. Soster, R. Juris, S. Bonacchi, D. Genovese, M. Montalti, E. Rampazzo, N. Zaccheroni, P. Garagnani, F. Bussolino, L. Prodi and S. Marchiò, *Int. J. Nanomedicine*, 2012, **7**, 4797–4807.
- 14 A. Credi and L. Prodi, *Spectrochim. Acta Part A Mol. Biomol. Spectrosc.*, 1998, **54**, 159–170.

CHAPTER 6

DEVELOPMENT AND APPLICATION OF A NOVEL FLUORESCENCE CROSSCORRELATION IMAGING TECHNIQUE

6.1 Overview

In this chapter I reported the description of the results obtained during my six-months internship at “Laboratory of Fluorescence Dynamics – LFD”, “University of California”, under the supervision and mentorship of Enrico Gratton and Michelle Digman. The investigation has been focused on the application of a novel two-dimensional FCS techniques called 2D pair correlation function (pCF(δr)). This novel technique is applied for the investigation of the dynamics of a fluorescent labelled protein (Ku-EGFP) inside the nucleus of living cells. Ku protein is involved on the repair mechanism of double strands break (DSB) damage of DNA, which is one of the most hazardous genomic illness. DSB repair occurs with a structural reorganization of the chromatin that can provoke a change on the motion of the proteins which populate the cellular nucleus. To investigate this kind of phenomena techniques, which can permit to obtain information with very high spatio-temporal resolution (100-1000 μm and 10^{-5} to 10^{-3} s) are required. Moreover, these informations should be achieved on two-dimensional fashion because dynamic process can occur simultaneously in different cellular sectors. The innovative approach of 2D pCF is proposed as a promising tool to discover the physics behind biological phenomena giving information about the dynamics of the fluorescent object of interest. This very promising technique is in principle suitable for any fluorescent probe including dyes, nanostructures and 2D-pCF, that can be used for the description of processes involving

cellular uptake and localization of fluorescent theranostic materials.

6.2 pCF(δr)

The 2D-pCF approach was developed from the results showed in a paper written by Michelle Digman and Enrico Gratton in 2009 called “Imaging Barriers to Diffusion by Pair Correlation Functions”. The basic idea behind the pair correlation method is to statistically follow the same particle during its diffusion. In this work they followed a fluorescently labeled molecule in the membrane. The fluorescence intensity fluctuation was rapidly sampled at each point in the 2D plane (grid in Figure. 1). Only the same molecule will produce an average cross correlation with a given time delay at two different points in the grid. A positive correlation will occur if the fluctuation of the intensity of a molecule at position 2 interferes with the fluctuation of the intensity at position 1, i.e., only if the same molecule is moving there with a given time delay. If a barrier to diffusion (indicated by the blue line in figure 1) is present, there will be a lag of correlation between position 3 and 4. If the molecule hits an obstacle that is penetrable (but with a certain retention time inside the obstacle) or it diffuses around the obstacle, a delayed correlation compared to the free diffusion will be observed (Figure. 1)¹.

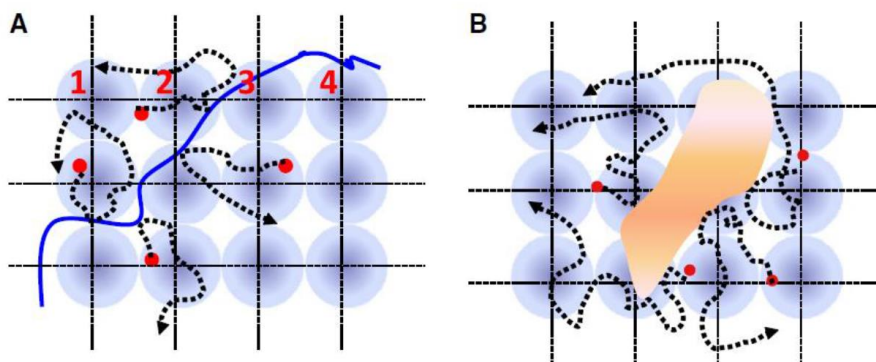


Figure 24. Schematic representation of the spatial pair-correlation method¹.

The used pair correlation function (pCF) is defined as follows:

$$G(\tau, \delta r) = \frac{\langle F(t,0) \cdot F(t+\tau, \delta r) \rangle}{\langle F(t,0) \rangle \langle F(\tau, \delta r) \rangle} - 1 \quad \text{Eq. 1}$$

where δr is the distance between the two points and τ is the delay time, $F(t, \delta r)$ is the fluorescence intensity at the time t and the distance δr from the origin. For each pixel of the image the pCF is calculated for all the adjacent neighbour pixels in a circle around the pixel of interest at a given pCF distance δr . For each direction, a pCF function with a maximum is obtained at a certain delay time if the correlation is positive, while no maximum is obtained if no correlation can be found. The maximum position is proportional to the average time that a molecules takes to travel a certain distance. From the delaytimes of the maxima in each direction is derived a weighted ellipsoid (Fig. 2, c-d) for the pixel of interest, i.e. the diffusion ellipsoid.

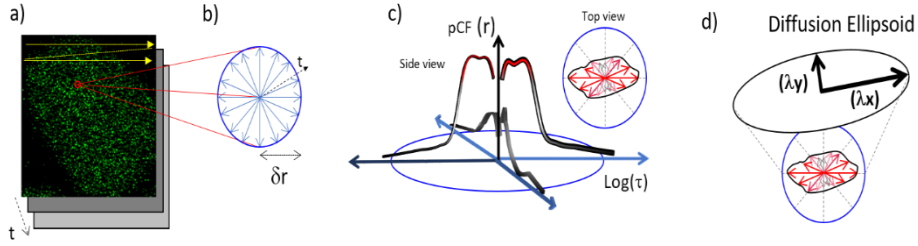


Figure 25. a) Laser scansion frames acquisition sample. b) Representation of the stellate pCF. c) Correlation plot and 2d projection. d) Diffusion tensor computed on the trajectories.

With the information about the first and second momentum of the center of mass of the diffusion ellipsoid, it is then possible to calculate the following parameter:

$$\text{Anisotropy} = \frac{\lambda_y - \lambda_x}{\lambda_y + \lambda_x} \quad \text{Eq. 2}$$

$$\text{Eccentricity} = \sqrt{1 - \frac{\lambda_y}{\lambda_x}} \quad \text{Eq. 3}$$

The Anisotropy and the Eccentricity are both ratios of the major axis of the ellipsoid. The scale for both of them is in the 0 – 1 range. These two dimensionless parameters represent the elongation of the diffusion ellipsoid. In particular, for anisotropy a value of 0 would represent a perfect circle (isotropic diffusion) and a value of 1 would represent a straight line.

From the 2DpCF the connectivity map is computed similarly to the streamline tracking. The basic principle of streamline tracking is to apply an angle of a certain width in the orientation of the direction arrow (direction of the major axis of the ellipsoid) of a pixel of interest to an adjacent direction arrow. If the orientation of the direction arrow is within the angle, the

track is continued. If the orientation of the direction arrow is not within the angle, the track ends. The trajectories computed are displayed in a 2D connectivity map (Figure 3, c-f).

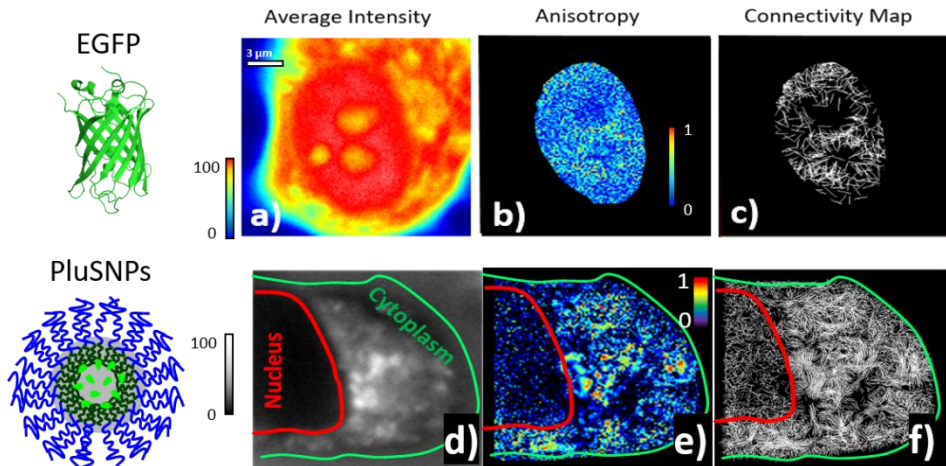


*Figure 3. TOP - HeLa cell expressing GFP, a) Average Intensity, b) Anisotropy Map, c) Connectivity map (0.1-1 anisotropy). BOTTOM HeLa Cell incubated with 0.1 μM of Rhodamine B doped Pluronic silica nanoparticles d) Average Intensity, e) Anisotropy Map, f) Connectivity map (0.1-1 anisotropy) pCF (5) computed on 8200 frames 37 ms*frame ($\lambda_{\text{ex}}=900$ nm 2-photon laser for GFP and $\lambda_{\text{ex}}=514$ nm single photon for Nanoparticles).*

6.3 DOUBLE STRAND BREAK – DNA DANGEROUS DAMAGE

Each of the 10^{13} cells in the human body receives tens of thousands of DNA lesions per day. These lesions can block genome replication and transcription, and if they are not repaired or are repaired incorrectly, they lead to mutations or wider-scale genome aberrations. The variety of possible damages is quite wide starting from a single base to a big DNA fragment denaturation. The repair machinery works in

continuous considering the frequency at which DNA damage occurs daily.³

As already mentioned, one of the most dangerous damage is the double strands break (DSB), which can be caused by irradiation, chemical agents, or ultraviolet light (UV). Double-strand breaks, in which both strands in the double helix are severed, are particularly hazardous to the cell because they can lead to genome rearrangements.

In general, *in vitro* DNA damage and repair do not occur on a naked DNA template but on chromatin where DNA is complexed with histones and compacted into higher-order structures. The DSB repair mechanism seems to involve different chromatin structures where the proteins can experience a change in the mobility after the damage. E. Hinde et al. revealed the importance of a suitable technique in order to discover the time scale of DSB induced effects on the mobility of nuclear protein. The technique used by E. Hinde is the line pair correlation function useful to investigate with very high resolution on the time correlations details the changes of the motion of two fluorescent proteins (Ku-EGFP and GFP) by analyzing small nuclear regions. The study revealed how chromatin undergoes to a rearrangement leading to the decrease of organization in the damaged region and to an increase in compaction in adjacent regions. All these processes together facilitate DNA repair factor recruitment to the micro-irradiated region with high spatiotemporal control. Indeed, the effects of a DSB can influence the behavior of chromatin of the entire nucleus, so 2D-pCF technique is proposed here as a promising way to highlight dynamic effect on a big cellular sector as the entire nucleus, enabling the calculation of a map of the processes.

6.4 DSB REPAIR MECHANISMS

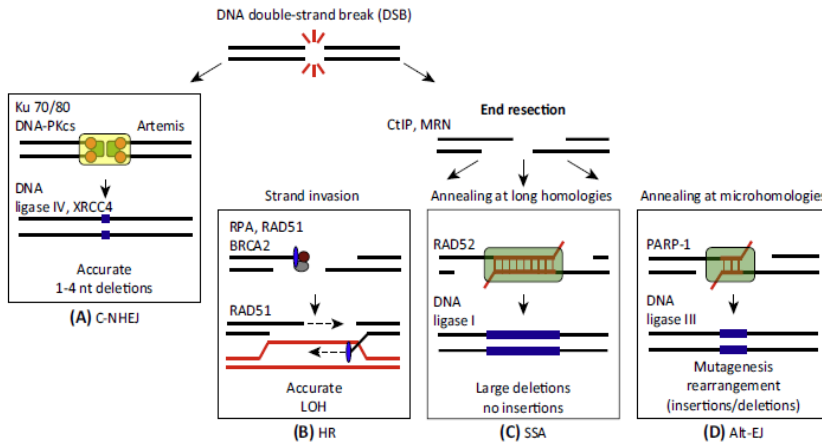


Figure 4. Schematic representation of the two DSB repair mechanism, from left A) non-homologous end joining (NHEJ), B) homologous recombination (HR), C) single-strand annealing (SSA) and D) alternative end-joining (Alt-EJ)⁵.

Many mechanisms are today proposed for the repair of double-strand breaks, the two main ones are: non-homologous end joining (NHEJ) and homologous recombination (HR). NHEJ is defined as "non-homologous" because the break ends are directly ligated without the need of a homologous template, in contrast to homology directed repair, which requires a homologous sequence to guide repair. NHEJ typically utilizes short homologous DNA sequences called microhomologies to guide repair. These microhomologies are often presented in single-stranded overhangs on the ends of double-strand breaks. When the overhangs are perfectly compatible, NHEJ usually repairs the break accurately. As showed on the figure where the two different processes are represented, KU proteins are directly involved on the NHEJ process^{5,6}. These

two processes lead to the complete repair of the DSB but can lead as well to imperfection and errors. Moreover, the DSB is not always completely repaired: the damage can thus activate parallel processes promoting different cell pathways as apoptosis or cell death.

6.5 HeLa - LASER DAMAGE INDUCE DOUBLE STRANDS BREAK

DSB can be induced on chromatin by different kinds of source of energy, such as X-ray exposure or high intensity UV-visible light.⁷ 2-photon laser at 780 nm provide, as reported previously, a controlled way to obtain a DSB damage, and it can operate on a very small nuclear volume avoiding membrane and nuclei illness.⁸ We have performed 2-photon laser irradiation using different laser powers in order to have the information on the relationship between the delivered energy able to generate DSB and the cellular effects. In the case of HeLa cells expressing Ku-EGFP, a localized laser having sufficient power to provoke DSB induces a recruitment process for this protein on the damaged region with a very fast kinetics.⁹ The recruitment induces an increase of the protein concentration (measured by an increase of the fluorescence intensity) on the damaged region. This process is correlated to the NHEJ mechanism, describing at molecular level a binding of Ku on the broken DNA strand ends.

On the contrary, upon damaging HeLa cells expressing EGFP, the recruitment does not occur within the tested laser power range and no effect on the fluorescence intensity appears (Figure 5). This confirms that laser irradiation modifies the behavior only of Ku, which is activated after the occurrence of DSB.

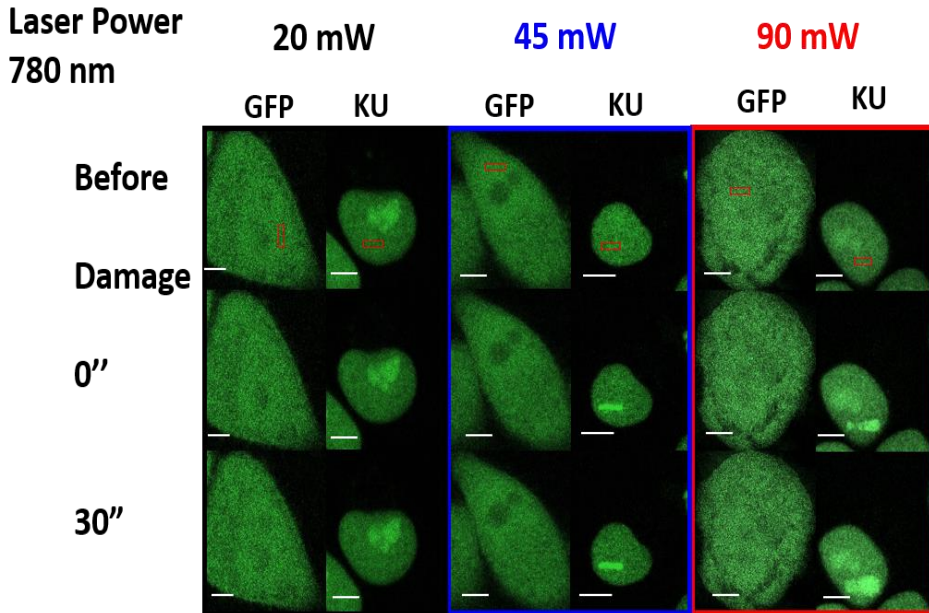


Figure 5. Comparison of EGFP and KU-EGFP expressing cell damaged with 780 nm two photon laser with different laser powers. (scale bar 3 μ m)

The intensity ratio after/before the damage allows to investigate the relationship between the amount of energy delivered and the protein behavior. In the case of Ku-EGFP, an increase of the ratio of fluorescence intensity after/before damage, computed on the damaged region, occurs as a function of the laser power. This increase of fluorescence intensity is related with an energy dose-depending effect that can influence the DSB formation and the relative Ku binding. For EGFP, which is an inactive protein in the process related with DSB, the fluorescence intensity ratio is constant.

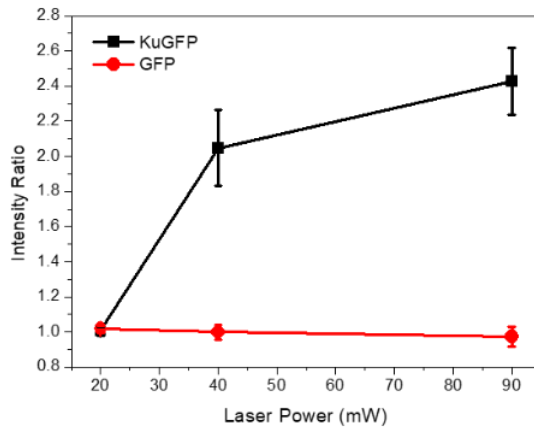


Figure 6. Fluorescence intensity ratio after/before damage in function of laser power of KU-EGFP (black line) and EGFP (red line).

Immediately after the irradiation, Ku-EGFP is recruited on the damaged region. Here Ku-EGFP/DNA complexes evolve over time; for this reason the behavior has been monitored up to 240 min after damage. Ku-EGFP/DNA complexes decrease in size, highlighting, probably, the beginning of the DSB repair. After 60 min from the irradiation, Ku forms small aggregates on domains called foci spread on the entire nucleus.¹⁰

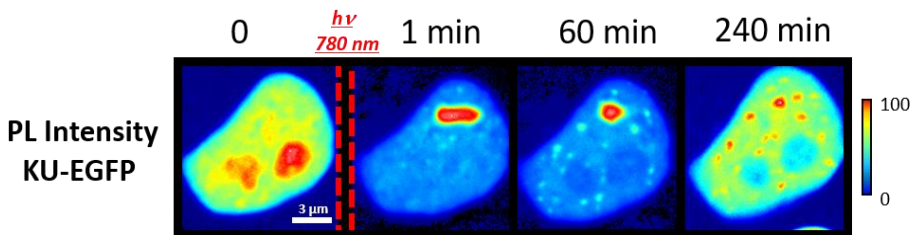


Figure 7. Ku-EGFP fluorescence intensity time evolution after damage.

The foci formation is a process that can be regulated by a chromatin structural reorganization. To study the evolution of the irradiated region and of the foci on the entire nucleus the

use of two-dimensional techniques able to discriminate dynamic events becomes even more necessary.

2D-pCF can be computed selecting different pixel distances: this parameter allows, on the same data set, to highlight processes occurring in different time/space scale. For this reason, 2D-pCF is proposed here as the right tool to highlight chemical-physic information in two-dimensional fashion of complex system: this tool is in fact able to discriminate different dynamic processes with the same frames acquisition.

6.6 Ku-EGFP Motion Anisotropy - Damage effect

2D-pCF analysis led to represent the motion anisotropy map and the computation of the average anisotropy value (on the entire masked region). Before the damage, the highest anisotropy is visible close to the nuclear membrane because for Ku this structure is a physical barrier (the protein is expressed only inside the nucleus) which block the diffusion and influence the possible orientation of the motion. The maps acquired for not damaged cells from the beginning to the last acquisition (0 to 240 min) reveal the same behavior of anisotropy, confirming the orientation of the motion in this region before irradiation. When DSB is provoked by the 780 nm 2-photon laser, on the edges of the damaged area Ku recruitment set off an increase of anisotropy indicating the formation of an obstacle which can be due to the complex of the damaged DNA and this protein. At the same time, close to the membrane, the motion become structureless probably because of the recruitment activation (decrease of the anisotropy close to the membrane). The formation of the foci occurs and the recruitment size decreases on irradiated area,

changing drastically the anisotropy computed by 2DpCF (Figure 8).

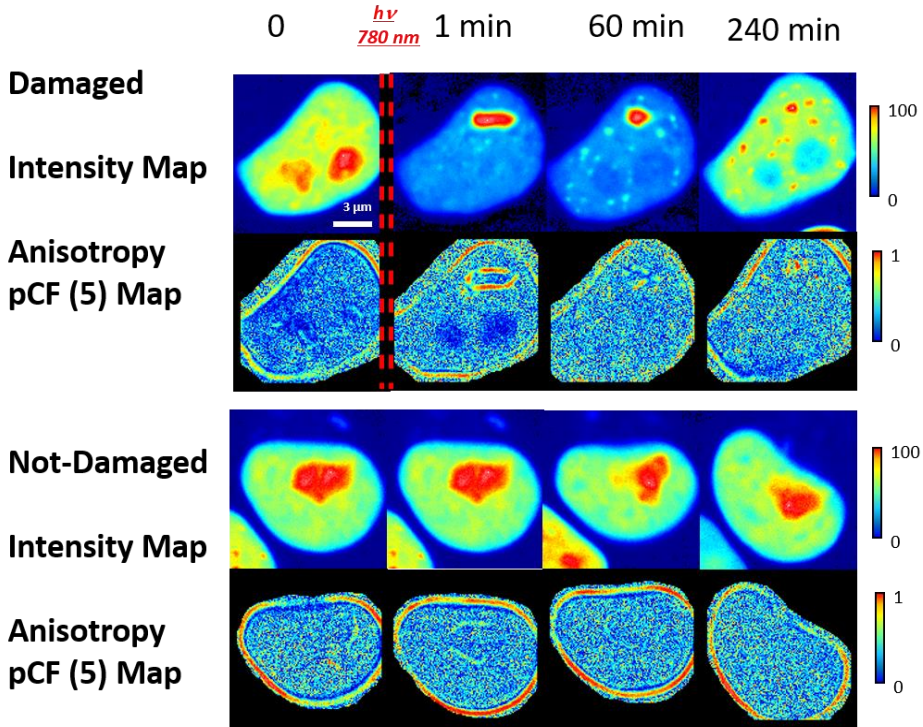


Figure 8. Fluorescence intensity and anisotropy map for damaged cell and control cell (top and bottom, respectively).

The computation of the averaged anisotropy value measured on the collected pixels allows to have a statistical information about the effect of the DSB correlated proteins response of the entire nucleus. The localized irradiation causes an averaged increase of the motion anisotropy which is due to the activation of Ku proteins. The effect of damage is confirmed analyzing the anisotropy of the not damaged cells, which is constant, indicating that the changes of motion are due to DSB (Figure 9). In general, for the motion of protein in complex

environments, an anisotropy increase can be described as an increase of motion compartmentalization.

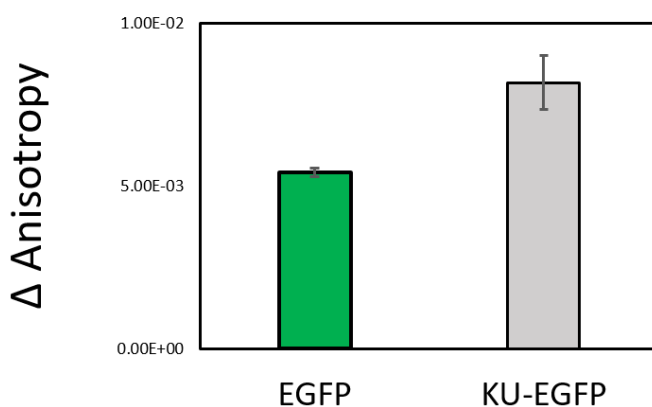
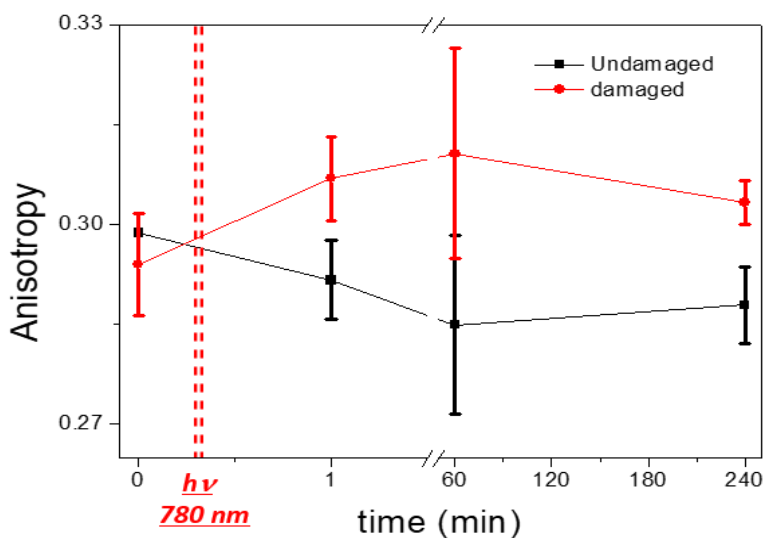


Figure 9. Top, Anisotropy trends of not damaged cells (black line) and 90 mW damaged HeLa Ku-EGFP expressing cells (red line) over time. Bottom: variation of motion anisotropy (Δ Anisotropy=1h after – before) after one hour from irradiation of EGFP (green) and Ku-EGFP (grey).

The effect of the damage and the activation of the repair processes on the chromatin can be described by the trajectories obtained computing the connectivity map. This tool provides a very detailed map of the connections and the barriers in the system. To rationalize the trajectories can be useful to focus the description about region of interest as the damaged sector, the nuclear membrane and the foci. The connectivity map (Figure 10) at correlation distance of 5 pixels, describes a short-range mobility in a fast time scale. In these conditions connectivity maps reveals the changes of Ku motion close to the membrane provoked by the irradiation. The motion, close to nuclear barrier is composed by trajectories tangential to the membrane, where statistically Ku motion becomes more discontinued once chromatin is damaged. Close to DSB region and to Foci the trajectories highlight the process of Ku recruitment. The connectivity map of EGFP doesn't show any significant evidence of changes on the trajectories. This fact confirms that there are not observable effects of damage on the EGFP anisotropy and on the fluorescence intensity.

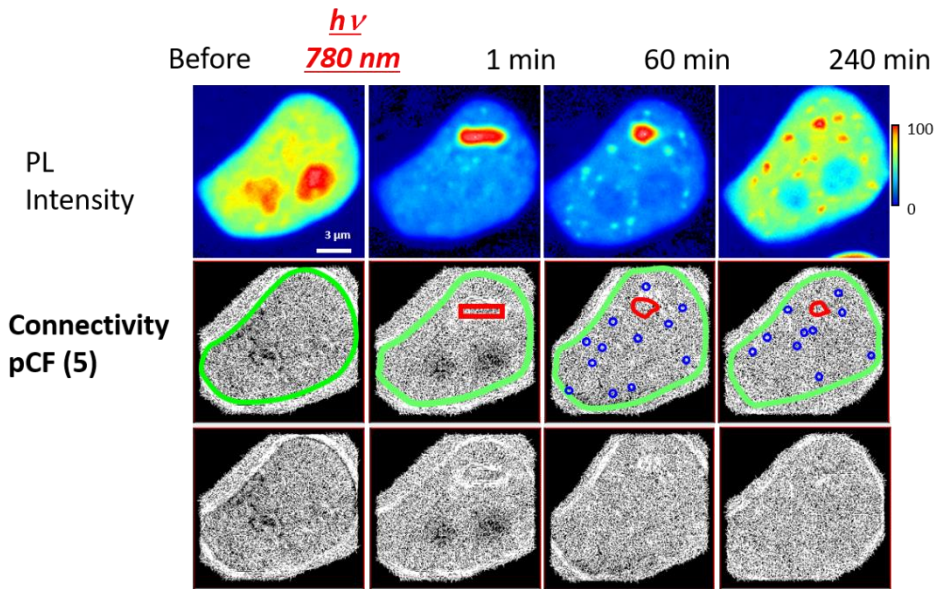


Figure 10. From top to bottom: fluorescence intensity map of Ku-GFP expressing HeLa cell before immediately, 60 and 240 minutes after the damage. Relative connectivity map computed at 5 pixels of correlation distance. Membrane is highlighted in green, damaged in red and foci in blue.

Changing the correlation distance, it is possible to control the spatiotemporal scale of the correlation which can be useful to highlight different processes. For this reason, here is reported a comparison between the output of different correlation distance: at 5 (700 nm) and at 10 pixels (1400 nm). Focusing on the damaged region, the anisotropy map shows two different patterns of obstacles which involved directly Ku proteins. The different pattern between 5 and 10 pixels is confirmed by the connectivity map where different trajectories are highlighted. In this region two different time scale processes are proposed, i.e.: pCF (5) short and fast recruitment and pCF (10) slower Ku reorganization probably

combined with big chromatin displacement. These results can provide a good example suggesting the importance of the development new two-dimensional techniques with a high spatiotemporal control where the traditional line correlation cannot allow description of a whole cellular sectors (Figure 11).

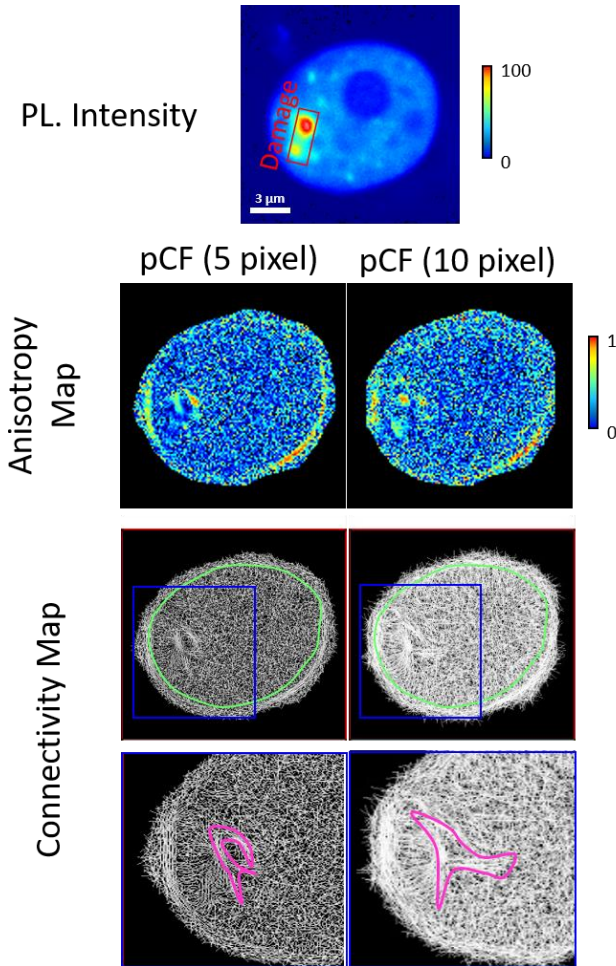


Figure 11. from the top to the bottom: Intensity map of KUEGFP expressing cell damaged with 90 mW at 780 nm. Anisotropy map computed at correlation distance 5 and 10 pixels. Connectivity map computed at 5 and 10 pixels and zoom close to damaged region.

6.7 Inhibition of DNA Damage Response

In order to maintain genomic stability, cells have developed sophisticated signaling pathways to enable DNA damage or DNA replication stress to be resolved. As key mediators which are involved in this DNA damage response (DDR), different proteins can be considered: the ATM and ATR kinases, PARP and DNA-PK, which are able to induce cell cycle arrest and to facilitate DNA repair via their downstream targets. Inhibiting the DDR has become an attractive therapeutic concept in cancer therapy, since (i) resistance to genotoxic therapies has been associated with increased DDR signaling, and (ii) many cancers have defects in certain components of the DDR rendering them highly dependent on the remaining DDR pathways for survival.¹³ The knowledge on the repair mechanism and the related chemical physical behavior of the chromatin could open the possibility to formulate new therapeutic tools able to control the DDR. For this reason, to understand the interconnection between different cell repair processes that can influence the dynamic of chromatin, three kinds of inhibition have been selected.

6.7.1 PARP

Poly(ADP-ribose) polymerase (PARP) is a family of proteins involved in a number of processes such as , genomic stability, and ¹⁴. PARP can be activated in cells experiencing stress and/or DNA damage. Activated PARP can deplete the ATP of a cell trying to repair the damaged DNA. ATP depletion in a cell can lead to lysis and cell death (necrosis). The PARP inhibition (PARPi, final i is for inhibitor) should works primarily by blocking PARP enzyme activity, thus preventing the repair of DNA damage and ultimately causing cell death.^{14–17}

6.7.2 DNA-PK

DNA Protein Dependent Kinase (DNA-PK) is an enzyme that is involved in NHEJ, which rejoins double-strand breaks. Autophosphorylation of DNA-PKs appears to play a key role in NHEJ and is thought to induce a conformational change that allows end processing enzymes to access the ends of the double-strand break. DNA-PK also cooperates with ATR and ATM (A-T, ataxia–telangiectasia; ATM, ataxia–telangiectasia mutated; ATR, ataxia–telangiectasia and Rad3 related) to phosphorylate proteins involved in the DNA damage checkpoint. For this reason, the other two kinds of inhibition tested are DNA-PKi and ATMi and DNA-PKi+ATMi+ATRi¹⁸.

6.7.3 ATM and ATR

ATM and ATR are members of the phosphatidylinositol 3-kinaserelated kinase (PIKK) family of serine/threonine protein kinases. The cellular functions of these protein kinases range from regulation of the DNA damage response (DDR) to cell survival, proliferation, metabolism, differentiation, motility and nonsense-mediated mRNA decay¹⁹.

6.8 Inhibition effect on the KU-EGFP motion

The biological effects of these kinds of inhibition are today still under investigation. There are many examples of cellular DDR behaviors where active proteins are inhibited²⁰. Here is proposed 2D pCF, as a powerful tool able to disclose the effect of inhibition of DDR on Ku-EGFP mobility. This investigation indicates some chromatin structural changes when some processes are repressed before and after the irradiation. The motion anisotropy computed at 5 pixels of correlation distance (Figure 12) indicates which are the effects of these inhibitors on Ku mobility before and after the damage. Higher average value of anisotropy can represent different kinds of diffusion related to an increase of compartmentalization of chromatin. Probably, repressing certain processes, the cells are stimulated to

overcome the inhibitions, and this can alter the mobility of Ku-EGFP proteins also before the DSB formation.

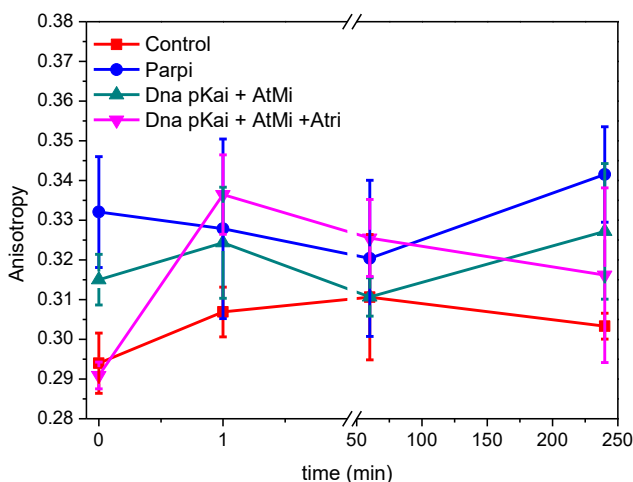


Figure 12. Trends of the Motion Anisotropy for: Control (red line), PARPi (blue line), DNA-PKi+ATMi (dark green line) and DNA-PKi+ATMi+ATRI (purple line) inhibitors. DSB induced with 90 mW at 780 nm.

The inhibitors tested can influence other processes not only related with DDR. Probably the increase of anisotropy of DNA-PKi+ATMi+ATRI provoked by the damage and the relative high anisotropy after one hour can be correlated to process of Ku/foci formation. Indeed, counting the number of foci formed after one hour from the damage, the highest number of foci is revealed under the effect of this inhibitor, (Figure 13, A).

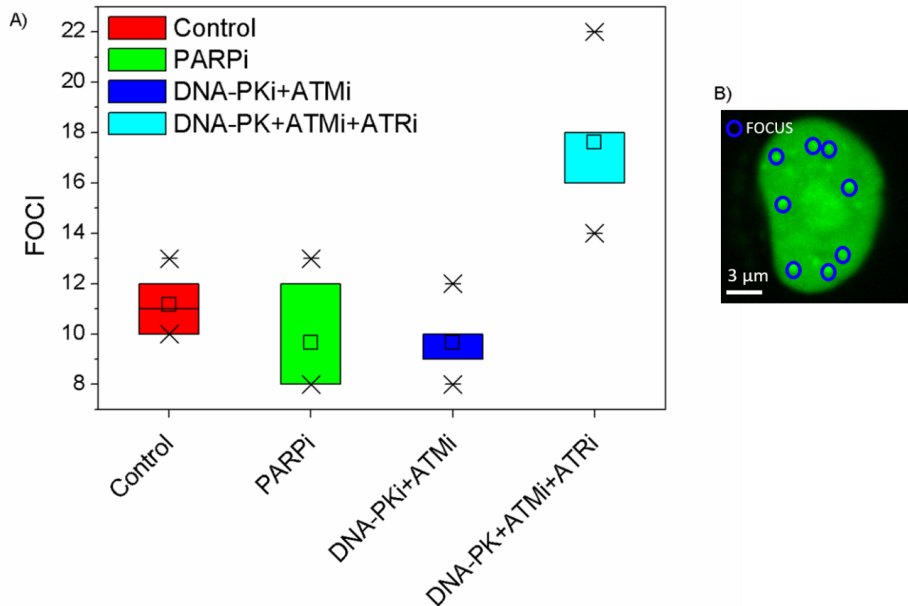


Figure 26. A) Box plot of number of foci expressed after one hour from damage with laser power of 90 mW at 780 nm for: control as no inhibited (red box), PARPi (green box), DNA-PKi+ATMi (Blue box) and DNA-PKi+ATMi+ATRi (cyan box). B) KU-EGFP expressing cell where FOCI are marked in blue.

To explain a possible reason about the relationships between the highest number of foci and the average increase of anisotropy, it is useful to understand how the foci are structured. In order to understand the structure of foci a colocalization of two different labels has been carried out staining with Ku red antibody and green antibody for Telomeric repeat-binding factor 2 (a protein which protect and regulate the telomeres length).

Firstly, for Ku red, the foci are highlighted as well as the Ku-EGFP expressing cells, demonstrating the natural formation of these aggregates after irradiation. We co-stained cells Ku and telomeric factor are colocalized in the foci as well as in the damaged region (Figure 14). This could mean that the Ku recruitment process related to the DDR involves chromatin components as the telomeres which

can change chromatin structure altering the mobility of certain proteins inside the nucleus.

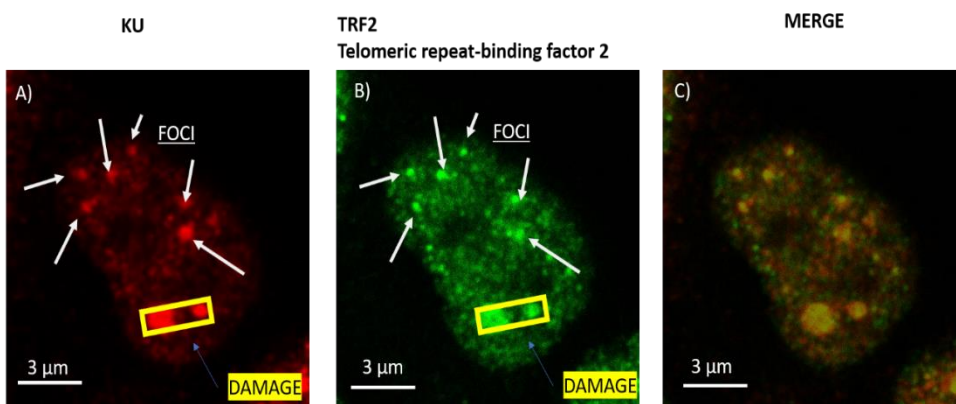


Figure 27. HeLa cell fixed and co-stained with A) KU red antibody marker, B) TRF" green antibody marker C) merged images

6.9 CONCLUSION

Here I reported the application of a novel fluorescence two-dimensional correlation technique for the investigation on the dynamic repair process of double strand break of DNA. These processes are induced by the irradiation with high power two-photon laser at 780 nm in a small region of the cellular nucleus.

In particular, the technique provided, with very high spatiotemporal resolution, the information on motion anisotropy of EGFP and Ku-EGFP, a DSB repair active fluorescent labeled protein. The final outputs of 2D-pCF are anisotropy and connectivity map. Anisotropy map shows how is structured the motion and the connectivity highlights the pattern of trajectories before and after the irradiation yielding which is the behavior of physical chemical properties of Ku when DSB occurs.

The application of 2D-PCF to DDR response allowed calculating the effect of the damage on local recruitment processes involving Ku. Indeed, when HeLa cells are damaged two different processes for Ku are observed: the recruitment on the damaged region with very

fast kinetics (few seconds after irradiation) and, on longer time scale, the recruitment on structure called foci (slow kinetics 30 minutes).

These biological processes are related to DDR and can be investigated looking how this protein moves inside the nucleus. The DSB damage can remodel the chromatin changing the mobility of Ku provoking an increase of the anisotropy. This can be described as an increase of the compartmentalization for Ku which can find more obstacles during its activity while for EGFP, an inactive protein, anisotropy is constant.

Moreover, I have investigated the effects on the motion of Ku provoked by three different DDR inhibitors that influence how this protein can move inside the nucleus. The inhibition of DDR processes can influence the Ku mobility as well as the number of foci formed. In particular DNA-PKi+ATMi+ATRi inhibition induces the formation of the highest number of foci and the biggest increase of anisotropy which can be described by colocalization of Ku and telomeres binding factor which is one of the responsible of protecting and regulating the telomere length.

Concluding, I believe that 2D-pCF is a powerful method which can provide the access to physical chemical information, in a two-dimensional form, of dynamic processes of nanostructured fluorescent materials (ranging from protein to nanoparticles), useful to improve the knowledge on biological processes and, in the future, for the development of theranostic nanomaterials.

6. 10 Technical Notes

Laser Damage

In this investigation the damage has been achieved by irradiating at 780 nm with 2-photon laser. This treatment has been carried out inducing with a linear scansion, in a small

region of interest (0.3 by 3 μm , a scan speed of 16 $\mu\text{s}/\text{pixel}$) with different laser powers (0, 40 and 90 mW).

Laser scanning Acquisition Method for 2D pCF(δr)

2D-pCF analysis, similarly as the other correlation techniques needs a discrete number of events (fluctuations) to have reliable statistics able to gain correlation functions with a good resolution.

The acquisition in terms of pixel dwell time is another crucial parameter which, as reported previously, control the time scale of the correlation^{11,12} To get the best compromise of the frame acquisition and scan speed aiming the time resolution of the processes involved, the data suitable for 2D-pCF are acquired using a confocal Microscope Zeiss LSM 880 recording 8200 frames with very fast laser scansion (37 ms per frame a pixel size of 140 nm and a frame of 128 by 128 pixels). To avoid side effects during the scansion due to the long exposition of the cell to the laser for the scansion a very delicate two-photon excitation at 900 nm (about 0.8 mW) is used to acquire the frames selecting the lowest laser power to avoid photobleaching (which can alter the correlation as well).

Laser damage and the frame acquisition for the 2D-pCF analysis have been carried out using water immersion apochromat 40x objective with NA 1.2

2D-pCF pixel distance and analysis

The pixel distance for the correlation is a key parameter, since at different distance, the analysis can highlight phenomena which occurs in different spatiotemporal scales. Experimentally, the pixels distances choice to compute the pair

correlation function in this work are 5 and 10 pixels (PSF about 3 pixels). In order to get statistical information pCF analysis is carried out on the nucleus on a set of three cells at list, selecting a region of interest designed including the nuclear envelop

Inhibition Protocol

Each inhibitor is dissolved in DMSO. The cells are incubated with the inhibitor solution in DMEM for one hour and before the imaging the medium is changed. Below the percentages are in v/v. For each cell treatment, the inhibitor stock is mixed in the cellular medium as follow:

Control -> 0.24% DMSO

PARPi -> 0.1% PARPi +0.14% DMSO

DNA-PKi + ATMi -> 0.1% ATMi + 0.1%DNA-PKi +0.04 DMSO

DNA-PKi + ATMi + ATRi -> 0.1% ATMi + 0.04%ATRi +0.1%DNA-PKi

Staining

HeLa cells are damaged in the same way described before. The cells are co-stained after PFA fixation (carried out one hour after damaging) with red marker antibody for KU and a green marker antibody for TRF2 (Telomeric repeat-binding factor 2).

References

- 1 M. A. Digman and E. Gratton, *Biophys. J.*, 2009, **97**, 665–673.
- 2 C. Di Rienzo, F. Cardarelli, M. Di Luca, F. Beltram and E. Gratton, *Biophys. J.*, 2016, **111**, 841–851.
- 3 S. P. Jackson and J. Bartek, *Nature*, 2009, **461**, 1071–1078.

- 4 E. Hinde, X. Kong, K. Yokomori and E. Gratton, *Biophys. J.*, 2014, **107**, 55–65.
- 5 R. Ceccaldi, B. Rondinelli and A. D. D’Andrea, *Trends Cell Biol.*, 2016, **26**, 52–64.
- 6 L. Liang, L. Deng, Y. Chen, G. C. Li, C. Shao and J. A. Tischfield, *J. Biol. Chem.*, 2005, **280**, 31442–31449.
- 7 X. Kong, S. K. Mohanty, J. Stephens, J. T. Heale, V. Gomez-Godinez, L. Z. Shi, J. S. Kim, K. Yokomori and M. W. Berns, *Nucleic Acids Res.*, , DOI:10.1093/nar/gkp221.
- 8 A. J. Hartlerode, M. J. Morgan, Y. Wu, J. Buis and D. O. Ferguson, *Nat. Struct. Mol. Biol.*, 2015, **22**, 736–743.
- 9 P. Reynolds, J. A. Anderson, J. V. Harper, M. A. Hill, S. W. Botchway, A. W. Parker and P. O’Neill, *Nucleic Acids Res.*, 2012, **40**, 10821–10831.
- 10 S. Britton, J. Coates and S. P. Jackson, *J. Cell Biol.*, 2013, **202**, 579–595.
- 11 E. Hinde, F. Cardarelli, M. A. Digman and E. Gratton, *Biophys. J.*, 2012, **102**, 691–697.
- 12 E. Hinde, F. Cardarelli, M. a Digman and E. Gratton, *Proc. Natl. Acad. Sci. U. S. A.*, 2010, **107**, 16560–16565.
- 13 S. Bekker-Jensen, C. Lukas, R. Kitagawa, F. Melander, M. B. Kastan, J. Bartek and J. Lukas, *J. Cell Biol.*, 2006, **173**, 195–206.
- 14 M. Wang, W. Wu, W. Wu, B. Rosidi, L. Zhang, H. Wang and G. Iliakis, *Nucleic Acids Res.*, 2006, **34**, 6170–6182.
- 15 A. G. Patel, J. N. Sarkaria and S. H. Kaufmann, *Pnas*, 2011, **108**, 3406–3411.
- 16 C. Beck, I. Robert, B. Reina-San-Martin, V. Schreiber and F. Dantzer, *Exp. Cell Res.*, 2014, **329**, 18–25.
- 17 C. Godon, F. P. Cordelières, D. Biard, N. Giocanti, F. Mégnin-Chanet, J. Hall and V. Favaudon, *Nucleic Acids Res.*, 2008, **36**, 4454–4464.
- 18 K. Meek, V. Dang and S. P. Lees-Miller, *Adv. Immunol.*, 2008, **99**, 33–58.

- 19 A. Ciccia and S. J. Elledge, 2011, **40**, 179–204.
- 20 F. Rossiello, J. Aguado, S. Sepe, F. Iannelli, Q. Nguyen, S. Pitchiaya, P. Carninci and F. d’Adda di Fagagna, *Nat. Commun.*, 2017, **8**, 13980.

CONCLUSIONS

Theranostic nanomaterials and genome interpretation are expected to provide solutions for unsolved medical problems allowing better life conditions and improving life expectation of patients. Nevertheless, since biological environments are very complex and nanoparticles, interacting with macro-molecules, form self-assembled structures referred as biomolecular corona, it is very important to consider that they will present different chemical/physical properties, biological activity and biodistribution in these conditions. It is therefore evident that to understand and control these interactions is of great importance for the application of new nanomaterials in medicine.

The results obtained in this PhD thesis provide precious information on the design and preparation of nanomaterials for theranostic applications based on dye doped Pluronic F-127 Silica Nanoparticles and for the development of fluorescence-based methods or technical tools for an improved characterization of such materials especially in a biological environment.

In particular, I have investigated a new method based on fluorescent solvatochromic dyes (Prodan and Nile Red), that can be conveniently used to map the polarity of neighboring nanoenvironments (chapter 3) in order to understand the composition of complex nanoarchitecture, as PluSNPs. For these nanoparticles we were able to evidence the complex architecture of the Pluronic shell, its multi-polarity gradient from the inner, more lipophilic part, to the more hydrophilic outer one, ruling the host/guest abilities of these structures. These results obtained for a particular nanostructure, are extremely interesting; but it is important to underline that the method can be of general application, being suitable for the mapping of nano-polarities in many nanostructured materials and, in general, in soft interfaces.

I have then taken advantage from the information gained with the solvatochromic method to design PluSNPs for drug delivery purposes and, with suitable changes in the synthetic strategy, I have been able to incorporate in a single nanostructure, an average of 70-100 units of Sorafenib Tosylate, a very common chemotherapeutic lipophilic drug (chapter 2). This drug is widely used in clinical practice for the treatment of renal and liver carcinoma. We monitored in controlled conditions *in vitro*, the release kinetic of this drug from the particles occurring in more than two days, an already very good result that can be still tuned and optimized in the next future. Moreover, the same drug delivery nanoplatform has revealed very promising anti-angiogenic properties in several *in vitro* dedicated cellular tests.

As already mentioned, we were well aware that to tune these properties it is fundamental a deep understanding of the formation of the biomolecular corona. To this goal we have investigated a kind of model system following the interactions among PluSNPs and two dye labeled hyaluronic acids with different molecular weights (chapter 5). Interestingly, we were able to monitor the conformational reorganization of the hyaluronic acid by observing the changes on the optical properties of the Rhodamine B chemically anchored to the hyaluronic acid chains induced by these interactions. Further evidences and a deeper understanding have been possible by following the energy transfer process among Rhodamine B and suitable fluorophores embedded in the core of *ad hoc* designed nanoparticle. We have followed the hyaluronic acid/PluSNPs nanoparticles ensemble with two different correlation techniques (DLS and FCS). Moreover, we monitored the biological effect of these self-assembled nanoarchitectures observing their uptake in a tumor cell line *in vitro*. Interestingly, the interaction with the Hyaluronic acid makes the internalization of PluSNPs faster, a result that, if confirmed also *in vivo* could be of significant importance for the optimization of the drug delivery process.

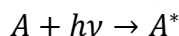
In the last part of my research work I have tested and optimized the application of a novel fluorescence cross correlation technique developed at Laboratory of Fluorescence Dynamics of University of California, namely 2D-pCF. As also shown by this work, this technique is able to provide the maps of dynamical processes yielding statistically the motion anisotropy and trajectories of fluorescent objects inside cells with very high spatiotemporal resolution. 2D-pCF can be useful for the description of different phenomena related to nanoparticle intracellular localization. With the aim to follow a step by step approach, as a first model I focused the investigation on chromatin reorganization monitoring the dynamical processes of a protein involved in the repair mechanism of DNA double strands breaks. I evidenced that when DNA is damaged, the chromatin undergoes a reorganization that changes the motion of the proteins responsible for the protection of DNA and in general of nucleic materials. Although only few preliminary tests have been carried out on PluSNPs, this technique can be easily extended also to most fluorescent nanoarchitectures, representing a powerful tool to follow different processes inside cell.

I believe this work can provide interesting stimuli for the scientific community as starting point for the development of nanostructured materials, self-assembled biomolecular corona and fluorescence-based techniques for the design and investigation in the field of nanomedicine as theranostic applications.

APPENDIX PRYNICIPLES OF PHOTOPHYSICS

A.1 ELECTRONIC EXITED STATE, JABLOSNKY DIAGRAM

To introduce the applications which takes advantage of fluorescence processes is useful to shows the origin and the behavior of an electronic exited state. Electromagnetic radiation and matter can interact in different ways. Photochemistry is interested in the conversion of the energy ($h\nu$) of a photon absorbed by a chemical species in electronic energy, causing the transfer of an electron toward an orbital possessing higher energy. The species turns from its electronic ground state A to an electronic excited state A^* , which possesses a different electronic configuration:



This different electronic distribution causes the excited states of a chemical species to have physicochemical properties so different from those of the ground state that they can be considered different chemical species. For this reason, it is possible to define photochemistry as the chemistry of excited states. A photon can be absorbed and provoke the formation of an electronic excited state only if its energy $h\nu$ exactly corresponds to the energy difference between the excited and the ground state. Absorption electronic transitions occur in a time scale of the order of femtoseconds (10^{-15} s, Franck Condon Principle), creating excited states which are transient and can deactivate in different ways, shown in the Jablonski diagram (Figure 3). In this diagram electronic states (the singlets S_0 , S_1 and the triplets T_1 and T_2) are represented by thicker lines. The distinction between states with different spin multiplicity is due to the fact that transitions between these states are partially not allowed. Thinner lines represent the vibrational levels of the electronic states. After the energy absorption and reaching an excited vibrational level of an S_2 electronic excited state, the molecule goes rapidly ($< 10^{-12}$ s) to the ground vibrational level of that excited state (vibrational relaxation); then internal conversion

occurs, passing from the ground vibrational level of S2 to the isoenergetic vibrational level of S1, the electronic state at lower energy ($< 10^{-12}$ s). Another vibrational relaxation is then observed toward the ground vibrational state of S1, and at this stage the excited molecule can deactivate in two ways:

- 1- Non-radiative deactivation: the energy is released as vibrational energy generating heat. If this process occurs between two states with the same spin multiplicity we speak about internal conversion (10^{-12} - 10^{-6} s), while if the states have different spin multiplicity we have intersystem crossing (10^{-11} - 10^{-6} s). The successive vibrational relaxation leads in the first case to the ground vibrational level of S0, in the second case to that of T1;
- 2- Radiative deactivation: it is a process that generates luminescence and it is defined fluorescence if it occurs between states with the same spin multiplicity, phosphorescence if it occurs between states with different spin multiplicity. Similarly to S1, T1 can deactivate to S0 by radiative deactivation (phosphorescence, 10^{-4} - 10^2 s) or by nonradiative deactivation (intersystem crossing, 10^{-3} - 10 s, and successive vibrational relaxation to S0). Long-lived states such as T1 can undergo photochemical reactions, for example with oxygen, producing other chemical species. Generally speaking, since the time scale to decay to S1 and T1 are shorter than that necessary to pass from S1 and T1 to S0, only lowest energetic states of each spin multiplicity (that is S1 and T1) live enough to undergo luminescence (Kasha's rule) or photochemical reactions¹.

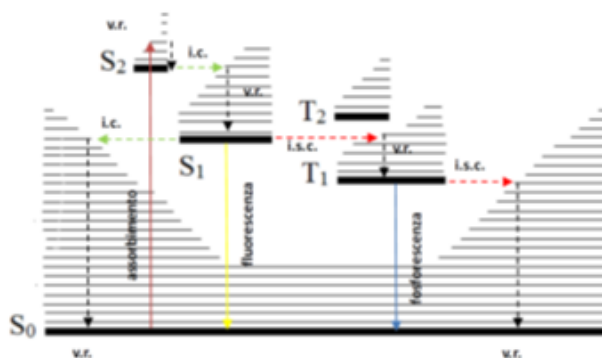


Figure 28. Jablonsky diagram for a generic molecule: *v.r.*=vibrational relaxation; *i.c.*= internal conversion; *i.s.c.*=intersystem crossing.

A.2 SOLVATOCHROMISM

Many relevant chemical and physical phenomena such as thermodynamics and reaction kinetics, as well as the position and intensity of the electronic absorption and emission bands, are often strongly dependent on the solvent. The basis of these effects on chemical equilibria and spectroscopic properties is the solvation of reagents and products. The solvation depends on the intermolecular forces between solute and surrounding solvent molecules, which include non-specific forces, such as electrostatic and polarization forces, and specific forces such as hydrogen bonds. The influence of solvents on the chemical equilibrium position was discovered in 1896 by Claisen and Wislicenus independently of each other. These results were examined by Stobbe, who in 1903 divided the solvents into two groups, based on their ability to isomerize some tautomeric compounds, with subsequent subdivision in solvent donors of hydrogen bonds (HBD, protic solvents) and non-hydrogen bond donors (non-HBD, aprotic solvents). Hantzschlater instead observed the displacement of the absorption and emission maxima at longer or shorter wavelengths of some molecules (fluorophores) as the polarity of the solvation environment varies.

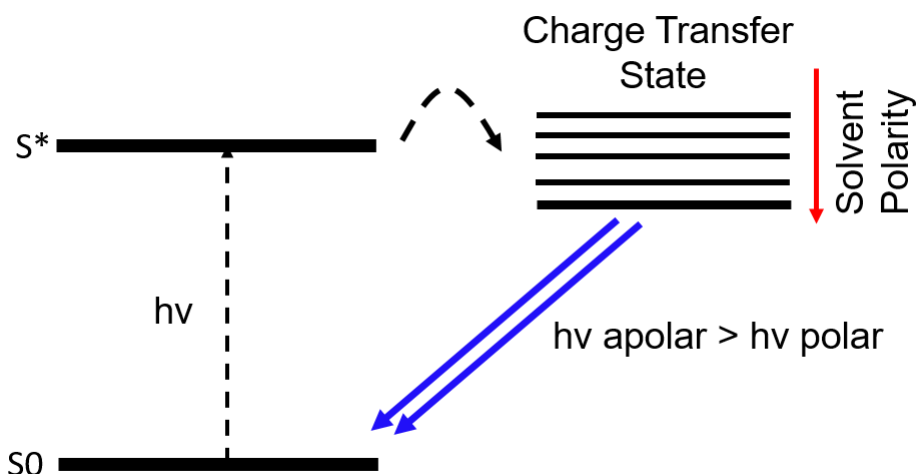


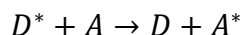
Figure 29. Schematization of Jablonsky diagram for a positive solvatochromic dye

This phenomenon has taken the name of solvatochromism. The solvatochromism manifests itself in molecules having a different dipole moment for the ground state and the excited state. Solvents can therefore stabilize the two electronic states in a different proportion, thus varying the energy gap between them and therefore the energy of the transition. In general, the transitions between two states, both in absorption and in emission, take place in a very short time, much lower than that of the motion of the nuclei, therefore considered to be stationary. Therefore, there is no reorganization of the solvent molecules causing the scheme of solvation of the excited state and that of the ground state to remain unchanged (Frank-Condon principle). However, if the residence time in an excited state is large enough, a reorientation of the solvent molecules can occur, with associated internal conversion, which brings the molecule into a lower energy vibro-electronic state and, from this new energy level, it can take place a radiative relaxation with fluorescence emission that brings the molecule to the ground state². In this case, the energy emitted by the solvatochromic dye molecule will be as

low as the stabilization effect of the excited state operated by the solvent is greatest. There are two types of solvatochromism, negative and positive. If, as the solvent polarity increases, the fundamental state of the molecule is more stabilized than its first excited state, we observe hypsochromic shift (towards high energies in the spectrum) and the solvatochromism is called negative. Vice versa, if as the solvent polarity increases the excited state is stabilized more than the fundamental one, the solvatochromism is called positive and we observe a bathochromic shift (towards low energies). The solvatochromic probes are widely used for the study of polarity in complex systems or in the diagnostic field as bioluminescent sensors in imaging techniques ^{3,4}.

A.3 Electronic Excitation Energy Transfer

With the term electronic excitation energy transfer we indicate the process in which an excited molecule of a donor D^* decays to its ground state D with the simultaneous transfer of its excitation energy to a molecule of acceptor A , which is thus led to an excited state A^* :



it is possible to observe this phenomenon exciting D in a spectral region in which it absorbs but A does not: if energy transfer occurs, D^* emission is quenched and at the same time the appearance of the emission of A^* is observed, which is called sensitized emission. In the case in which D and A are different molecules of the same chemical species we speak about homo energy transfer. It is possible to observe also intramolecular energy transfer in the case of a (super)molecule containing a donor and an acceptor, separated by a spacer L :



Two possible mechanisms of energy transfer exist, radiative one and non-radiative one. The radiative mechanism (also called trivial energy transfer) does not require the direct interaction of D and A , but it occurs via the electromagnetic field produced from the photons emitted by D , which can be absorbed by A , provided that an overlap

between the emission spectrum of D and the absorption one of A exists. This mechanism consists of two different steps:



It is possible to correlate the probability of absorption of A of a photon emitted by D*, that is the probability of energy transfer ($a_{D^* \rightarrow A}$), with the overlap between the emission spectrum of D and the absorption one of A. In particular a relation stands between $a_{D^* \rightarrow A}$ and the overlap integral J , defined as

$$J = \int_0^{\infty} F_D(\lambda) \varepsilon_A(\lambda) \lambda^4 d\lambda$$

where F_D is the normalized emission spectrum of D (the area under the spectrum is equal to 1) and $\varepsilon_A(\lambda)$ is the absorption spectrum of A in $\text{dm}^3 \cdot \text{mol}^{-1} \cdot \text{cm}^{-1}$. So as J increases, the probability of radiative energy transfer linearly increases. This probability is also directly proportional to the concentration of A, to the optical path length and inversely proportional to the luminescence quantum yield of D. The radiative energy transfer can occur over extremely long distances: solar irradiation on Earth is a striking example. It is necessary that the transition of absorption in the acceptor is spin-allowed so that the radiative energy transfer can occur: thus singlet(D*)-singlet(A*) and triplet(D*)-singlet(A*) transfers are allowed, while singlet(D*)-triplet(A*) and triplet(D*)-triplet(A*) transfers are not allowed.

The *non-radiative mechanism*, on the other hand, requires an intermolecular interaction between D and A mediated by the electromagnetic field. The energy transfer between the partners occurs in resonance conditions, involving isoenergetic non-radiative transitions between D* and A. Also, in this case the probability of energy transfer is directly proportional to J . The theoretical description of the process leads to obtain that the interaction between D* and A consists of a Coulombic term (Förster mechanism) and of an exchange term (Dexter mechanism) (Figure 3).

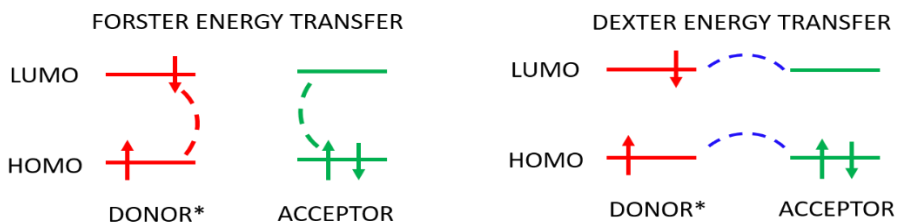


Figure 30. energy transfer via Coulombic mechanism (left) and with exchange mechanism (right)

The Coulombic mechanism arises from the coupling of the electronic transition moments of electric dipole of the transitions $D^* \rightarrow D$ and $A \rightarrow A^*$. This interaction is governed by Förster's equation, which correlates the energy transfer kinetic constant with the distance R_{DA} :

$$k_{ET} = \frac{1}{\tau_D} \left(\frac{R_0}{R_{DA}} \right)^6$$

Where τ_D is the lifetime of the donor in the absence of the acceptor and R_0 is the Förster distance, that is the distance between D and A at which the energy transfer rate (k_{ET}) is equal to the decay rate of the donor in the absence of the acceptor ($k_{ET} = \frac{1}{\tau_D}$). At this distance half of the molecules of D decay via energy transfer. Förster distance is correlated to the overlap between the emission spectrum of D and the absorption spectrum of A by means of the following relation:

$$R_0^6 = 2.303 \frac{9000 \chi^2 \Phi_D}{n^4 N_A 128 \pi^5} J$$

Where χ is the orientational factor which describes the relative orientation of the electric dipole moment of D and A (it is assumed to be equal to 2/3 in the case of freely rotating D and A), Φ_D is the fluorescence quantum yield of D in the absence of A, n is the refractive index of the solvent, N_A is the Avogadro's constant, is the luminescence spectrum of D normalized to 1m and J is the spectral overlap. The higher the overlap between the emission spectrum of A and the absorption spectrum of A, the higher the value of R_0 .

Typical values are about 20-100 Å. It is possible to define an efficiency of energy transfer

$$\eta = \frac{k_{ET}}{k_{ET} + k_D}$$

which is linked to R_{DA}^6 by means of the following relation

$$\eta = \frac{R_0^6}{R_0^6 + R_{DA}^6}$$

which highlights that the efficiency of the energy transfer process is equal to 0.5 when $R_{DA} = R_0$. It is possible to experimentally obtain η from the fluorescence quantum yield of D in the presence of A (Φ_{DA}) and in its absence (Φ_D), or from lifetimes in the two conditions (τ_{DA} , τ_D):

$$\eta = 1 - \frac{\Phi_{DA}}{\Phi_D}$$

$$\eta = 1 - \frac{\tau_{DA}}{\tau_D}$$

The processes of Förster type energy transfer are generally allowed if the transition in D and in A does not involve spin changes of the single species. On the contrary Dexter type energy transfer dominates. The exchange interaction requires a simultaneous double electronic exchange involving the LUMO of D and the HOMO of A (Figure 3) and it is a short-range interaction, becoming important when R_{DA} is ≤ 5 Å. According to Dexter model, the kinetic constant for the exchange mechanism decays exponentially with R_{DA} :

$$k_{ET}^{ex} = \frac{2\pi}{\hbar} K J^{ex} e^{-\frac{2R_{DA}}{L}}$$

where K is a factor related to the specific orbitalic interaction, J^{ex} is the normalized overlap integral and L is an average Van der Waals radius which simulates molecular dimensions⁵.

A4 Electronic absorption spectra

For the acquisition of electronic absorption spectra, a double beam spectrophotometer UV/Vis Perkin Elmer Lambda-45 was used. The

amount of light absorbed is provided by the ratio of the intensity of incident light (I_0) and the intensity of transmitted light (I_t) and is expressed by Absorbance (A):

$$A = \log_{10} \frac{I_0}{I_t}$$

A is related to the chromophore concentration by the Lambert Beer equation as following:

$$A = c\epsilon l$$

Where c is the chromophore concentration express in mol/L, ϵ is the molar extinction coefficient (mol/L)⁻¹cm⁻¹ and l is the optical path of the sample (1 cm optical path of the cuvette).

A5 Emission and excitation spectra

The registration of the emission and excitation spectra was performed using a spectrofluorimeter Perkin Elmer LS55 and a spectrofluorimeter Edinburgh FLS920.

A very used quantity in photophysics is the luminescence quantum yield (Φ_{PL} , QY), defined as the ration between the number of emitted photons and the number of photons absorbed by a species in the same time and for a determined excitation wavelength:

$$\Phi_{PL} = \frac{\text{number of emitted photons}}{\text{number of absorbed photons}}$$

For the assessment of luminescence quantum yield with a relative method we need a reference which its quantum yield is known. The species used as a reference has to emit in the same spectral region in which the sample emits so that emission spectra are obtained in the same experimental conditions. For the assessment of Φ_{PL} we adopted the following experimental procedure: the absorption spectra of the sample and of the reference were registered and, when possible, isoabsorption points were used as excitation wavelength for the registration of emission spectra. The following equation was used to determine the value of luminescence quantum yield:

$$\Phi_{PL} = \Phi_{ref} \frac{I_x}{I_{ref}} * \frac{A_{ref}}{A_x} * \left(\frac{\eta_x}{\eta_{ref}} \right)^2$$

Where Φ_{ref} is the referment fluorescence QY. I_{ref} , A_{ref} and η_{ref} are the referment emission intensity, the absorption at excitation wavelength and the dielectric constant of the solvent respectively. I_x , A_x and η_x are the analogous parameters for the sample.

A6 Excited state lifetime measurements

Excited state lifetime measurements were performed using a spectrofluorimeter Edinburgh Analytical Instruments FLS920, equipped with a time-correlated single-photon counting device, which is able to measure lifetimes in a range between 0.5 ns and 30 μ s. The time-correlated single-photon counting is based on the probability that a single photon emitted by a luminescent sample is collected by a proper high sensitivity detector: this probability is statistically correlated with the variation of the concentration of the excited states in solution.

A.7 Dynamic Light Scattering

Dynamic Light Scattering (DLS) measurements were performed using a Malvern Instruments DLS ZetaSizer Nano-ZS (Figure 2.7). With this instrument it is possible to determine the dimension of particles having a diameter between 1 nm and 10 μ m. The DLS technique allows the measurements of submicrometric particles. It exploits the study of Brownian motions to determine the hydrodynamic diameter of particles suspended in solution. The hydrodynamic diameter is obtained by the correlation of the scattering intensity fluctuations recorded over time experimentally irradiating the sample with a 633 nm laser. The laser produce scatter events when particles diffuse through the laser beam, so recording and correlating over time the fluctuations is possible to get the particle size distribution. The particle size distribution is obtained from the relative scattering intensity graph of the several particle size

classes (intensity size distribution). It is also possible to obtain this distribution as a function of particle volume, or particle number. Let us consider, for example, a sample containing two populations of spherical particles having a diameter of 5 and 50 nm respectively and present in the same number (Figure 4). As far as the number of particle is concerned, the graph consists of two peaks, one at 5 nm and the other at 50 nm, with a 1:1 ratio. If we convert the number distribution in volume distribution, the two peaks ratio is 1:1000, because the volume of a sphere is equal to $\frac{4\pi}{3} \left(\frac{d}{2}\right)^3$. If we switch to intensity distribution, the ratio becomes equal to 1:106 according to Rayleigh approximation.

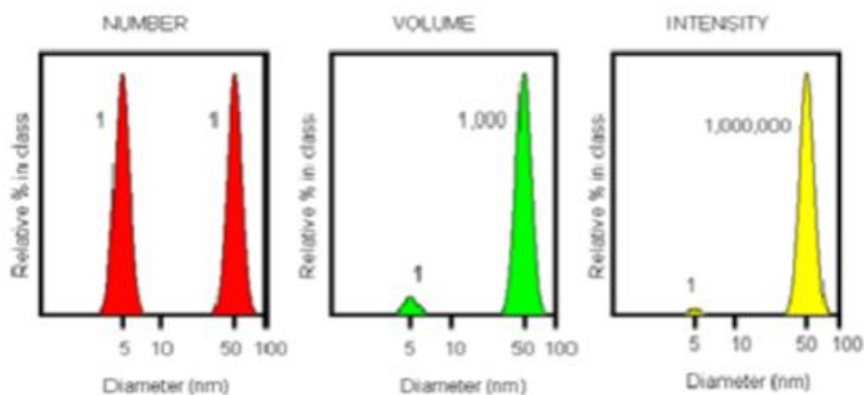


Figure 31. number, volume and intensity distribution of a sample containing spherical particles of 5 and 50 nm diameter in equal numbers.

A.8 Fluorescence Correlation Spectroscopy

Fluorescence Correlation Spectroscopy is a technique where the fluorescence intensity fluctuations are correlated over time in order to describe the dynamic of the system. FCS can provide information as diffusion coefficient of the fluorophore and concentration with very high sensitivity because it observes a small number of molecules (nanomolar to picomolar concentrations) in a small volume ($\sim 1\mu\text{m}^3$)⁶. Commonly, FCS is employed in the context of optical microscopy, in particular Confocal microscopy or two-photon

excitation microscopy. In these techniques light is focused on a sample and the measured fluorescence intensity fluctuations (due to diffusion, physical or chemical reactions, aggregation, etc.) are analyzed using the temporal autocorrelation. The classical FCS setup (Figure 5) consists of a laser line (wavelengths ranging typically from 405–633 nm (cw), and from 690–1100 nm (pulsed)), which is reflected into a microscope objective by a dichroic mirror. The laser beam is focused in the sample, which contains fluorescent particles (molecules) in such high dilution, that only a few are within the focal spot (usually 1–100 molecules in one fL). When the particles cross the focal volume, they fluoresce. This light is collected by the same objective and, because it is red-shifted with respect to the excitation light it passes the dichroic mirror reaching a detector, typically a photomultiplier tube. The FCS curve by itself only represents a time-spectrum. Conclusions on physical phenomena have to be extracted from there with appropriate models. The parameters of interest are found after fitting the autocorrelation curve to modeled functional forms⁷. The correlation function is obtained by the time trace fluctuations by the following equation:

$$G(\tau) = \frac{\langle \delta I(\tau) \delta I(t + \tau) \rangle}{\langle I(t) \rangle^2}$$

The time-dependent fluorescence intensity ($I(t)$) is then analyzed in terms of its temporal autocorrelation function ($G(\tau)$), which compares the fluorescence intensity at time t with the intensity at ($t + \tau$), where τ is a variable interval, averaged over all data points in the time series.

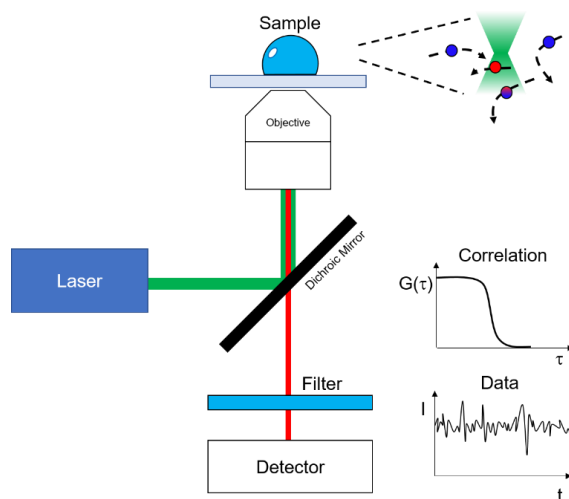


Figure 32. FCS setup and analysis representation

REFERENCES

- 1 M. T. G. Marco Montalti, Alberto Credi, Luca Prodi, *Handbook of Photochemistry, Third Edition*, Taylor & Francis, Third edit., 2006.
- 2 E. Buncel and S. Rajagopal, *Acc. Chem. Res.*, 1990, **23**, 226–231.
- 3 L. Malacrida, D. M. Jameson and E. Gratton, *Sci. Rep.*, 2017, **7**, 1–11.
- 4 O. Golfetto, E. Hinde and E. Gratton, *Biophys. J.*, 2013, **104**, 1238–1247.
- 5 J. R. Lakowicz, *Principles of Fluorescence Spectroscopy*, Springer US, 3rd editio., 2006.
- 6 H. Chen, E. R. Farkas and W. W. Webb, *Chapter 1 In Vivo Applications of Fluorescence Correlation Spectroscopy*, Elsevier Inc., 2008, vol. 89.
- 7 M. Á. Medina and P. Schwille, *BioEssays*, 2002, **24**, 758–764.

